Universidade de Aveiro Departamento de Electrónica, Telecomunicações e Informática,
2017

Carolina Teixeira de Sousa Gouveia

Bio-Radar

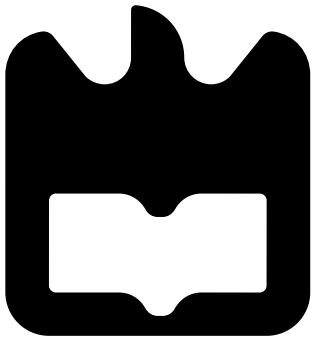

Aos meus pais, irmãos e sobrinho

Carolina Teixeira de Sousa Gouveia

Bio-Radar

Dissertação apresentada à Universidade de Aveiro para cumprimento dos requisitos necessários à obtenção do grau de Mestre em Engenharia Eletrónica e Telecomunicações, realizada sob a orientação científica do Professor Doutor José Manuel Neto Vieira, Professor do Departamento de Eletrónica, Telecomunicações e Informática da Universidade de Aveiro, sob co-orientação científica do Professor Doutor Pedro Renato Tavares Pinho, Professor Adjunto do Instituto Superior de Engenharia de Lisboa e com a colaboração do Doutor Daniel Filipe Simões Malafaia Investigador Doutorado do Instituto de Telecomunicações, pólo de Aveiro

o júri

presidente

Professor Doutor Nuno Miguel Gonçalves Borges de Carvalho
Professor Catedrático do Departamento de Electrónica, Telecomunicações e Informática da Universidade de Aveiro

vogais

Professor Doutor Sérgio Reis Cunha
Professor Auxiliar do Departamento de Engenharia Eletrotécnica e de Computadores da Faculdade de Engenharia do Porto

Professor Doutor José Manuel Neto Vieira
Professor Auxiliar do Departamento de Eletrónica, Telecomunicações e Informática da Universidade de Aveiro (orientador)

agradecimentos

Antes demais queria agradecer aos meus pais pela oportunidade que me deram para tirar este curso e por todo o apoio dado incondicionalmente, não só ao longo deste percurso académico, mas também ao longo da vida. Aos meus irmãos e cunhado, um grande obrigado pelo apoio e conselhos.

Agradeço ao meu orientador, Professor Doutor José Manuel Neto Vieira, e co-orientador Professor Doutor Pedro Renato Tavares Pinho pela excelente orientação e preciosa ajuda. O acompanhamento contínuo foi imprescindível para a conclusão com sucesso desta dissertação. Obrigada por tudo o que me ensinaram.

Nos meus agradecimentos, destaco também o apoio fulcral do meu colaborador Doutor Daniel Malafaia, que foi incansável comigo, com a maior paciência do mundo para me ajudar a ultrapassar todas as barreiras que apareceram no decorrer deste projeto. Sem ti nunca teria chegado tão longe. Obrigada também à Marina Jordão pela excelente formação em LabVIEW e aos restantes investigadores do instituto que ajudaram e apoiaram de diferentes formas.

Por fim, agradeço a todos os meus amigos, que com o seu companheirismo e amizade conseguiram fazer todos os meus dias mais felizes. Em especial, devo destacar a Vanessa Martins não só por ter sido uma colega de trabalho impecável e cúmplice com a minha dedicação, mas agradeço-lhe em especial pela a companhia, lealdade e pura amizade que cresceu exponencialmente ao longo destes anos.

A todos, obrigada!

Palavras Chave Bio-Sinais, Radar, CW Radar, SDR, Efeito Doppler

Resumo

Nesta dissertação é desenvolvido um protótipo de um bio-radar, cujo foco é a aquisição e processamento do sinal respiratório em tempo real. O sistema do bio-radar permite medir sinais vitais com precisão, baseando-se no princípio do efeito Doppler, que relaciona as propriedades do sinal recebido com a variação da distância percorrida desses sinais. Essa distância está compreendida entre as antenas do radar e a caixa torácica do paciente. No contexto deste projeto, é apresentado o modelo matemático do bio-radar e é também desenvolvido um algoritmo que visa extrair o sinal respiratório tendo em consideração a sensibilidade dos sinais envolvidos tal como o modo de operação do sistema. O protótipo em tempo real desenvolvido nesta dissertação usa um *front-end* baseado em *Software Defined Radio* (SDR) e os sinais por ele adquiridos são processados no *software* LabVIEW da National Instruments.

Keywords Bio-Signals, Radar, CW Radar, SDR, Doppler Effect

Abstract In this dissertation, a prototype of a bio-radar was developed with focus in the real-time acquisition and processing of the respiratory signal. The bio-radar system can measure vital signals accurately by using the Doppler effect principle that relates the received signal properties with the distance change between the radar antennas and the person's chest-wall. In this framework, a mathematical model of the bio-radar is presented. Also, an algorithm for respiratory rate extraction is proposed having in mind the acquired signal's sensitivity and the system's operation. The real-time acquisition system is developed using a front-end based in SDR and the acquired signals are processed using the LabVIEW software from National Instruments.

Contents

List of Figures

List of Tables

Acronyms

ADC	Analog-to-Digital Converter
API	Application Programming Interface
AT	ArctangenT demodulation
BPM	Beats per minute
Breaths/min	Breaths per minute
BSS	Blind Source Separation
CW	Continuous-Wave
CWS	Chest-Wall Simulator
DAC	Digital-to-Ananlog Converter
DSP	Digital Signal Processing
ECG	Electrocardiogram
FBW	Fractional Bandwidth
FCC	Federal Communications Commission
FFT	Fast Fourier Transform
FIR	Finite Impulse Response
FMCW	Frequency-Modulated Continuous Wave
IBP	Initial Breathing Pattern
ICA	Independent Component Analysis
IF	Intermediate Frequency
IIR	Infinite Impulse Response
IQ	In-phase and Quadrature
LabVIEW	Laboratory Virtual Instrumentation Engineering Workbench
LM	Levenberg-Marquardt

LNA	Low-Noise Amplifier
LO	Local Oscillator
LSF	Least Square Fitting
MATLAB	MATrix LABoratory
MUSIC	MUltiple SIgnal Classification
OSA	Obstructive Sleep Apnea Syndrome
PA	Power Amplifier
PLL	Phase Locked Loop
PMI	Point of Maximal Impulse
PSD	Power Spectral Density
RCS	Radar Cross Section
RF	Radio Frequency
Rx	Reception
SDR	Software Defined Radio
SIDS	Sudden Infant Death Syndrome
SNR	Signal-to-Noise Ratio
TVD	Total Variation Denoising
Tx	Transmission
UHD	USRP Hardware Driver
USRP	Universal Software Radio Peripheral
UWB	Ultra-Wideband
VCO	Voltage-Controlled Oscillator
VI	Virtual Instruments
Wave/sec	Waves per second
WT	Wavelet Transform

Chapter 1

Introduction

1.1 Motivation

The cardiopulmonary signal monitoring, without the usage of contact electrodes or any type of invasive sensors, has several applications in the medical field, home health care, nursing of elderly or commercially oriented applications. This sensorless measurement of bio-signals has the potential to improve many areas.

In the medical field, among many other applications, it can be highlighted the continuous monitoring of vital signals in bedridden patients, as in a burn unit where physical contact with the patient is discouraged. Also for sleeping monitoring, namely to support cases of Obstructive Sleep Apnea Syndrome (OSA) without interfering in the normal life style of the patients, or in the prevention of Sudden Infant Death Syndrome (SIDS), [1]. In terms of commercial applications, it can be highlight driver monitor, where his vital signals are monitored to avoid any possible accident in case of cardiac failure. Applications in psychology are also possible, as for example measurement of stress response, [2].

The bio-radar system can measure vital signals accurately by using the Doppler effect principle, that relates the received signal properties with the distance change between the radar antennas and the person's chest-wall.

The concept of non-contact signal extraction of human physiological parameters, has been demonstrated by pioneers during the 1970's, where both the respiration and heartbeat were measured separately during apnea interspersed periods, [3]. Later, between 1980's and 1990's this system was implemented using incorporated analog and digital signal processing. Nowadays the research in this area is even more focused on the development of systems with features that guarantee low power, small dimensions, better accuracy, long range detection and more robust operation [1]. The research in this technology advancement has led to different front-end architectures and signal processing methods that are suitable for different environments. However, there are some challenges in this field that still need to be overcome, such as the removal of non-related patient motion that generates artifacts in the extracted signal and the proper separation in real-time of the heartbeat signal from respiratory signal.

With the usage of a front-end based on Software Defined Radio (SDR), the prototype developed in this dissertation offers a low power and portable solution for bio-radar implementation.

1.2 Objectives

In this dissertation, a bio-radar prototype is proposed with focus on the real-time acquisition and processing of the respiratory signal. Therefore, this prototype should be capable to display the respiratory signal of the monitored subject and should also be able to compute the respiratory rate in real-time.

In this framework, a mathematical model of the bio-radar is presented. Also, an algorithm for respiratory rate extraction is proposed having in mind the acquired signal's sensitivity and system's operation. Moreover, conducted experiments were performed using a Chest-Wall Simulator (CWS), developed to simulate the human chest-wall motion with a stable frequency, in order to validate the presented mathematical model and the Digital Signal Processing (DSP) algorithm. Finally, the overall system's performance is evaluated using as reference a certified measuring equipment, the Biopac MP100.

Regarding the state of the art of the bio-radars, this prototype stands out with the usage of SDR instead of other complex hardware components. Thus, the SDR usage revealed a straightforward solution to implement a bio-radar, as it makes possible to process digitally the acquired signals in any software development platform supported by USRP Hardware Driver (UHD).

1.3 Content Organization

In this section the structure of this dissertation is outlined and a brief description of each chapter is presented.

This document is divided in the following 6 chapters:

- **Chapter 1** - is the current chapter. Its aim is to frame the studied system in the society's need, by revealing the objectives that are intended to be achieved and its possible application in the everyday life.
- **Chapter 2** - in this chapter an overview of the theory of radar operation is explained, with focus in the Doppler radar where different radar systems are presented. Also, an introduction of the Software Defined Radio architecture is made. Furthermore, the cardiopulmonary physiology and its physiological motion and measurement using radars are studied. Finally, a general overview of the radar hardware is made, including the front-end architectures and the antennas design.
- **Chapter 3** - the architecture of the bio-radar implemented in this dissertation is defined in this chapter, beginning with its mathematical model definition, simulation and later the sources of disturbance exploitation in a real scenarios. Regarding the exposed constrains, several techniques to overcome them are evaluated and the most suitable are selected. In the end of this chapter a DSP algorithm for signal extraction is proposed and simulated.
- **Chapter 4** - in this chapter, the implementation of the proposed prototype of a bio-radar is described with a special focus in the software development in LabVIEW.
- **Chapter 5** - this chapter shows and discusses the results obtained with the developed prototype. Moreover, a comparison with a vital signals measuring equipment is made in order to evaluate the bio-radar's performance.

- **Chapter 6** - in this last chapter conclusions over the developed work are presented and future improvements and different approaches are pointed out.

1.4 Contributions from the Developed Work

Some of the results obtained in this work, were published in two scientific papers in the following conferences:

1. C. Gouveia, D. Malafaia, J. Vieira, P. Pinho, A. Tomé, P. Magalhães, "Bio-Radar Model Validation using Chest-Wall Simulator", 23^{rd} Conference of Pattern Recognition, Portuguese Military Academy, Lisbon, Portugal 2017.

2. C. Gouveia, D. Malafaia, J. Vieira, P. Pinho, "Bio-Radar Performance Evaluation for Different Antenna Design", 11^{th} Congress of the Portuguese Committee of URSI "New technologies for mobility", Lisbon, Portugal 2017

Chapter 2

Bio-Radar Background Overview

This chapter aims to frame the system developed in this dissertation in the radar area. Thus, it begins with a radar theory overview, with emphasis in the Doppler radar effect and the different radar types that apply this principle. Since the goal of the bio-radar is to measure small physiological motion driven by the cardiopulmonary activity, an anatomic overview is made with focus on the cardiopulmonary system and their interaction in the skin surface. Finally an overall vision about the radar technology used is done, where the possible hardware configurations are presented and a state of the art of the already implemented bio-radars is analysed.

2.1 Radar Fundamentals

The Radar term is an acronym which stands for Radio Detection And Ranging. The simplest form of a radar system consists in a transmitter, a receiver, an antenna and hardware or software dedicated to signal processing, as presented in Figure 2.1. The transmitter

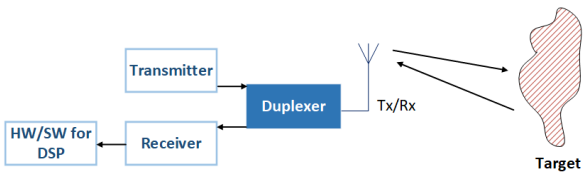

Figure 2.1: Basic model of a radar system, [3].

generates a signal that is modulated and sent towards one or more targets in the form of electromagnetic waveform. The receiver demodulates the signal from reflected echoes, to an intermediate frequency or even to the baseband, depending on the transceiver architecture, as we will see further in section 2.3. Other task of the receiver is to reduce the noise and interference that are present in the signal and its amplification for further digitization, [3]. These echoes provide information about the the target's presence, position, size/shape and motion [4], and it can be obtained after signal processing.

Different information requires different parameters of the received signal and hence different hardware configurations of the used transceivers. For instance, the distance of the target relative to the radar can be obtained regarding the time delay between the transmitted and the received signal. In this way, is possible to compute the range, once the speed of

electromagnetic waves in free space is the same as the speed of light, [4]. Moreover, the frequency shift of the received signal enables the computation of the target's velocity motion. Also the physical dimensions of the target, such as the size, geometry or composition, can be obtained from the Radar Cross Section (RCS) that is achieved by the signal's received power, [3].

The radar has been used where other sensor technologies do not have conditions to operate properly, for example during night time, in fog or for long range applications, [5]. Thus, the main applications of the radar technology encompasses the ship and airplane detection, the traffic control and tracking objects located in hidden places, once the Radio Frequency (RF) signals used can penetrate through obstacles, [3].

Each application requires different operation characteristics, for example over the horizon radars (or/and space radars) demands large size antennas with transmitted power in the order of megawatts. On the other hand, radars for medical applications need small size antennas and work with a power level around milliwatts, [5].

The handled power in these systems can be given by the radar equation, which estimates the received power by taking into account the target characteristics and its range from the transceiver, [4]. The radar focus the incident power in a desired direction, where a specified portion of power will be intercepted by the target that re-radiates it in several directions. The incident power is described by the antenna gain G, which is defined as the radiated power in the target's direction when compared with the power that should be radiated by a lossless isotropic antenna, if the same incident power is in its input. The amount of incident power that is radiated backwards in direction to the radar is measured by the RCS σ_{RCS} of the target and is expressed in area units. In other words, the RCS is the measure of the target's size as seen by the radar, [6]. Regarding the involved parameters mentioned previously, the radar equation is equal to (2.1)

$$P_r = \frac{P_t G^2 A_{eff} \sigma_{RCS}}{(4\pi)^2 R^4} \tag{2.1}$$

where P_t is the transmitted power, G is the antenna gain, A_{eff} is the effective area of the radar's antenna, σ_{RCS} is the radar cross-section and R is the range between the radar and the target. The area A_{eff} determines the portion of power reflected by the target that is received by the radar and can be expressed according to equation (2.2):

$$A_{eff} = \frac{G\lambda^2}{4\pi} \tag{2.2}$$

where λ is the wavelength.

By replacing (2.2) in the radar equation (2.1), the total power received by the radar can be expressed as equation (2.3):

$$P_r = \frac{P_t G^2 \lambda^2 \sigma_{RCS}}{(4\pi)^3 R^4} \tag{2.3}$$

The radar maximum range R_{max} is defined by the distance beyond the extremely necessary to detect the target. It means that at this distance the received power P_r is equal to the minimum power that can be detected S_{min}, [6]. The maximum range is expressed by equation (2.4):

$$R_{max} = \Big[\frac{P_t G A_{eff} \sigma_{RCS}}{(4\pi)^2 S_{min}}\Big]^{(1/4)} \tag{2.4}$$

In real scenarios other facts have to be considered: the detection of a single target is only possible when the received signal is properly separated from noise sources, such as the phase noise (which is going to be seen in detail in chapter 3) and thermal noise $N_0 f_B$, that is uniformly distributed over the frequency spectrum, [5]. Regarding the equation (2.1), it is possible to compute the Signal-to-Noise Ratio (SNR) in terms of the thermal noise, as described in equation (2.5):

$$SNR = \frac{P_t G^2 \lambda^2 \sigma_{RCS}}{(4\pi)^3 R^4 N_0 f_B} \tag{2.5}$$

where N_0 is the noise spectral power density in Watts and f_B is the bandwidth of the receiver.

Other consideration about the real scenario is the presence of multiple objects in the target's surrounding environment, that cause parasitic reflections in the received signal. The resultant effect is introduced and studied in chapter 3.

2.1.1 Doppler Radar

Doppler radars are based on the Doppler effect, also known as Doppler shift. Their main application is to detect moving targets and compute their velocity, being the traffic control the most common application.

The Doppler effect is the change in frequency of the received signal caused by the motion of the target relative to the radar. This frequency change depends on the total number of wavelengths in the two-way path, between the radar and the target, given by $2R/\lambda$ in waves per second (Wave/sec), where R is the range and λ is the wavelength of the transmitted signal and both are measured with the same unit (meters).

By considering that the radar is at a stationary position, the same frequency is received over the time if the target is also stationary, because the same number of Wave/sec is received. However, if the target moves toward or away from the radar different frequencies are received: if the motion is toward to the radar, higher frequency is received due to the bigger number of received Wave/sec. On the other hand, if the target is moving backwards, a lower frequency is perceived, due to the fewer number of received Wave/sec, [4].

The frequency shift effect can also be perceived as phase change, once each wavelength corresponds to a phase change equal to 2π in radians. Thus, if the travelled path of the wave changes due to the target's motion, also the number of Wave/sec changes, hence the total phase change relative to range R is given by the equation (2.6).

$$\phi = 2\pi \frac{2R}{\lambda} \tag{2.6}$$

The velocity of the target's motion can also be calculated by differentiating (2.6) in relation to time. The differentiation results in the angular velocity ω_d represented by the equation (2.7), [4]

$$\omega_d = \frac{4\pi \upsilon_r}{\lambda} \tag{2.7}$$

where $\upsilon_r = dR/dt$ is the radial velocity (m/s) and it can be computed through equation (2.8):

$$\upsilon_r = \frac{c f_d}{2 f_t} \tag{2.8}$$

where $c = 3 \times 10^8$ m/s is the speed of light, f_d is the Doppler frequency shift and f_t is the radar frequency, [4].

The Doppler effect is the basis of some radar architectures, namely the Continuous Wave (CW) radar, as we will see further in the next sections.

Continuous Wave Radar

CW radar transmits and receives a RF signal with narrow bandwidth continuously. A radar system that uses this operation mode is composed by a signal generator, which is used to generate the signal for transmission and to down-convert the received signal in the radar's receptor. The receptor is usually heterodyne or homodyne. The radar can have a single antenna for either Transmission (Tx) and Reception (Rx), where a circulator or a duplexer are used to separate signals in the transceiver. Also two separated antennas can be used for Tx and Rx operation, [4]. Once the system usually handles with narrowband signals, it is possible to perceive the frequency shift due to the Doppler effect when the target is moving, thus CW radar can measure the velocity of the target's motion and this feature allows to distinguish between a moving target and stationary objects, independently of its distance (within the radar's range) or its velocity, [6].

CW radar presents an important advantage regarding the implementation complexity, once it is significantly simple to implement. It uses a single oscillator for both Tx and Rx and once the transmitted signals and their reflections respectively have narrow bandwidth, the filters used in the receiver chain can be quite simple.

Nonetheless, some disadvantages can be pointed out about this type of Doppler radars. Once Tx and Rx are continuous operations, due to circuitry or antennas coupling, a portion of the transmitted signal can affect the signal in the receptor causing leakage, [4]. In addiction to leakage, also clutter from multiple reflections of stationary objects in the range can contribute to the signal power at the carrier frequency, generating low frequency noise and DC offsets, which will be discussed later in chapter 3.

Frequency-Modulated Continuous Wave Radar

Frequency-Modulated Continuous Wave (FMCW) allow the computation of the target's velocity and distance between the target and the radar, once it improve the range resolution that do not exist for a single frequency waveform (like in CW radar case), [5]. These type of radars perform a frequency modulation, usually with a triangular modulation in order to increase and decrease the frequency linearly over the time. A visual example of this modulation type is represented in Figure 2.2, [4], where the triangle waveform represents the transmitted signal with its frequency modulation over time. The dashed triangular signal is the received signal, which is delayed in relation to the transmitted $T = 2R/c$ seconds. Regarding Figure 2.2, the modulated signal has bandwidth equal to Δ_f and it determines the accuracy of the range measurement. The modulation is done with a rate equal to f_m and it determines the maximum detectable range without ambiguity. The mix between the transmitted and the received signals result in a frequency difference f_r, that changes according to the target motion.

Pulsed Radar

Pulse radar transmits pulsed bursts and then listens the resultant echoes. Tx and Rx operations are not done simultaneously. Therefore the pulse repetition period should be

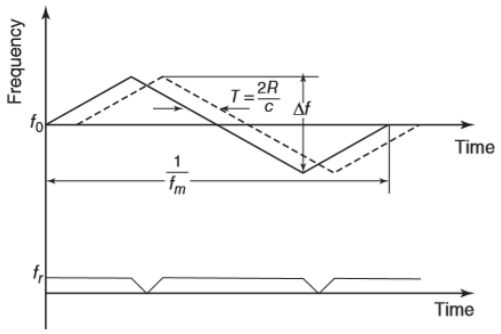

Figure 2.2: Linear frequency modulation performed by a FMCW radar, [4].

longer than the round-trip path length of the transmitted wave and thus the radar receives the echoes between transmissions, [3].

Since the reflections are not acquired at the same time of the signal's transmission, the leakage from the transmitter and the parasitic reflections are separated temporally from the long-range targets. This means that as we have to wait for the full transmission, the reflections that occur immediately from short-range objects are not detected, which represents a clear advantage when comparing to the CW radar. Other advantage brought by the pulse radar, as well as the FMCW, is the possibility to measure the target range.

In the framework of our application, the target is the subject that we want to monitor, which is at a short-range as his stationary body parts, giving limitations to the first advantage previously mentioned. In addiction, the range measurement is not important for the vital signals measurement, hence is not a necessary feature that should be considered.

Comparing with the CW radar, the pulsed radar present a disadvantage regarding the implementation complexity, [3]. Other disadvantage of this type of radars is the lack of velocity resolution, thus a limit in target's velocity and range position should be denoted in order to guarantee the proper target's detection.

Ultra-Wideband Radar

An Ultra-Wideband (UWB) is a special application of the pulsed radar and is characterized by its large bandwidth regarding the centre frequency (there is no carrier) and is generated by a very short duration pulses rather than continuous waves. The Federal Communications Commission (FCC) has established that a signal can be categorized as a UWB signal if its Fractional Bandwidth (FBW), which is the measure of how wide is the bandwidth, is 20% of the centre frequency or has a bandwidth equal or greater than 500 MHz, regardless of the FBW, [7], [4].

Signals generated by pulses with short duty-cycle have low Power Spectral Density (PSD) and thus the signal's energy is equally spread over its bandwidth, more specifically from values around DC to several gigahertz. Figure 2.3 shows the comparison between the PSD from a UWB transmission system and from a narrowband system.

The operation of UWB radars starts by the short pulses transmission through the antenna. The target will reflect a portion of the transmitted signal. The total range ΔR of this radar is given by the equation (2.9), [8]:

$$\Delta R = \frac{c}{2 * BW} = \frac{\tau c}{2} \tag{2.9}$$

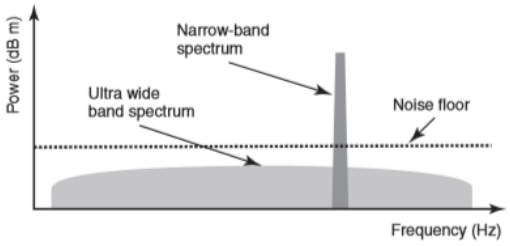

Figure 2.3: Spectrum comparison between UWB and narrowband systems, [4].

---

where, c is the speed of light, BW is the bandwidth of the radar pulse in frequency domain and τ the bandwidth in time domain. With this type of radar is possible to calculate the distance to target d_T (equation (2.10)), [8]:

$$d_T = \frac{\Delta t * c}{2} \tag{2.10}$$

where Δt is the delay between the transmitted and the received signal.

Applications of the UWB radars encompasses material boundaries detection (due to the large range of different wavelengths that can be used) and motion detection. With this type of technology it is possible to perceive breathing signals, once their periodic motion causes also periodic changes in the received signal. This periodic change is reflected across multiple scans that are compared with a reference scan in order to locate the target. It is also possible to detect the subject's respiration behind walls, due to the wavelengths that can be used, [4].

2.1.2 Software Defined Radio

The SDR systems used in radio communications can be digitally configured, via software control, the hardware components of the front-end such as amplifiers, modulators, demodulators, mixers, etc, and thus establish a connection between the user and the radar.

Regarding the generic SDR configuration shown in Figure 2.4, its operation can be separated in the Tx and Rx chain. The transmitter generates a waveform digitally which is converted from digital to analog using a Digital to Analog Converter (DAC) and then up-convert it to RF before its transmission. The receiver does the down-conversion of the analog received signal to baseband or to an Intermediate Frequency (IF) (depending on the receiver architecture, that will be discussed in section 2.3.1) and then converts to digital using an Analog to Digital Converter (ADC). In the end, the signal processing can be done in the user's computer, using specific drivers and compatible applications supported by the device manufacturer. In section 2.4 we will analyse some generic hardware based radars, which are developed for a specific task and can not be reconfigured. SDR have dedicated hardware only to antennas, DAC , ADC, the mixing stage (for up and down-conversion) and a FPGA to reduce the computational burden of the computer during the signals process, [8]. The remain processing is performed by software, which provides great flexibility to the system.

Therefore, advantages of using SDR as the selected radar system comprises its versatility allowing multiple application with a single radar, its faster development of complex signal processing, its compact and portable shape and its reduced price.

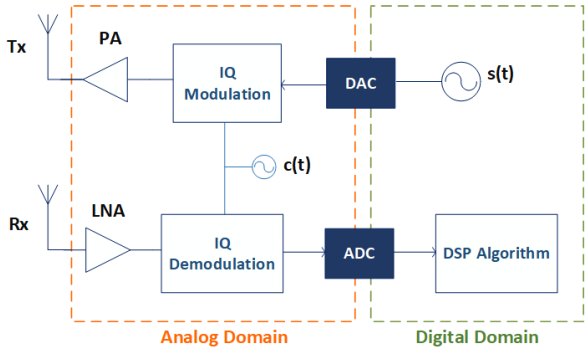

Figure 2.4: Basic block diagram of a generic SDR system.

2.2 Heart and Respiratory Surface Motion

This dissertation aims to build a prototype of a bio-radar capable to detect and measure bio-signals that actuate in the chest area, for example the respiratory and the heartbeat signal. In this section, an introduction to the respiratory and heart systems are made, with focus on their motions and how they can be detected in the skin surface by the radar. First, the respiratory system is mentioned where the displacement of the muscles and bones involved in the breathing function is detailed. Finally, a general overview about the heart system is done, where the agents that cause the motion in the chest are identified. Once the final prototype is focused in the respiratory signal and only some alternate methods for the heartbeat's signal extraction are briefly mentioned, the heart system is not deeply studied.

2.2.1 Respiratory System

The respiratory system has as primary function the gas exchange, where the air with carbon dioxide should be expelled from the body and the air with oxygen should be inhaled. The respiratory system also helps to keep the acid-base levels balanced, [4].

The ventilation level is controlled by the central nervous system and it comprises the respiratory rate and the change of the tidal volume. The respiratory function can be influenced by other organ systems, thus it is directly connected with the healthy state of the total body. The evaluation of the respiratory rate and other related parameters such as the breathing rhythm, regularity, depth and volume can reveal some disorders that can be avoided, controlled or even treated if monitored continuously and detected in good time. Some disorder examples are presented below, [4]:

- Cardiorespiratory diseases;
- Acute respiratory distress syndrome;
- Pulmonary edema and embolism;
- Chronic obstructive pulmonary disease;
- Severe heart failure;
- Systemic inflammation;

- Low blood volume;
- Malfunctions of the excretory system or of the central nervous system.

During the breathing function, muscles contract and cause changes in the thorax volume. This volume change generates pressure differences between the thorax and the external environment, hence the air moves inside or outside the lungs going from the higher level of pressure to the lowest. The breathing function can be easily detected in the chest-wall skin surface.

During normal breathing, muscles contract during inspiration but not in the expiration, i.e. there is not an implied effort for the normal expiration. For the inspiration the diaphragm contracts, the thorax elongates and the volume increases pushing the abdominal area forward. Figure 2.5, shows the chest cavity behaviour during inspiration and expiration. Normal respiration cause a diaphragm extension equal to 1-2 cm and deep respiration 10 cm.

During inspiration, the ribcage presents displacements in different levels, hence its radium changes as the thorax diameter. The ribcage motion characterization is present in Figure 2.6 and outlined below, [4]:

1. The upper ribs causes the dominant motion and is called "pump-handle". It consists in a rotation around their long axis;
2. The lower ribs motion is named "bucket-handle" and is caused by its rotation and glide;
3. The lowest ribs, also known as floating ribs are not connected to the sternum and their displacement is called "caliper" motion.

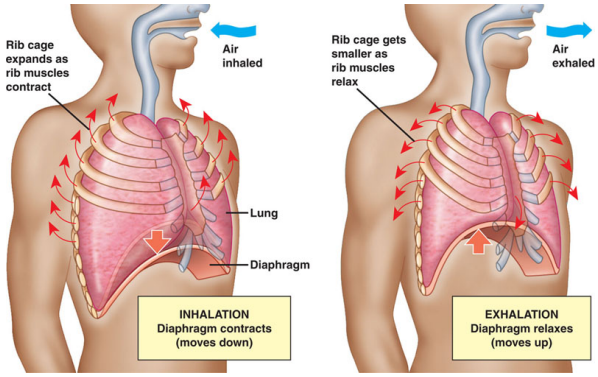

Figure 2.5: Inspiration and expiration action and all involved parties, [9].

Expiration decreases the tidal volume naturally by the alveoli recoil, if the subject is breathing normally. On the other hand, if the subject is speaking, singing, coughing or sneezing, a forced expiration is required and abdominal muscles must contract in order to increase the abdominal pressure and the abdomen content is pushed against the diaphragm. The abdominal muscles contraction depresses the lower ribs and pull them down, decreasing the thorax volume.

The chest-wall motion is caused by the combination of the abdominal and ribcage motions. By observing the chest-wall behaviour during the breathing function in multiple angles (back/front, left/right and up/down) it is possible to conclude that the biggest displacement is caused by the sternum (approximately 4.3 mm) and by the navel (approximately 4.03

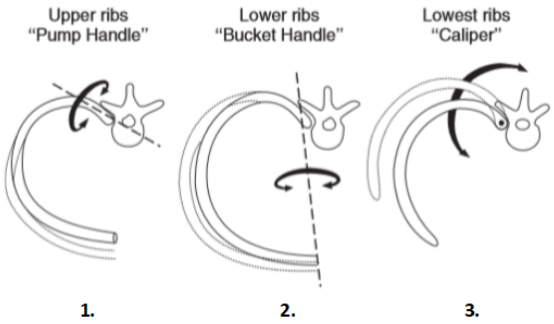

Figure 2.6: Motion of the ribcage, [4].

mm). With the tidal volume variance and the abdominal motion measurements during normal breathing, presented in [4], it was possible to conclude that the total radial thorax expansion is 4-12 mm, depending on the body structure of the subject.

In [4] a study is referred, where 65 healthy people are monitored having in mind features related to the breathing pattern: the respiratory rate, tidal movement, inspiration and expiration time, and finally the ribcage and abdominal excursion. They concluded that young adults have a regular breathing pattern, in contrast with older adults which have less regular breathing patterns, with significant variations in tidal volume and they also presented brief central apnea periods. The breathing rate average was 16.6 ± 2.8 Breaths/min, i.e. approximately 0.3 Hz.

2.2.2 Heart System

The heart is the organ responsible to distribute blood, through the lungs and to all body tissues. Its continuous contraction and expansion generates a changing pressure that drives blood flow. The heart, which is located in the chest cavity, during the beating rotates and changes size, causing motion in the chest-wall that can be sensed in the skin surface by a non-contact sensors and palpation, [4].

Beneath all the auricles and ventricles contraction and relaxation, the motion caused by the left ventricle is the one that causes a larger displacement, perceived in the chest-wall surface. Usually, motion of the right ventricle can not be detected, in healthy patients, by palpation. As the heart contracts, its shape become spherical and its diameter increases adding more impulse against the chest. With the contraction it rotates, causing the lower front part of the left ventricle to strike the chest-wall front, [3]. In healthy subjects, there is a Point of Maximal Impulse (PMI), where the impulse caused by the left ventricular can be easily detected. This point is above the anatomical apex, in the fourth and fifth intercostal spaces from the left mid-clavicular line (see Figure 2.7).

In order to prove that is possible to detect heartbeat in the chest-wall surface, measurements using a single point laser displacement were conducted, for instance in [10], and results show that the heart displacement in the PMI is approximately 0.6 ± 0.2 mm. However, this value should vary widely according with the subject's health, physiology and age.

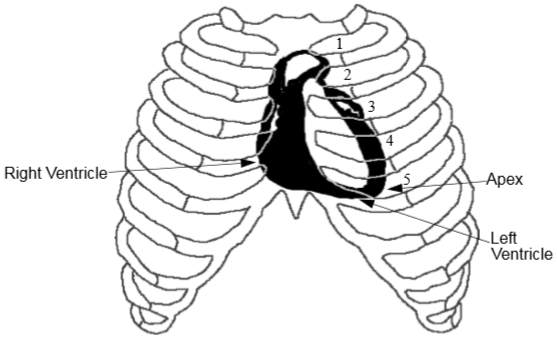

Figure 2.7: Location of the heart on the ribcage, [3].

2.3 Full Front-end Description

This section consists in an introduction to the bio-radar architecture. Firstly a SDR technology overview is done, with the main focus on important physical features such as receiver architecture, antennas and the carrier frequency selection, once they influence the recovered bio-signals. Also some implementations already done in other projects are presented, that gather a state of the art of bio-radar systems.

2.3.1 Receiver Architectures

The front-end architecture selection aims to guarantee maximum sensitivity, to enlarge detection range and to eliminate baseband interferences and noise, [1]. Over the years heterodyne architecture has been used as radio receivers due to its versatility and easy tuning characteristics that ensures maximum quality. However, nowadays simplicity and low-cost components features are even more required. In this section, some receiver architectures are presented as alternative solutions and the motivation to have selected the homodyne receiver for this application is presented.

Heterodyne Receiver Architecture

The operating principle of this architecture is to mix the received signal in the Local Oscillator (LO) with a signal which its frequency is different from the incoming signal. In this way the wave is down-converted to an IF, instead to the baseband. The tunable characteristics can be made in the LO stage, by changing the LO signal frequency in order to assure optimal IF gain and high quality filter stage, [3]. Figure 2.8 shows this architecture that is explained bellow.

After its reception, the received RF signal is bandpass filtered in order to reject the image frequency. Self-image problem is a parasitic spectral component formed by the superposition of both sidebands from the real signal when is converted to IF, [3], and it will be explained in more detail later when we will discuss some receptor constrains (section 2.3.2). Afterwards, the noise figure existent on the receptor chain input is reduced, using a Low-Noise Amplifier (LNA) that increases the signal power and hence the noise is decreased, [3]. Once located in the IF, signal is isolated from the nearby channels by using a bandpass filter around the IF and amplified with the necessary gain to guarantee accurate results during the remain DSP algorithm, represented by the last block.

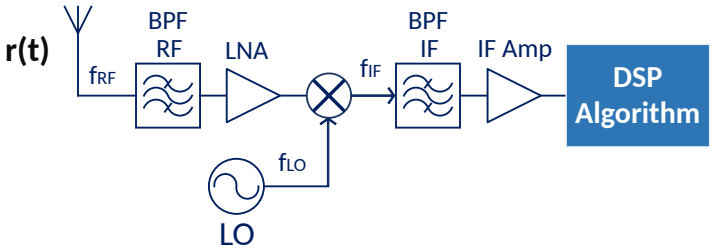

Figure 2.8: Heterodyne receiver architecture.

Usually this architecture presents better robustness in terms of DC component because it does not work in baseband rather then homodyne receivers as we will see further.

Homodyne Receiver Architecture

This type of receiver mixes the received signal with the LO signal using the same carrier frequency and thus down-conversion directly to baseband is performed. Therefore it can also be called as direct-conversion receiver and its architecture is shown in Figure 2.9.

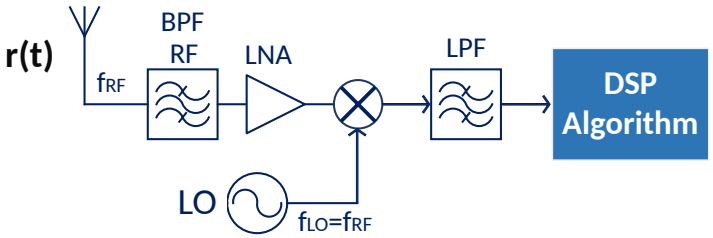

Figure 2.9: Homodyne receiver architecture.

Bandpass filter and LNA reduces the noise figure of the incoming signal by isolating it from the surrounding spectral components and amplifying the signal power. Subsequently the signal is down-converted using a portion from the transmitted signal, providing correlation between both signals in the mixer. Range correlation effect is achieved due to these conditions and baseband noise caused by mismatch in hardware components, also known as phase and amplitude noise, can be rejected (this issue is studied later, in section 3.2.1). In the end, the resultant baseband signal is low-pass filtered.

This is the architecture chosen for the prototype developed in the framework of this dissertation, once the used board that performs the front-end has this architecture configuration. This architecture is also simple to implement and it does not require a complex hardware, rather than heterodyne architecture. A direct-converter receiver is implemented in quadrature hence the self-image and null-detection point problems are avoid, as we shall see.

2.3.2 Receptor Constrains

The Doppler radar architectures proposed in early times were based in single channel receivers due to its simplicity and sufficient accuracy to extract vital signals with precision [4]. An example of this architecture is presented in Figure 2.10.

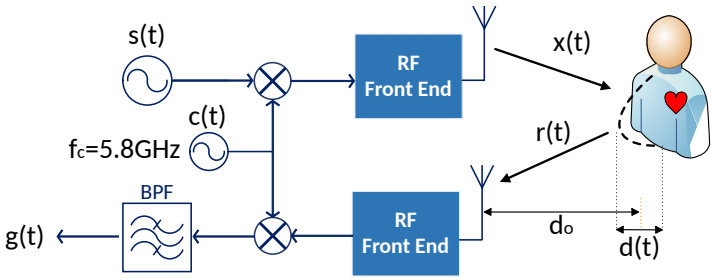

Figure 2.10: Simplified Doppler radar model with single channel receiver [11].

The single channel receiver output is proportional to the phase change, so signal's extraction can be performed directly without any other demodulation method. However, with only one output, the receiver has to deal with real signals that assign sensitivity to target's static position relative to the radar. The initial phase angle of the received signal depends only on the nominal position d_o, as described by the equation (2.11) [12].

$$\theta_i = \frac{4\pi d_o}{\lambda} + \Theta \tag{2.11}$$

where λ represents the wavelength and the constant Θ is the phase shift at the target's surface and encompass the distance between the mixer and the antenna [11].

In phase demodulation, the value of d_o can cause two cases of extreme point detection, so called "null" and "optimum" points. This happens because different positions of the target imply a variant delay in the received signal, when comparing with the LO signal, where is used a portion of the transmitted one for down-conversion. Delay is perceived as phase change in $r(t)$ signal. Regarding radar full range, these extreme cases occur periodically, at each $\lambda/4$ from the antenna, where "null" and "optimum" points are interleaved and separated $\lambda/8$ [13], as illustrated in Figure 2.11:

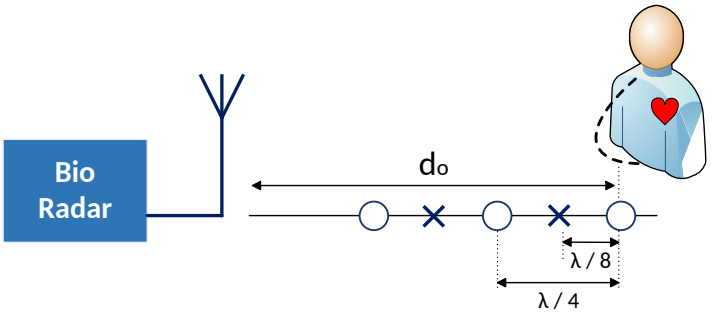

Figure 2.11: Radar range organization concerning extreme points of detection. Crosses represent null points and circles represent optimum points [4].

The mathematical explanation for the these extreme detection cases stands as follows [4], [11]: the baseband signal is real and its sinusoidal form is written as equation (2.12),

$$g(t) = A_r \cos\Big(\theta_i + \varphi_r(t)\Big) \tag{2.12}$$

where θ_i is the initial phase angle expressed by the equation (2.11) and the time-varying chest-wall displacement is denominated as $\varphi_r(t) = 4\pi d(t)/\lambda$. Regarding the Figure 2.11, null

points occur in every θ_i integer and multiple of π. Therefore, this occurs every multiple of quarter of wavelength, or in other terms for

$$d_o = \frac{n}{4}\lambda, n \in \mathbb{N} \tag{2.13}$$

This null point occurs everytime the received signal $r(t)$ and the LO are in phase or 180° out of phase [11]. By substituting this d_o value in the equation (2.12), neglecting the initial phase shift Θ from equation (2.11) and considering that small angle approximation is valid (i.e. $d(t) \ll \lambda$), it is easy to verify mathematically the null effect in phase demodulation result. The baseband signal is rewritten as

$$g(t) = A_r \cos\Big(\frac{4\pi}{\lambda}\frac{n\lambda}{4} + \varphi_r(t)\Big) = A_r \cos\Big(\pi n + \varphi_r(t)\Big) = \pm A_r \cos\Big(\varphi_r(t)\Big) \tag{2.14}$$

Regarding Taylor series expansion of the cosine function (2.15), it is possible to obtain an approximative solution.

$$\cos(x) = \sum_{k=0}^{\infty} \frac{(-1)^k}{(2k)!} x^{2k} \tag{2.15}$$

$$g(t) = \pm A_r \left(\sum_{k=0}^{\infty} \frac{(-1)^k}{(2k)!} \Big(\varphi_r(t)\Big)^{2k} \right) = \pm A_r \mp A_r \frac{\varphi_r(t)^2}{2!} \approx \pm A_r \tag{2.16}$$

This result shows that for this target's position, the baseband signal is approximately constant hence is not linearly proportional to the subject chest-wall displacement and it results in a large DC component in baseband. Having in mind that the recovered phase data comprises heart and respiration motions, in null point both could be self or mutually coupled, resulting in a large detection inaccuracy [13]. The square terms in expression (2.16) means doubling the signal frequency which leads to signal distortion and SNR degradation.

On the other hand, for every θ_i value odd and multiple of $\pi/2$, the receiver faces an optimum detection point, that occurs more specifically for

$$d_o = \frac{2n+1}{8}\lambda \tag{2.17}$$

The baseband signal (2.12) is now rewritten as

$$g(t) = A_r \cos\Big(\frac{4\pi}{\lambda}\frac{(2n+1)\lambda}{8} + \varphi_r(t)\Big) = A_r \cos\Big(\pi n + \frac{\pi}{2} + \varphi_r(t)\Big) = \pm A_r \sin\Big(\varphi_r(t)\Big) \tag{2.18}$$

Following the previous procedure, concerning Taylor series expansion of the sine function (2.19), the approximative solution is now (2.20):

$$\sin(x) = \sum_{k=0}^{\infty} \frac{(-1)^k}{(2k+1)!} x^{2k+1} \tag{2.19}$$

$$g(t) = \pm A_r \left(\sum_{k=0}^{\infty} \frac{(-1)^k}{(2k+1)!} \Big(\varphi_r(t)\Big)^{2k+1} \right) \approx \pm A_r \varphi_r(t) \tag{2.20}$$

In this case, the phase demodulation result is linearly proportional to the periodic chest-wall motion and thus signal can be extracted successfully.

In order to overcome the null points issue, a primary approach was proposed by [11] using quadrature Doppler radar receiver with channel selection, where the received signal is split in two chains with phase relation of 90°, resulting in two quadrature outputs (2.21) [4], that can be combined for optimal detection. This method can also be called as linear demodulation and is explained in section 3.3.1.

$$\begin{aligned} g_I(t) &= \cos\Big(\theta_i + \varphi_r(t)\Big) \\ g_Q(t) &= \cos\Big(\theta_i + \varphi_r(t) - \frac{\pi}{2}\Big) = \sin\Big(\theta_i + \varphi_r(t)\Big) \end{aligned} \tag{2.21}$$

If equations (2.13) and (2.17) are substituted in both quadrature components from equation (2.21), it can be verified that when the subject is located at null position in the in-phase (I) channel, it is located at optimum position in quadrature (Q) channel and vice-versa. Thus there is always at least one output that is not in null position. The receiver with channel selection tracks both channels and select the one that is in optimum point. If both channels are at optimum points, the outputs are added [4]. In [13] an experiment is conducted in order to show signal's behaviour in each channel for null and optimum points. A common effect caused by null points are drop-out regions in the extracted signal from the damaged channel, that occurs due to signal power degradation. Another consequence of null point deterioration is the variability in both heart and respiratory rate, being even possible to be mixed with each other.

Single-channel receiver like the one illustrated in Figure 2.10, performs down-conversion using a cosine signal in the LO, which results in a baseband output vulnerable to spectrum folding and self-image problem [4]. This happens because a real signal in frequency domain contains both positive and negative frequency components, as stated from Euler's equations (equation (2.22)):

$$\begin{aligned} \cos(\omega_o t) &= \frac{1}{2}(e^{j\omega_o t} + e^{-j\omega_o t}) \\ \sin(\omega_o t) &= \frac{1}{2j}(e^{j\omega_o t} - e^{-j\omega_o t}) \end{aligned} \tag{2.22}$$

Therefore, baseband signal contains both positive and negative frequency components overlapped that causes self-interference. A representation of this issue is presented in Figure 2.12.

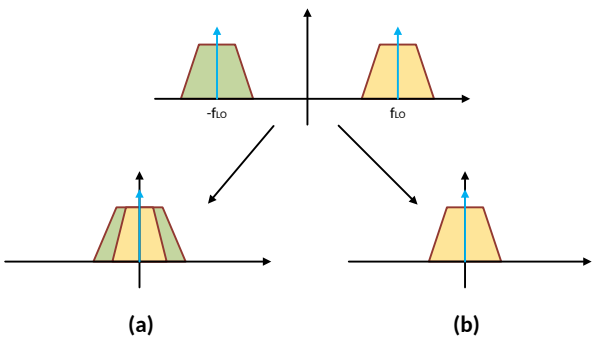

Figure 2.12: Down-conversion result: (a) With self-image problem representation (b) Without self-image problem.

The better solution to overcome the self-image issue in the baseband signal is by using quadrature receiver that combines simultaneously I and Q components, rather than optimal channel selection. Thus, the RF signal is mixed with a complex exponential which results in only one frequency component present in baseband.

Furthermore, this architecture provides two orthonormal outputs that ensures always at least one channel in optimum point. With the quadrature outputs combination is possible to achieve an accurate phase demodulation, where the target position does not have any influence because the extracted signal is always linearly proportional to the time varying phase shift caused by target's motion [13].

2.3.3 Antennas

For the purpose of this project and due the specific signal's characteristics, antennas should be designed with certain specifications to guarantee maximum directivity and narrow beam width that avoids the reception of undesired clutter reflections. However, a special care with the beam width should be made, once with the narrow beams it is difficult to focus properly in the subject's chest area, specially in case of small chest cavities or if the subject is moving. The application scenario of this dissertation is focused in cases of continuous monitoring with stable patients or only with shallow movements (bedridden patients, for instance), therefore directive antennas can be used, [12],[3].

The antennas design should also have in consideration the balance between directivity and size. As mentioned previously, highly directive antennas should be used, however it requires larger dimensions and hence increase the near-field area [4]. Large dimension antennas confer a less portable system, revealing another disadvantage.

Other point of interest is the number of antennas connected in the front-end, [3]. There are two possible alternatives: on the one hand is possible to use a single antenna for both transmission and reception using a circulator to isolate both signals. On the other hand, two antennas could be used for transmission and reception separately. The first option confers more directivity with only one beam being used, although it carries more production costs. The second option is cheaper in terms of mass-production, nonetheless its design and angle can affect isolation and RCS. If both antennas are closer enough, these effects can be decreased.

2.3.4 Frequency Selection

The selection of the carrier frequency is an important matter because it affects the fundamental operation and influences physical characteristics in the transmitting environment such as antenna size, possible range for target detection and the resolution (i.e the carrier wavelength influence in the amount of phase modulation). The phase modulation is represented by the length of the formed arc in the complex plot, as we will see with more detail in chapter 3. With higher frequency bigger is the arc length and it is easier to achieve full 2π phase rotation in the complex circle [4]. Larger arc lengths requires non-linear channel combination for phase demodulation, once the small angle approximation is not verified anymore and hence linear demodulation can not be used.

In [12] a performance comparison is made between high and low frequency carrier, using 10 GHz and 2.5 GHz radar respectively. Advantages in the usage of high frequencies are identified, for instance the increase of SNR and the possibility to use more compact and portable radar modules, because smaller size antennas can produce same gain and directivity

using higher frequencies. This can be ensured because for higher frequency, smaller is the wavelength and the far-field limit is closer to the antenna, [4]. In chapter 5 is described an experiment conducted for the prototype validation, where both carrier and antenna directivity impact are demonstrated. High frequencies also maintain full beam radiating properties for longer distances and increase RCS. Nonetheless, higher carrier frequencies difficult the measurement of respiration and heart-beat simultaneously, [1].

In order to compliance FCC, an unlicensed band should be chosen, [4]. In the context of this project, the unlicensed band of $5.725 - 5.875$ GHz is going to be used, because once this dissertation does not focus deeply in the hardware (antennas) characteristic, but in DSP algorithms instead, the available material to built the prototype required this frequency of operation. Also it is a frequency whose features are not severely affected by the low frequency and neither high frequency constrains.

2.4 Related Hardware Systems

In this section, an overview of the implemented bio-radars is made, regarding the used hardware. Some of the papers presented in this section had the aim to find better solutions for DSP algorithms to extract vital signals. For now, only their set-up characterization is done and later, in chapter 3, the signal processing state of the art is made in order to present possible solutions to the acquired signal constrains.

The timeline of this system's hardware advancement can be divided in three main stages:

1. Transceivers composed by single RF hardware components interconnected with each other;

2. Transceivers implemented on-chip with CMOS process;

3. Full radar modules able to transmit, receive and process the acquired signals with the parameters configuration performed digitally.

Non-invasive monitoring was firstly presented in the 1970's, where [14], [15] and [16] proposes microwave radars for respiration measurement, as well as, heartbeat measurement. The heartbeat signal was measured in separate during breath hold periods. For the monitoring system was used a X-band sweep oscillator with horn antennas. This system was tested in animals, where in [15], they were anaesthetized and intubated with the aim to control their respiration pattern, and thus detect apnea or hyperventilation cases. In [16] was used a CW radar with 2 GHz antenna that was located at 3 cm above the apex so the heart motion could be detected.

Recent advances in this field aim to find solutions based on trade-offs to guarantee small dimensions, low power consumption, straightforward implementation in both hardware and software levels and accurate results. In [13], [17] and [18] experiments were conducted to verify the effect of single-channel null point detection mentioned in section 2.3.2. In addiction, a set-up was proposed regarding the quadrature receiver, the demodulation mode and some extract signal's compensations that will be explored in chapter 3. The same set-up was used in [13], [17] and [18] (see Figure 2.13) and it was composed by a direct conversion quadrature Doppler system with the following components:

- Single antenna for both Tx and Rx, more specifically a 2.4 GHz patch antenna;

- Voltage-controlled oscillator (VCO) as LO to provide signal source for signal's modulation in the transmission chain and demodulation in the receptor chain;
- Circulator used to isolate transmitted and received signals;
- The LO signal is divided in RF and LO signals by using a signal splitter, for signal transmission (RF output) or for mixers (LO output);
- The received signal and the LO signal are divided using a two-way 0° and 90° power splitters, in order to create quadrature outputs;
- Baseband pre-amplification stage by using a LNA and bandpass filtration;
- Analog signals are digitized using an ADC card.

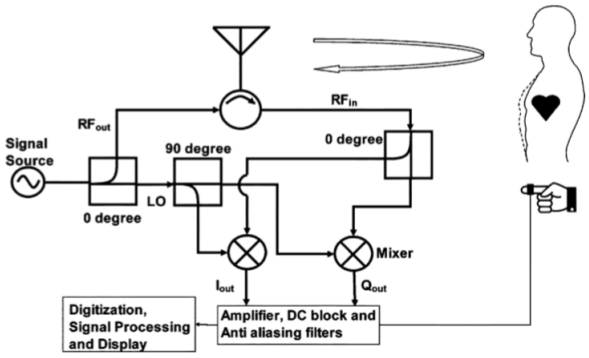

Figure 2.13: Bio-radar set-up used in [13], [17] and [18].

Later, the DSP is performed in MATLAB, where the vital signals are recovered and its rate is computed. In order to validate the accuracy of the extracted heartbeat signal a wired finger pressure pulse sensor (Piezoelectric Pulse Transducer, UFI 1010) was used.

In [19] experiments demonstrated that large motion can be used to calibrate the bio-radar system, allowing it to detect smaller displacement. For this purpose, the set-up included the bio-radar system and a mechanical target moved by a linear stage (Griffin Motion MLS series) that simulates the subject chest-wall. This simulator was needed to establish a reference to the measurement. The Doppler radar used was similar to the previously described in [13], [17] and [18]: it was composed by a 2.4 GHz Antenna, 0° and 90° power splitters, Mini-Circuit mixers and the same LO as signal source for both Tx and Rx channels. The data was recorded by a DAC NI-USB 6259 and processed in LabVIEW at a sampling rate of 1kHz. The simulator moved with different and increasing amplitudes of the linear stage for calibration purposes. The prototype developed in this dissertation needed also a calibration system, thus a CWS was developed and it will be explained in chapter 4.

An important milestone in the bio-radar development was the integration of RF front-end components in a single and small chip, which is more compact, lightweight and with low cost production, [1].

The first proposed on-chip radar for vital signals acquirement was implemented in a 0.25-μm CMOS process, operating at 1.6 GHz with single-channel receiver, [20], [21]. Another

similar implementation used a quadrature receiver, at 2.4 GHz and it improved the null point detection, [11]. As an example, in Figure 2.14 is shown the block diagram of the implemented RF circuit on-chip from paper, [11].

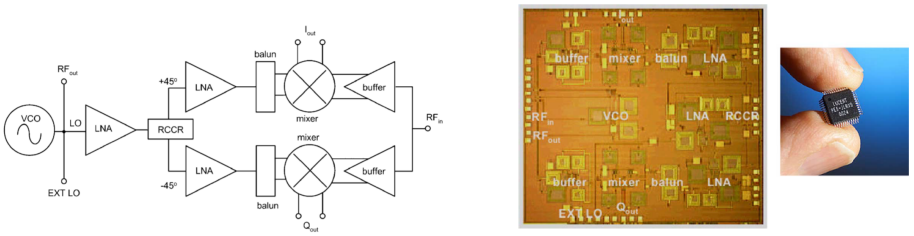

(a) (b)

Figure 2.14: (a) Block diagram of the implemented quadrature transceiver on-chip in [11]. (b) First noncontact physiological motion sensor chip using quadrature receiver architecture, [1].

Other different implementations were proposed with a trend the reduce the chip sizes. For instance, in [22] a double-sideband receiver was used in a 0.18-μm process and in [23] a high-sensitivity receiver chip is integrated in a 0.13-μm process. The developed systems presented so far in this paragraph could measure the physiological motion of the target within a range of 50 cm. In order to test the chip efficiency, external components were also needed, for instance in [11] they used a power splitter to provide isolation between the input and output signals, and the baseband output was filtered and amplified by using an external LNA, (see Figure 2.15). Finally, the acquired signals were then processed in MATLAB, in order to compute their rate.

A deep study about single chip implementation is done by Droitcour in [3].

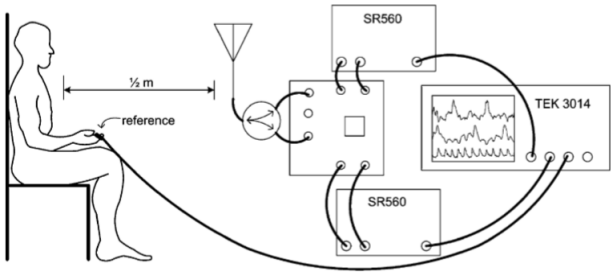

Figure 2.15: Experiment set-up for bio-signals measurement with the developed chip in [11].

In [24] a bio-radar prototype with DSP embedded hardware is proposed. The hardware is divided in two modules: the RF circuit with a similar configuration as the previously presented in Figure 2.13 and the baseband signal processor that performs an Arctangent Demodulation (AT) (explained further in chapter 3), the filter stage (to separate heart signal from breathing signal) and the rate computation from the extracted signals. This last module is implemented by a Texas Instruments C6000 series DSP. Signals are digitized by an external 12 bit ADC. The rate finding is computed using MATLAB, that has as input exported data from a RS232 connection available in the NI C600 DSP board.

Currently, some experiments were performed in order to validate some DSP algorithm specifications. In this framework more compact radar systems were used. For instance in [25] an experiment is made to verify the autocorrelation method efficiency. For this aim a 10 GHz Doppler radar was used (from New Japan Radio Co., Ltd), with a patch antenna. The received signal is then digitized at a sampling frequency equal to 100 Hz, via 12-bits ADC card. Before autocorrelation computation, signal processing was made using LabVIEW. Another example is presented in [12] where a comparison of some centre estimation algorithms is done using a similar set-up used in [25]: the radar was implemented by using quadrature modules from Microwave Solutions, Ltd, with integrated 10 GHz patch antennas. The received data is sampled at a sampling rate equal to 800Hz, with a 24-bit ADC (from Icraft).

Finally, in [2] and [26] a bio-radar implementation was proposed, using a front-end based in SDR. It was executed with an USRP B200 board, developed by Ettus Research, with an Analog Devices chip that concentrates the RF front-end components, like the chip example in Figure 2.14. This hardware solution will be the selected for this dissertation prototype. As mentioned previously in section 2.1.2 and as will also be seen in chapter 4, this board allows the digital configuration of its input and outputs (receiver and transmitter), regarding the required frequency and sampling rate of the current application. The transmitted signal can be generated digitally, then is up-converted before the transmission and down-converted after its reception. The output signal is digital and already in baseband. These configurable systems present an advantage regarding the previously referred ones, due to its flexibility and compact devices. In chapter 3, a study of the hardware as a problem source is done and is concluded that the implementation with front-end based in SDR can solve some problems, such as the phase noise.

Chapter 3

Architecture Definition

The main objective of this thesis is to study bio-radar systems and develop a real-time prototype which proves that this concept can be applied in real scenarios. Thus, this chapter aims to define the architecture implemented to built the prototype.

This chapter is going to be divided in the following sections: firstly, a mathematical model that synthesises the bio-radar system behaviour is presented, as well as a DSP algorithm proposal for bio-signal's information recovery, considering an ideal scenario, i.e. without any sources of disturbance. Furthermore, both model and algorithm will be tested with the same ideal conditions, using simulated signals generated in MATLAB software and taking into account all the signal characteristics. Their impact in the system's performance will be studied by varying their value during the simulation.

Subsequently, a real scenario is going to be considered. Each source of signal distortion is going to be exploited by representing its mathematical model, simulate it in MATLAB and some solutions are presented, pointing out the one choose for this application.

Finally, and also considering a real scenario, methods for phase demodulation and rate computation are discussed.

In section 3.5, a final simulation is performed combining the selected methods for DC offset cancellation, phase demodulation and bio-signal rate estimation. The simulation aims to prove that the selected methods are suitable for the presented bio-radar model. As mentioned in chapter 1, the proof of concept embraces only the respiratory signal, so the heartbeat signal will be neglected in this chapter.

Later in this thesis, in chapter 5, experimental tests will be performed in order to validate the efficiency of this model. These tests will be supported by a CWS built for this purpose and also with real signals acquired by the bio-radar prototype developed during this dissertation.

The overall bio-radar's system is described in Figure 3.1. The bio-radar's system is composed by a CW Doppler radar which continuously transmits a sinusoidal carrier, generated digitally and receives the echo from the reflecting target. Due to the Doppler effect, there is a phase change as the subject's chest-wall moves towards or away from the radar and hence a phase modulation in the received signal is created [4]. The main goal of this system is to measure the respiratory and heartbeat rate. This information can be obtained by the phase extraction of the received signal.

Bio-signals have low amplitude and its bandwidth occupies very low frequency ranges close to DC, hence they are highly sensitive to several sources of noise, such as clutter from the scenario reflections. Regarding Figure 3.1, the *DSP Module* performs an algorithm developed

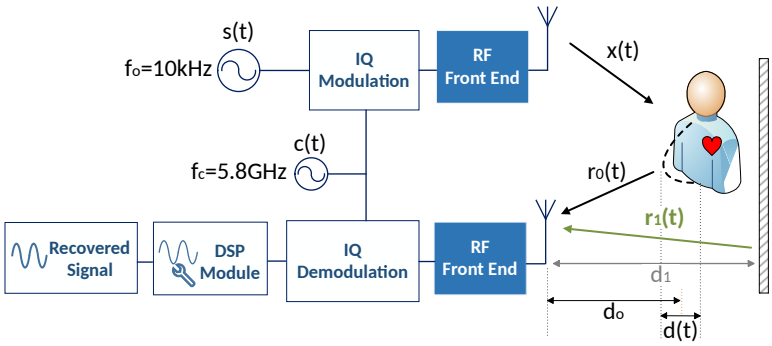

Figure 3.1: Block diagram of the bio-radar's system.

for the accurate bio-signals information extraction, taking into account its strict features. Finally, the *Recovered Signal Module* displays in real-time the respiratory signal and computes its rate. The methods for the rate's computation are presented in this chapter, in section 3.4. The real-time displaying module, performed by the demonstrator will be described in chapter 4.

3.1 Bio-Radar Mathematical Model

Firstly in this section, system signals will be defined considering an ideal scenario where the only source of disturbance are the parasitic reflections from nearby standing objects. Figure 3.2 shows the bio-radar system, more specifically the DSP algorithm implemented in the receptor chain. Each module have in its output a specific signal that is going to be defined in this section. Their mathematical representation has into account the architecture of the SDR board used in this dissertation, which is detailed in chapter 4. It means that signals in analog and digital domain are distinguished: analog signals are expressed in time domain and digital signals are expressed in discrete time domain. This assumption can be made if we assume that blocks *IQ Modulation* and *IQ Demodulation*, in figure 3.2, include a DAC and an ADC, respectively.

Later, the simulation of the described model is going to be performed with simulated signals using MATLAB. The RF signal $s(n)$, is generated digitally with an offset of $f_o =$

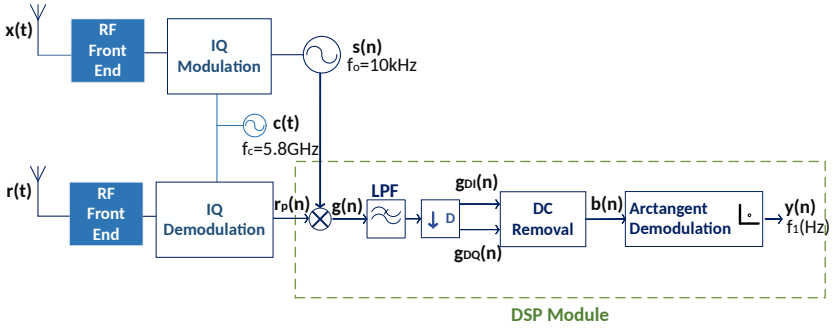

Figure 3.2: Block diagram of the system including the DSP module content.

10kHz, due to some hardware specifications that will be discussed in the next section. It is

given by the equation (3.1):

$$s(n) = e^{j\omega_0 n} \tag{3.1}$$

with $\omega_o = 2\pi f_o$, where the offset f_o is the frequency of operation. Before its transmission toward the target, and already in analog domain, the $s(t)$ signal is modulated In-phase and Quadrature (IQ) with the carrier $c(t) = \cos(\omega_c t)$, $f_c = 5.8$GHz, resulting in the signal $x(t)$, expressed by (3.2).

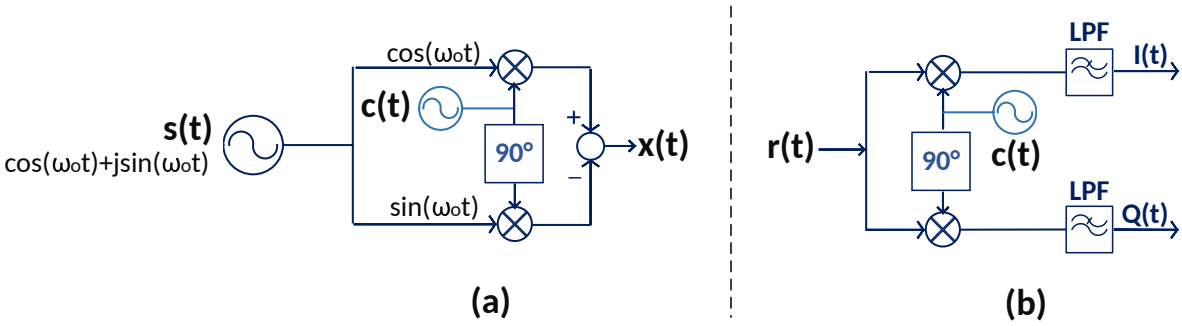

Figure 3.3: In-phase and Quadrature: (a) Modulator, (b) Demodulator.

Both IQ modulation and demodulation procedures are shown in Figure 3.3.

$$\begin{aligned} x(t) &= \cos(\omega_0 t)\cos(\omega_c t) - \sin(\omega_0 t)\sin(\omega_c t) \\ &= \cos((\omega_0 + \omega_c)t) \end{aligned} \tag{3.2}$$

Regarding Figure 3.1, the received signal combines the reflection from the subject's chest-wall, $r_0(t)$, and the parasitic component, $r_1(t)$. Thus, it can be expressed as:

$$\begin{aligned} r(t) &= r_0(t) + r_1(t) = \\ &= A_0\cos((\omega_0 + \omega_c)t + \varphi(t)) + A_1\cos((\omega_0 + \omega_c)t + \theta_1) \end{aligned} \tag{3.3}$$

where A_0 and A_1 are the amplitudes of both reflected signals, and θ_1 represents the total path travelled by the parasitic reflection. The phase change function that contains the respiratory information is represented by $\varphi(t)$. The chest-wall motion changes the wave's travelled distance and hence modulates the reflected signal. Having in mind the Doppler effect presented on chapter 2, there is a relation between the wavelength λ and the phase change, which consists in 2π per wavelength. Therefore, the two-way path distance is related to the phase due to the number of wavelength per second captured by the receiver [4]. As result of this relation, considering a stationary target, the phase change due to the Doppler effect follows the relation (3.4):

$$\theta = \frac{2\pi}{\lambda}(2d_o) \tag{3.4}$$

where d_o is the distance between the target and the radar. Considering now, that the target is a person, the phase change function is divided by two main components [1]:

- The stationary two-way path travelled by the wave (Eq. (3.5)) which includes the constant phase shift, Θ, [11]:

$$\theta_0 = \theta + \Theta \tag{3.5}$$

- The chest movement described as a low frequency sinusoidal signal, described by the equation (3.6):

$$d(t) = a_r \cos(2\pi f_1 t) \tag{3.6}$$

Thus, the total phase change function can now be described by the equation (3.7):

$$\varphi(t) = \theta_0 + \frac{2\pi}{\lambda}(2d(t)) = \left(\frac{4\pi d_o}{\lambda} + \Theta\right) + \frac{4\pi d(t)}{\lambda} \tag{3.7}$$

For now we are going to assume an ideal scenario, so the *DC Removal* block in Figure 3.2 and the parasitic component $r_1(t)$ are neglected.

In the next stage of the receptor chain, the received signal is down-converted to baseband in two steps:

1. IQ demodulation, where the information from reflections is recovered from the modulated carrier wave. Figure 3.3 shows the IQ demodulator's architecture. In this step, the demodulated signal $r_p(t)$ is expressed as a complex signal with the ω_o component and is represented by the equations (3.8) and (3.9):

$$r_p(t) = I(t) + j * Q(t) \tag{3.8}$$

$$r_p(t) = \frac{A_0}{2} e^{-j(\omega_0 t + \varphi(t))} \tag{3.9}$$

2. The offset $f_o = 10\text{kHz}$ created for the signal $s(n)$, should be cancelled in order to get the signal in baseband. This process is done with digital signals, so from now on they are represented in discrete time domain. For this purpose, the baseband signal, $g(n)$ is the result of the multiplication between $r_p(n)$ and the $s(n)$ signal. Assuming $A_r = A_o/2$, $g(n)$ is given by equation (3.10):

$$\begin{aligned} g(n) &= A_r e^{-j(\omega_0 n + \varphi(n))} e^{j\omega_0 n} = \\ &= A_r e^{-j\varphi(n)} \end{aligned} \tag{3.10}$$

The baseband signal $g(n)$ can be decomposed in IQ components, according to the equations (3.11):

$$\begin{aligned} g_I(n) &= A_r \cos\left(\left(\frac{4\pi d_o}{\lambda} + \Theta\right) + \frac{4\pi d(n)}{\lambda}\right) \\ g_Q(n) &= A_r \sin\left(\left(\frac{4\pi d_o}{\lambda} + \Theta\right) + \frac{4\pi d(n)}{\lambda}\right) \end{aligned} \tag{3.11}$$

In chapter 2, we conclude that the respiratory rate should be within the range of 12-20 breaths per minute, i.e. between 0.2 and 0.4 Hz. Due to these narrowband and low-pass characteristics, before the phase extraction the baseband signal should be downsampled, it means that the sampling frequency should be reduced. The decimated signal is represented by the equation (3.12).

$$g(n) = g(Mn) \tag{3.12}$$

where M is the decimation factor and thus the new sampling frequency F_s is:

$$F_s = \frac{F_s}{M} \tag{3.13}$$

After that, the phase information is recovered by applying phase demodulation (*Arctangent Demodulation* block) to the downsampled signal. The phase demodulation is performed by computing the *Angle* of $g(n)$. Equation (3.14) expresses the angle computation in function of the quadrature components from $g(n)$:

$$y(n) = \angle(g(n)) = \angle(g_I(n) + jg_Q(n)) = \varphi(n) \tag{3.14}$$

3.1.1 Model Simulation

In this section a MATLAB simulation is described in order to validate the mathematical model in an ideal scenario, presented in the previous section. Propagation environment and even the system's variables have impact in the received signal and hence in the phase demodulation. Taking this information into account, this section studies the received signal behaviour using simulated signals.

The system's variables that have impact in the received signal are:

- Chest-wall's motion in meters (respiratory signal's amplitude) - a_r;
- Received signal amplitude - A_r;
- Nominal distance between the radar and the subject's chest-wall - d_o;
- Wavelength of the carrier signal - λ;
- Phase shift at the target's surface - Θ.

Simulation Procedure

1- Respiratory signal definition - $\varphi(n)$

To perform the respiratory signal established in equation (3.7), a sinusoid was generated, according to expression (3.6). The amplitude a_r corresponds to the total motion of the target around its nominal position, shown in Figure 3.4.

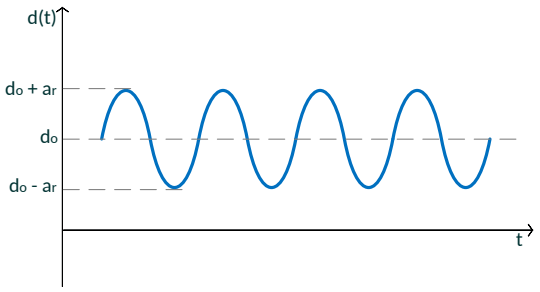

Figure 3.4: Target's motion around its nominal position.

2- Baseband signal definition and its parameters influence - $g(n)$

Considering the respiratory signal (equation (3.7)), the received signal already in baseband (equation (3.10)) can be written according to equation (3.15):

$$g(n) = A_r e^{-j((4\pi d_o/\lambda + \Theta) + 4\pi d(n)/\lambda)} \tag{3.15}$$

The simulation begins with the following parameters:

- Wavelength - $\lambda = 0.0517$ m;
- Received signal's amplitude - $A_r = 0.1$;
- Distance between the target and the radar - $d_o = 2$ m;
- Chest-wall motion's amplitude - $a_r = 0.00325$ m;
- Initial phase shift - $\Theta = \pi/12$ rad;
- Respiratory frequency - $f_1 = 0.3$ Hz;

The phase variation as consequence of the target's motion, is represented in the polar plot by an arc (Figure 3.5), where its length corresponds to the amplitude of the respiratory signal, a_r, and its radius is the received signal's amplitude A_r. In an ideal scenario the arc fits to a perfect circle centred at zero. The phase variation has direct relation with the wavelength

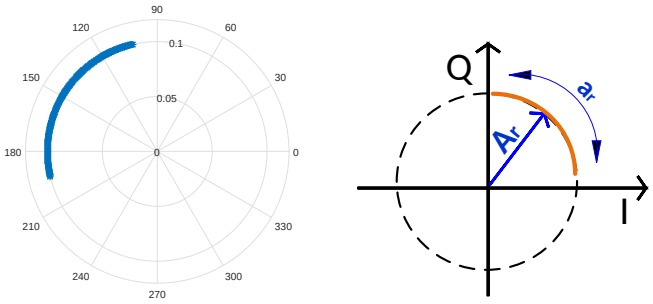

(a) (b)

Figure 3.5: Polar plot of the baseband signal.

of the carrier signal. From equations (3.7) and (3.6) it is possible to establish the necessary amplitude of target's motion to perform the full circle in the polar plot instead of an arc. If we replace the $d(t)$ term from the equation (3.7) by its expression (3.6), considering now the representation in discrete time domain, we obtain equation (3.16).

$$\begin{aligned} \varphi(n) &= \left[\left(\frac{4\pi d_o}{\lambda} + \Theta\right) + \frac{4\pi d(n)}{\lambda}\right] \\ &= \left[\left(\frac{4\pi d_o}{\lambda} + \Theta\right) + \frac{4\pi a_r}{\lambda}\cos(2\pi f_1 n)\right] \end{aligned} \tag{3.16}$$

Since the cosine function varies between $[-1, 1]$, neglecting stationary components of equation (3.7), the recovered phase has a range (3.17):

$$\varphi(n) \in \left[-\frac{4\pi a_r}{\lambda}, +\frac{4\pi a_r}{\lambda}\right] \tag{3.17}$$

To perform a full circle instead of an arc, the phase should reach 2π, to fully cover the interval $[-\pi, \pi]$. Hence, following relation verifies the necessary motion's amplitude in function of the wavelength λ that is necessary to perform the full circle instead of an arc:

$$\varphi(n) = \frac{4\pi a_r}{\lambda} \iff \pi = \frac{4\pi a_r}{\lambda} \iff a_r = \frac{\lambda}{4} \tag{3.18}$$

Thus, the target's motion should be less than $\lambda/4$ concerning the formed arc that should be obtained. As the total amount of movement increases or if the carrier frequency increases also the arc's length increases revealing that also the frequency selection is important for the system's performance. Figure 3.6 shows the visual difference when the amplitude achieves $\lambda/8$ (performing visually half wavelength motion in the polar circle) and $\lambda/32$ (performing visually $\lambda/8$ motion in the polar circle).

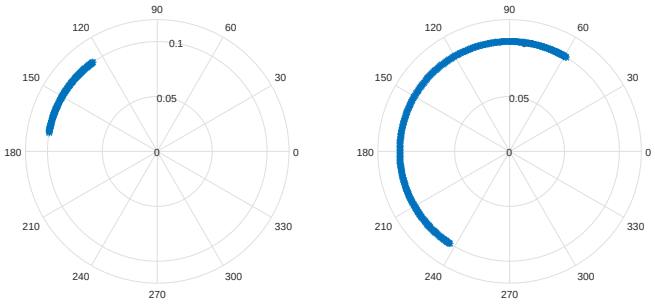

(a) (b)

Figure 3.6: Target's motion's amplitude influence in the full circle: (a) $a_r = 0.0016$ m for $\lambda/8$ (visually), (b) $a_r = 0.0064$ m for $\lambda/2$ (visually).

The amplitude A_r corresponds to the radius of the arc, so the received signal's energy is A_r^2. If the subject moves with a large deviation, the received energy changes and also the radius of the arc varies, but the centre remains located in its initial position. Assuming a case where the subject is constantly moving forward and backward, with a total deviation of 200 cm for instance, the signal's polar plot would present a spiral-like shape surrounding the same centre, instead a circle [17], [18]. Figure 3.7 shows the visual difference of this parameter.

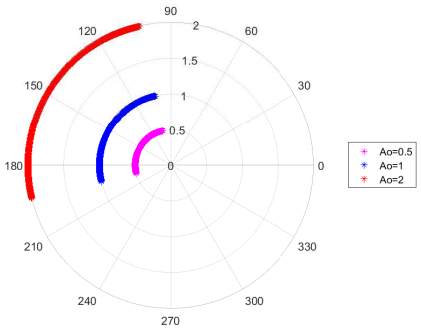

Figure 3.7: Influence of the received signal's amplitude A_r in the polar plot.

The nominal position of the target relative to the radar, d_o and the phase shift at the target's surface Θ, changes the position of the arc with respect to the full circle. This effect can be observed in Figure 3.8. This can represent a problem for the phase recover because, considering the phase in radians, if the arc varies around π, the receptor can not distinguish π and $-\pi$, hence wraps in the recovered signal occur. Some solutions for this problem will be presented later and also what happens to the recovered signal when this issue occur.

For last but not least, the carrier's wavelength is an important feature for the SNR.

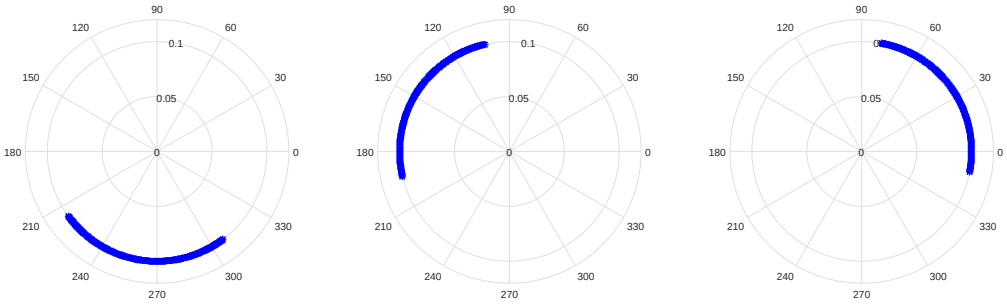

(a) (b) (c)

Figure 3.8: Influence of the target's nominal distance: (a) $d_o = 1$ m, (b) $d_o = 2$ m, (c) $d_o = 3$ m.

Regarding the wavelength's equation:

$$\lambda = \frac{c}{f_c} \tag{3.19}$$

where $c = 3 \times 10^8$ m/s is the speed of light in vacuum and f_c is the carrier frequency, the wavelength gets higher if f_c decreases causing lower SNR, [12]. On the other hand, the SNR increases for high values of f_c, whereas the wavelength decreases. It is beneficial to use as high frequency as possible, however it is necessary to find a balance because with a short wavelength, larger is the formed arc due to the phase modulation. With a larger arc length is easier to achieve π value or even a full 2π circle and hence wraps occur in the resulting signal after phase demodulation.

The impact of the wavelength is shown in Figure 3.9, where a comparison is made using the same target motion ($a_r = 0.00325$ m), with different carrier values, revealing differences in the arc length. The carrier values used in the simulation are 5.8 GHz, 2.5 GHz, and 10 GHz. From equation (3.18) a relation between the displacement in meters can be obtained and the resultant phase modulation in radians is made, for different carriers, according to the relation (3.20):

$$a_r = \frac{\lambda \varphi(n)}{4\pi} \tag{3.20}$$

Regarding the arcs plotted in Figure 3.9, it is possible to conclude that lower carrier frequencies are perceived as a smaller arcs in the polar plot (Figure 3.9b). In contrast, higher carrier frequencies contribute for a higher resolution, since the formed arc is bigger (Figure 3.9c). With higher resolution is possible to detect smaller motions, for instance the heartbeat motion in the subject's chest. The respiratory signal has bigger amplitude if compared with the heartbeat signal, hence lower carriers are sufficient.

3.2 Sources of Perturbation in Real Scenarios

In a real scenario there are other parameters that have huge impact in the correct demodulation, because they affect both I and Q channels. In this section the principal sources of disturbance will be described and their effect in the signal will be simulated. Finally, some solutions are presented and discussed.

The main sources of disturbance that we will consider are:

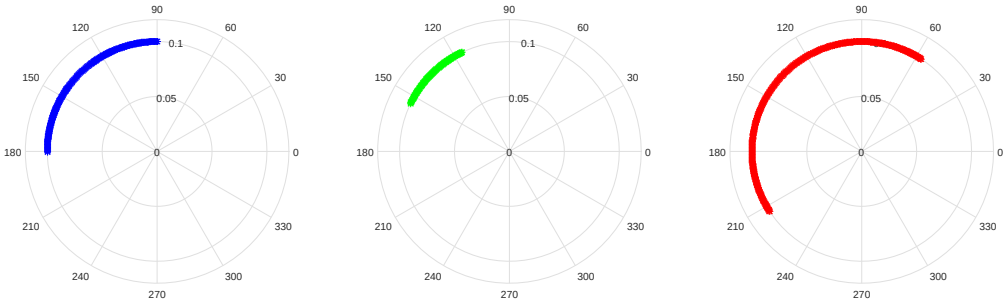

(a) (b) (c)

Figure 3.9: Influence of the carrier's wavelength, considering motion's amplitude $a_r = 0.00325$ m: (a) $f_c = 5.8$ GHz, (b) $f_c = 2.5$ GHz, (c) $f_c = 10$ GHz.

- Oscillator phase noise;
- IQ imbalance;
- DC offset due to clutter.

Each one of these sources of disturbance it is explained in the next points.

3.2.1 Oscillator Phase Noise

In CW radars, ideal oscillators provide perfect sinusoids. However in a real case scenario, oscillators have both amplitude and phase noise. Phase noise is generated due to random phase fluctuations in the oscillator [4]. These fluctuations can not guarantee frequency stability (i.e. the oscillators capability to produce the same frequency over time). Once all oscillators have an amplitude limitation, the amplitude noise can be neglected comparing with phase noise [4]. Hence, the transmitted and received signal defined previously by the equations (3.1) and (3.3) should be written as (3.21) and (3.22), respectively:

$$x(t) = \cos((\omega_0 + \omega_c)t + \phi(t)) \tag{3.21}$$

$$r(t) = A_r \cos[(\omega_0 + \omega_c)t + \varphi(t) + \phi(t - 2d_o/c)] \tag{3.22}$$

where $\phi(t)$ represents the phase noise and the term $\phi(t - 2d_o/c)$ has into account the time delay between the transmission and reception.

Phase noise is translated to noise in the baseband signal [4]: if the two signals in the LO for down-conversion are not correlated, a disruption in the desired baseband signal occurs, so the phase noise term may disrupt the accurate detection of motion $d(t)$. Although, if the same transmission source is used in the receptor's LO, the phase noise of both multiplying signals will be correlated, with a level of correlation dependent of the time delay between the two signals [11]. Adjusting in expression (3.11), the new quadrature terms in baseband will be (3.23):

$$\begin{aligned} g_I(n) &= A_r \cos\left(\theta_0 + \frac{4\pi d(n)}{\lambda} + \Delta\phi(n)\right) \\ g_Q(n) &= A_r \sin\left(\theta_0 + \frac{4\pi d(n)}{\lambda} + \Delta\phi(n)\right) \end{aligned} \tag{3.23}$$

where $\Delta\phi(n) = \phi(n) - \phi(n - 2d_o/c)$ is the residual phase noise in the baseband signal.

This time delay is proportional to the radar's range, therefore in cases of small radar range this delay is small, hence the noise spectrum in the baseband decreases and the phase noise can be cancelled out. This phase noise reducing effect is known as range correlation [11], and is present in homodyne receivers [4].

The transceiver used in this thesis has a homodyne architecture with an automatic DC rejection system. In order to guarantee the same frequency in both LO for transmitter and receiver and thus avoid the phase noise, the offset $f_o = 10$kHz is added in the generated signal $s(n)$, [2], [26], as mentioned in section 3.1. Since this effect is not verified, it was not necessary to simulate it and from now on, the term $\Delta\phi(n)$ is going to be neglected.

3.2.2 IQ Imbalance

The IQ imbalance behaviour is divided by phase imbalance that occurs when signal's I and Q are not exactly 90° out of phase, and gain imbalance which occurs when these signals do not have the same amplitude [3]. This issue will have impact in the phase demodulation by creating an undesired linear transformation on the I and Q signal, which affects the orthonormal properties important in quadrature systems. Thus, baseband signals will include both phase ψ_E and amplitude A_E error terms, where ψ_E is the difference between the phases of the two IQ signals minus 90, due to the quadrature, and A_E is the ratio between the amplitudes from I and Q signals. The quadrature components of the baseband signal are now defined as (3.24):

$$\begin{aligned} g_I(n) &= A_r \cos\left(\theta_0 + \frac{4\pi d(n)}{\lambda}\right) \\ g_Q(n) &= A_r A_E \sin\left(\theta_0 + \frac{4\pi d(n)}{\lambda} + \psi_E\right) \end{aligned} \tag{3.24}$$

Consequently, the extracted phase will have a phase error, that can be expressed as the equation (3.25), [3]:

$$\varphi_E(n) = \arctan\left(\frac{A_E \sin(p(n) + \psi_E)}{\cos(p(n))}\right) \tag{3.25}$$

where $p(n) = \theta_0 + \frac{4\pi d(n)}{\lambda}$ for a simpler notation [3].

Figure 3.10 shows the effect of IQ imbalance in the complex signal. For the purpose of this simulation, was considered that the target was at a nominal distance of $d_o = 0.5$ m and moved the equivalent of $\lambda/2$, in order to be easier to observe the effect of the imbalance. Resultant imbalance effect leads to an ellipse arc instead of a circle and rotate it.

Considering the ellipse function in equation (3.26), in order to guarantee a proper circle fitting the ellipse parameters a, b and c should satisfy the condition (3.27), otherwise an ellipse will be drawn. When imbalance is present, equation parameters verify the condition (3.28), instead.

$$ax^2 + bxy + cy^2 + dx + ey = f \tag{3.26}$$

$$\begin{cases} a = c \\ b = 0 \end{cases} \tag{3.27}$$

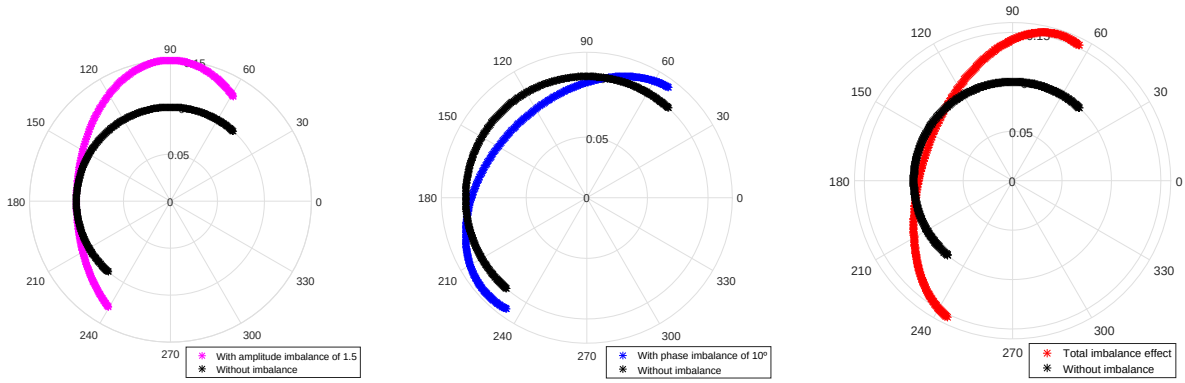

(a) (b) (c)

Figure 3.10: Simulated polar plot for IQ imbalance effect: (a) The effect of amplitude imbalance, (b) The effect of phase imbalance, (c) The effect of both amplitude and phase imbalance.

$$\begin{cases} a \neq c \\ b \neq 0 \end{cases} \tag{3.28}$$

More specifically, the gain imbalance observed in Figure 3.10a will cause $a > c$, and the phase imbalance causes a tilted ellipse due to $b \neq 0$, as shown in Figure 3.10b.

If the imbalance values are known by their measure, it is possible to correct the IQ imbalance by using the Gram-Schmidt method, applied to the quadrature components of the baseband signal, which makes these two vectors orthonormal as detailed in equation (3.29), [3]. This method does not work for wide band systems because phase imbalance varies with frequency, although bio-signals have narrowband features and thus it is possible to implement this method in this system.

$$\begin{bmatrix} g_{I,O}(n) \\ g_{Q,O}(n) \end{bmatrix} = \begin{bmatrix} 1 & 0 \\ -\tan(\psi_E) & \frac{1}{A_e \cos(\psi_E)} \end{bmatrix} \begin{bmatrix} g_I(n) \\ g_Q(n) \end{bmatrix} \tag{3.29}$$

Applying (3.29) with the baseband signals expressed in equations (3.24), the resulting polar plot will have an arc fitted in a circle instead of an ellipse.

3.2.3 DC Offset

In a wireless channel, we are ahead of a free-space propagation scenario when there is a single and direct signal path between the transmitter and the receiver. Nonetheless, when leading with real case scenarios, the surrounding environment has to be considered, since effects such as reflections, refractions, diffractions and scattering occur and cause many signal replicas which will sum to the received signal. These superimposed replicas from the transmitted signal, also known as **multipath**, can severely degrade the direct-path signal once are characterized by their amplitude, phase shift and delay and can contribute constructively or destructively, [27]. The reflecting obstacles are located at different distances relative to the receptor and in the context of our application include also the reflections from stationary

parts of the body, as represented in Figure 3.11a. Thus, the multipath causes phase and amplitude variations that depends in the different path lengths.

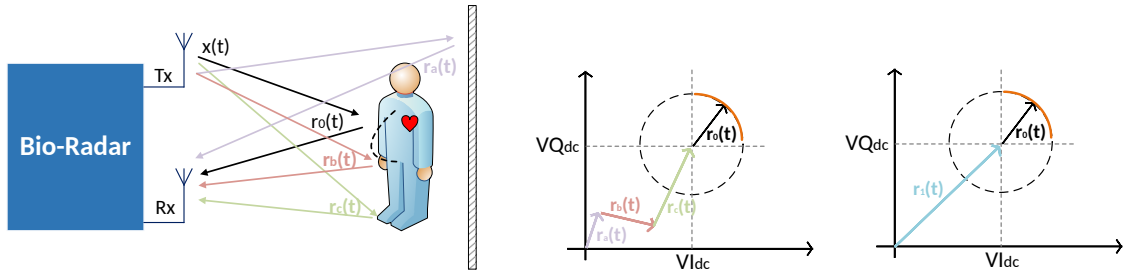

(a) (b)

Figure 3.11: Effect of the parasitic reflections: (a) Representation of the parasitic reflections in a real scenario, (b) Vectorial representation of the received signal including all the involved parasitic components.

Assuming that all clutter sources are stationary, these reflections are not time varying and hence are perceived as DC offsets. The received signal will be a sum of all signals that propagate using the same carrier, as defined previously with equation (3.3). This effect is perceived in both real (VI_{DC}) and imaginary (VQ_{DC}) parts, which leads to an offset in the arc's centre, as shown in Figure 3.11b. In this figure, the vector $r_1(t)$ represents the sum of all received replicas $r_a(t)$, $r_b(t)$, $r_c(t)$.

The DC component is a major source of perturbation to the signal. Although, the DC signal has also DC information related to the subject's initial position d_o. Despite its stationary value sensed as a DC component, it determines the position of the formed arc in the circle. Therefore this value consists in an important requirement for an accurate demodulation and should not be removed [17].

The received signal $r(t)$ and the baseband signal $g(n)$ are now defined with equations (3.30) and (3.31), respectively.

$$r(t) = A_0 \cos\Big((\omega_0 + \omega_c)t + \varphi(t)\Big) + A_1 \cos((\omega_0 + \omega_c)t + \theta_1) \tag{3.30}$$

$$\begin{aligned} g(n) &= A_r e^{-j\varphi(n)} + A_1 e^{j\theta_1} \\ \theta_1 &= d_1 4\pi/\lambda \end{aligned} \tag{3.31}$$

where A_1 is the amplitude from the clutter signals and d_1 the nominal distance between the radar and the clutter sources. Regarding expression (3.31), the updated version of quadrature baseband signals defined in (3.11) includes now the DC offsets and is represented by the equation (3.32):

$$\begin{aligned} g_I(n) &= A_r \cos\left(\theta_0 + \frac{4\pi d(n)}{\lambda}\right) + VI_{DC} \\ g_Q(n) &= A_r \sin\left(\theta_0 + \frac{4\pi d(n)}{\lambda}\right) + VQ_{DC} \end{aligned} \tag{3.32}$$

where VI_{DC} and VQ_{DC} are the I and Q components of the representative clutter baseband signal $r_1(t)$, or in other words, the DC offsets of each channel. They act as linear

transformations in each component, so the expression of the AT should be written as equation (3.33), [17]:

$$\begin{aligned} y(n) &= \angle g(n) = \angle(g_I(n) + jg_Q(n)) \\ &= \angle\Big[\Big(A_r \cos\Big(\theta_0 + \frac{4\pi d(n)}{\lambda}\Big) + VI_{DC}\Big) + j\Big(A_r \sin\Big(\theta_0 + \frac{4\pi d(n)}{\lambda}\Big) + VQ_{DC}\Big)\Big] \end{aligned} \tag{3.33}$$

In order to simulate the impact of this disturbance, a new signal was generated according to equation (3.31), with the equivalent target's motion of $\lambda/2$ ($a_r = 0.0064$ m) and considering that the principal target is at a distance of $d_o = 1.5$ m. In this simulation, the parameter d_1 will be changed since it is the one that causes more influence − it can change the position of the arc to any part of the complex plan as shown Figure 3.12. Its random position can cause wraps in the recovered signal if it is positioned near π. The amplitude A_1 only changes the position of the arc in the real axis, so its effect is not perceived in the polar plot.

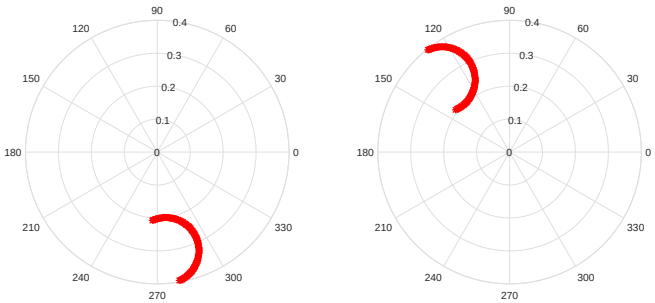

(a) (b)

Figure 3.12: Impact of clutter nominal distance in signal considering that the amplitude of the clutter signal is $A_1 = 0.3$: (a) Distance $d_1 = 1.7$ m, (b) Distance $d_1 = 2$ m.

The offsets of the arc centre caused by the linear transformation in baseband signals (3.32), affects severely the arctangent performance. For this reason the DC offset's must be removed before demodulation without compromising system's efficiency. The impact of DC offsets will be simulated later in this chapter, in section 3.3, where a simulation of the signal extraction result is done regarding ideal and non-ideal scenarios.

3.2.4 Total Perturbation Effect

Considering all the disturbances presented so far, beside the phase noise which have been neglected, the baseband quadrature signals previously defined in equation (3.32) are now defined as the equation (3.34) [12]:

$$\begin{aligned} g_I(n) &= A_r \cos\Big(\theta_0 + \frac{4\pi d(n)}{\lambda}\Big) + VI_{DC} \\ g_Q(n) &= A_E A_r \sin\Big(\theta_0 + \frac{4\pi d(n)}{\lambda} + \phi_E\Big) + VQ_{DC} \end{aligned} \tag{3.34}$$

Figure 3.13 presents a simulation of the signal in the receptor with these disturbances, considering the same imbalance values used in the simulation of Figure 3.10c.

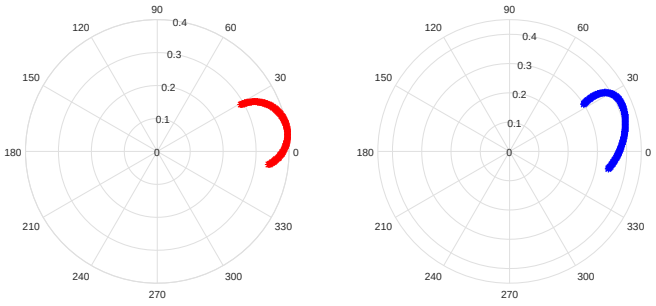

(a) (b)

Figure 3.13: Simulated polar plot with presence of DC offsets considering that the clutter is located at a distance of d_1=1.5 m from the radar, and amplitude $A_1 = 0.3$: (a) Without any IQ imbalance, (b) With IQ imbalance.

3.2.5 Methods for DC Offset Cancellation

Now will present a brief overview of different methods applied for DC offsets compensation is presented, leading to the one that best fits in the necessary requirements to guarantee the algorithm accuracy, by preserving the DC information beyond the DC offset elimination.

AC Coupling

A straightforward solution for DC offsets cancellation is using AC coupling, more specifically applying a high-pass filter, but it would also remove the DC information respecting to target's position, that is in this case important for the phase demodulation method, [13], resulting in signal distortion, affecting also the system time response. An example of the new shape of respiratory signal, after AC coupling is shown in Figure 3.14. The system time response is affected due to the filter's settling time. The amount of delay can not follow the received signal changes over time, because they are too fast.

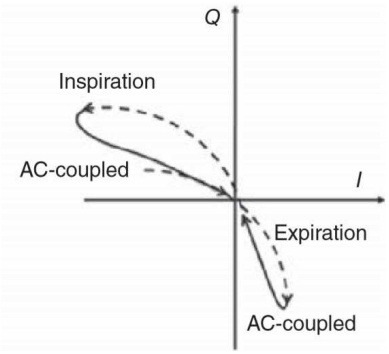

Figure 3.14: AC Coupling effect, [11].

DC offset Calibration with Previous Measurement

In [13] two main sources of prejudicial DC signal are established: clutter generated by reflections from stationary objects in the surrounding environment and static body parts, and hardware imperfections that encompass circulator imperfect isolation, antenna mismatch and mixer LO to RF port imperfect isolation, for instance. The latter causes self-mixing which generates DC output.

In the work developed in [13], DC offset caused by hardware imperfections is measured in practice, as well as the DC offset due to reflections, by finding maximum and minimum DC values using perfect reflectors. The method used in this work to perform DC offsets compensation is the subtraction of measured DC values mentioned above, in the output signal. Although, the DC information that needs to be maintained in the signal, regarding the nominal position of the target, has higher amplitude than the bio-signals, revealing impossible to digitize them because it cause the amplifier and ADC saturation. Thus, a new method was implemented with the set-up shown in Figure 3.15. Both types of induced DC offsets were measured with no objects in front of the radar within 1 m.

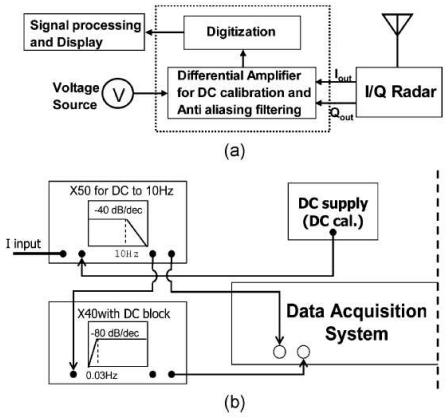

Figure 3.15: Measurement set-up for DC compensation from [13].

Afterwards, the same voltage value measured as DC offsets were generated by DC supply, removing the DC level in the output using differential amplifiers. After this calibration, a subject is located in front of the radar at a nominal distance of 1 m and its bio-signals are measured. In this way, the clutter signals effect is reject, preserving the DC information required for proper phase demodulation. However, this technique does not take into account the clutter from stationary parts of de body, revealing not robust enough. Other disadvantage of this method is the requirement of previous calibration of the DC offsets before the real monitoring starts, which reveals a barrier in its efficiency.

Methods Based on Centre Tracking

With the method purposed by [17], called as "Centre Tracking Compensation Method", it is possible to cancel DC offsets and estimate DC information simultaneously, by restoring it directly from the association of quadrature outputs. This technique minimizes the time delay and distortion when comparing with high-pass filter methods. With this technique the centre of the circle where the arc fits can be estimated from the first seconds of data [12].

The centre of the arc should be centred in zero, however due to DC offsets presence is centred in the coordinates VI_{DC} and VQ_{DC}. This method tracks the circle centre back to zero again, subtracting the coordinate values. With arc's centre back to zero again, the phase information due to the target's motion can be extracted properly. In [17] the data is collected, saved and only treated afterwards. The digital signal treatment is performed in MATLAB, using the recorded data. For centre estimation the first samples of data (the necessary amount to obtain one cycle of respiration) are used, in order to have the complete arc length. The estimated value of centre's coordinates is then removed in both I channel and Q channel using differential amplification, to track the arc back to origin.

In this paper, [17], is also proved that is possible to recover phase modulated information whether if the target motion is smaller or larger than the wavelength of the carrier, by executing this experiment with a subject that is moving towards and backwards the radar with a total displacement of 200 cm (the wavelength is relative to a carrier of 2.4 GHz).

There are several methods for centre estimation that can be performed in real time, i.e. without a previous calibration. Two methods are going to be explored:

1. Park method, [18];
2. Least squares fitting using Levenberg-Marquardt (LM) algorithm, [12], [28].

Park Method

The method presented in [18] consists in a DC cancellation method that constitute a primary step in centre tracking compensation procedure. It minimizes also the time delay and distortion that would occur if high-pass filter was used instead. This method can be applied in real-time system, once does not need any previous calibration before the measuring action starts, being now a part of DSP algorithm for signal treatment. The Park algorithm starts

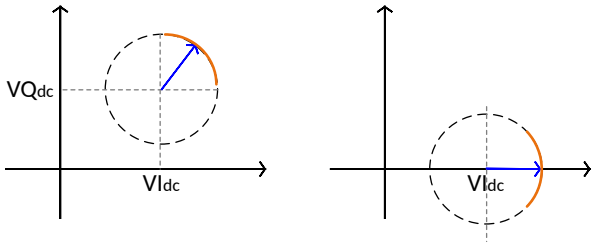

Figure 3.16: Arc rotation, [4].

by the rotation of the arc in order to be orthogonal with Q axis, as represented in Figure 3.16. This can be achieved by computing the matrix of eigenvectors of the covariance matrix and multiplying its transposed matrix by the data. Thus, there is only a real offset given by VI_{DC}. This single offset value can be obtain from a heuristic estimator (expression (3.35)), that finds k from $VI_{DC} = (k, 0)$ [12]:

$$\hat{k}(i,j) = \frac{\left|\begin{matrix} B_I[i] \\ B_Q[i] \end{matrix}\right|^2 - \left|\begin{matrix} B_I[j] \\ B_Q[j] \end{matrix}\right|^2}{2(B_I[i] - B_Q[j])}$$
$$\hat{k} = \underset{i \neq j}{\text{median}}[\hat{k}(i,j)] \tag{3.35}$$

In this case Q channel is in an optimum point and I in a null point. If the arc length is small enough to assume the small angle approximation (i.e. $d(t) \ll \lambda$), linear demodulation can be performed by considering only Q-channel as the demodulated signal, once is placed in an optimum position. In this way the same channel is used rather then quadrature combination like the AT. Otherwise, the coordinates of displaced circle centre are estimated by multiplying the result of (3.35) by the inverse matrix of eigenvectors, [12].

Least Squares Based Methods

LM method, also called as the Gauss-Newton method with the LM correction, consists in the successive application of the Least-Square Fitting method (LSF) until the resultant error is reduced to an acceptable level, [28]. It presents beneficial characteristics such as high precision and computationally less complex, which remains constant with increasing data size rather than other methods with higher computation complexity for large data segments.

The LSF method is a simple algorithm for fitting parameters calculation where its cost function should be minimized. In other words, it finds the minimum distance from the estimated circle to the data points [12], [28]. This method is susceptible to a measurement error and dependent of the SNR in the baseband signal and hence in case of noisy data it is difficult to find a close-form result to achieve an accurate circle fit leading to a wrong estimation of DC offsets [29], [28]. Therefore the LM method takes advantage of the LSF method, by finding the F function that minimizes the distance between data points and the fitting circle, iteratively. The minimum of F corresponds to the desired centre estimation.

One disadvantage of this method is the loss of accuracy when small displacement is measured concerning to the carrier wavelength. To overcome this impairment a novel arc shift method was proposed in [29] where can perform good circle fitting even with low SNR conditions.

Tests were performed in [12] in order to compare the efficiency of these algorithms (Park method and LM method). They concluded that LM method is the one that returns good estimation of circle fitting whether the data is uniformly distributed in the formed arc or not. Moreover, Park method fails when data is not well distributed, by being accumulated in some part of the arc, for instance.

Implemented Method Selection

The selected method is an estimation of the arc centre, using for this purpose a circle fitting method [12], [30]. In order to accomplish the circle fitting, an *Ellipse Fitting Function* based in the LSF was implemented in MATLAB. This function finds the best fit to an ellipse for a given set of points [31]. Thus it receives as input the real and imaginary part from the complex baseband signal (3.34) and in its output returns a parameter structure where the centre coordinates of the fitted ellipse are given. Using an *Ellipse Fitting Function* for this matter is a valid solution because if the ellipse parameters from equation (3.26) obey the condition (3.27), it means that a perfect circle is obtained.

In addition, the same function was also used to check the imbalance effect in each sample of recorded data and its final result after the Gram-Schmidt method application.

Once the coordinates from the geometric arc centre are determined, they are subtracted from each I and Q parts of the complex signal, forcing the arc to be centred in zero.

3.3 Respiration Signal Recovery

As mentioned previously in the beginning of this chapter, the received signal is phase modulated by the chest-wall motion of the subject. Thus, phase information gives us the desired respiratory signal and once extracted it is possible to estimate its rate. In this section, two different approaches for phase demodulation are presented, regarding the receiver's architecture. Also solutions for the wrap problem, discussed in section 3.1.1, are given.

3.3.1 Phase Demodulation

In [17] and [18] experiments were executed in order to compare two demodulation types: linear and non-linear. Both presented different behaviours according to the arc's length.

Linear demodulation was introduced by [18] with the Park Method for DC offset cancellation. To perform this method, the small angle approximation have to be verified ($d(t) \ll \lambda$) in order to be possible to assume that the formed arc is modelled as a straight line, with small error. Thus it should be applied in cases of low frequency carriers, [4]. To execute this method only one channel is considered as demodulated signal. However, the resultant signal is sensitive to null detection points problem. To overcome this issue a quadrature Doppler radar receiver with channel selection is a possible solution, as mentioned previously in section 2.3.2.

Non-linear demodulation can be achieved by combining both quadrature outputs simultaneously as result of the arctangent computation. Thus, phase information is linearly proportional to the chest-wall motion. Its orthonormal characteristics ensure that if the I channel is in a "null" point, the Q channel is in a "optimum" position or vice-versa. In [13] was proved that AT, with quadrature channels combination, is an accurate method of bio-signal extraction, irrespective the target's position and without a channel selection.

The conducted experiment in [13] comprise two different patterns of respiration, where one is more shallow than the other, creating different arc lengths. For the lower length case, linear and non-linear presented slightly difference in the measured error. On the other hand, for a normal respiratory pattern and hence bigger arc length, non-linear method presented the smallest error, revealing the best option. In [17] the same experiment was repeated with the subject positioned in different distances relative to the radar, revealing that AT presents higher accuracy and lower number beat error comparing with linear demodulation method.

Since the subject can randomly move during the monitoring process and a carrier of 5.8 GHz is going to be used in the prototype developed in this dissertation, the non-linear method is the most suitable for our application. In our case, the AT is implemented via four quadrant inverse tangent, instead of the regular arctangent function. It means that the obtained signal is in the range $[-\pi, \pi]$. This can be performed with the MATLAB function ***atan2(Y,X)***, where $\boldsymbol{Y}$ and $\boldsymbol{X}$ is the input signal's imaginary and real part, respectively. Other way to execute this demodulation is with the computation of the complex signal's angle, using the *Angle* function of MATLAB.

3.3.2 Phase Wrap Occurrence

The only influence of the subject's position in the AT demodulation performance is the possibility of wrapping to occur, since it changes the arc location in the complex plot. If the target's position is such that the signal's phase crosses the π value, wrapping will occur.

Figure 3.17 shows the recovered signal with and without wraps, as the result of the conducted MATLAB simulation. For the simulation shown in 3.17a, the choose nominal distance d_o locates the arc between 2^{nd} and 3^{rd} quadrants. This simulation and its results are detailed in section 3.5. In order to compensate this signal disruption two different approaches could

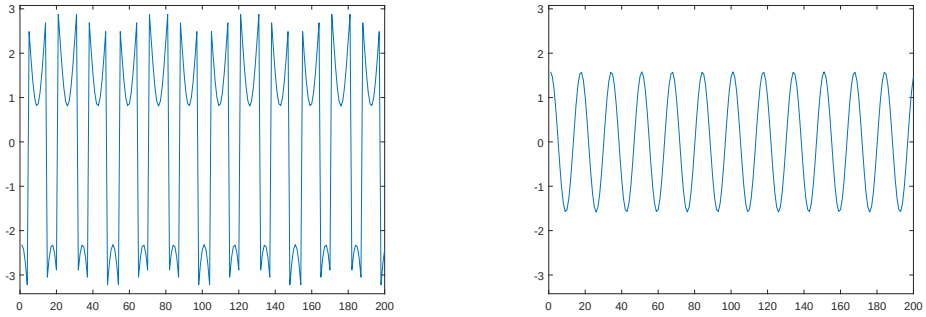

(a) (b)

Figure 3.17: Respiratory signal after phase demodulation.

be implemented: an unwrapping algorithm or a forced arc rotation.

Unwrapping Algorithm

It is possible to recover the original signal without damaging its rate by performing an unwrap algorithm that reconstructs the signal everytime a drop-out occurs. The unwrap algorithm, represented in Figure 3.18a stands as follows [32]: after the phase extraction, each sample is compared with the prior one. If their difference is larger than π all the samples starting in the one that is being evaluated, are subtracted by 2π. If their difference is less than $-\pi$, the same approach is done but summing 2π, instead of subtracting. The same procedure is done until it reaches the last sample.

Once the recorded signals are relative to patients that can move or have a non uniform respiration pattern, the presented data is not uniformly distributed over the arc, presenting limitations in the performance of this method.

Signal's Rotation Algorithm

Another option to solve the wraps issue is to rotate the complex signal the sufficient value of phase in radians so the arc does not reach π. For this purpose a *phase sensing algorithm* (Figure 3.18b) is required after IQ imbalance compensation and the DC offsets removal, in order to detect signal's phase orientation. Case it reaches π, signal is multiplied by an exponential with $\pi/2$ as phase value (expression (3.36)).

$$b_{change} = e^{-j\pi/2} * b(n) = e^{-j\pi/2}(A_r e^{j\varphi(n)}) \tag{3.36}$$

where $b(n)$ is the signal in the output of the *DC Removal* block from Figure 3.2.

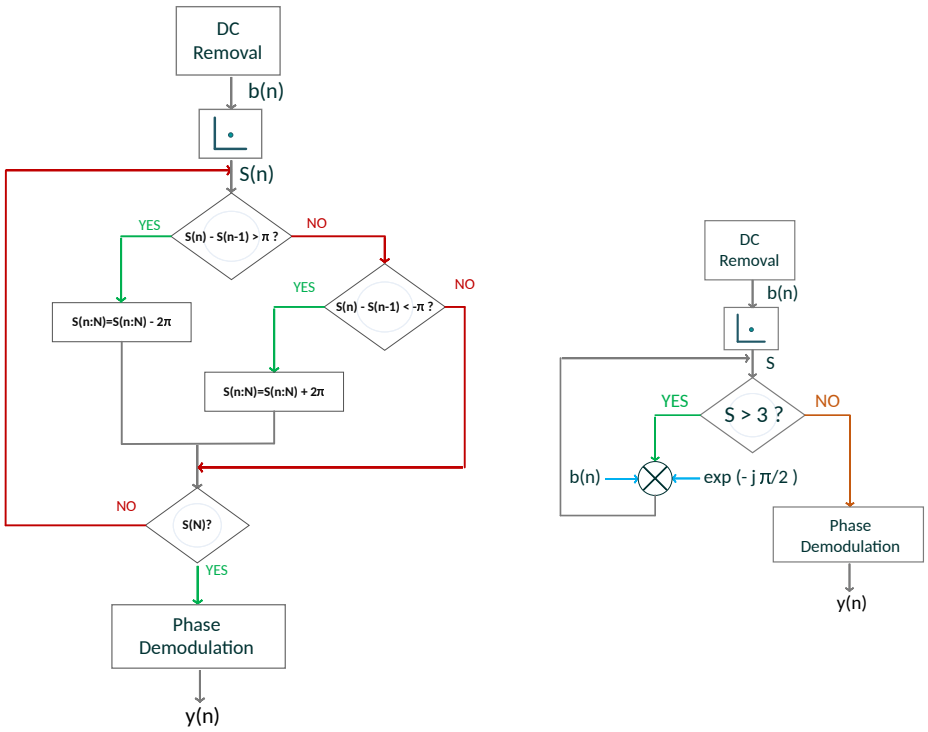

Figure 3.18: (a) Unwrapping algorithm, (b) Arc rotation algorithm.

3.4 Respiratory Rate Estimation

There are several estimation methods for determining the bio-signals rate. In this section, some methods are presented and compared, in order to select the one that best fits the current system requirements, focusing in a real-time application.

3.4.1 Peak Time Detection

This method is introduced in [4] and is more adapted to the heartbeat signal, due to its sharp shape. Each peak is detected and the time elapsed between consecutive peaks is estimated. The heartbeat rate is evaluated on this estimation. Nonetheless, this method works better for high SNR, because is sensitive to background noise. As result, the exact position of peaks can be biased, increasing the error of the estimation. Whereas this technique is not appropriated for different signal shapes and should be applied in a noiseless environment, it is not the best choice for our case.

3.4.2 Crossing Mean Value Algorithm

A straightforward method to compute the respiratory signal's rate in a real-time system, would be counting the number of mean value crosses, regarding the upward curve. Figure 3.19, shows an algorithm proposal to conceive this method. After phase demodulation, signal $y(n)$ represents the respiratory signal and its samples are used to evaluate the respiratory rate. The first seconds of data allow the mean phase computation which serves as a reference value

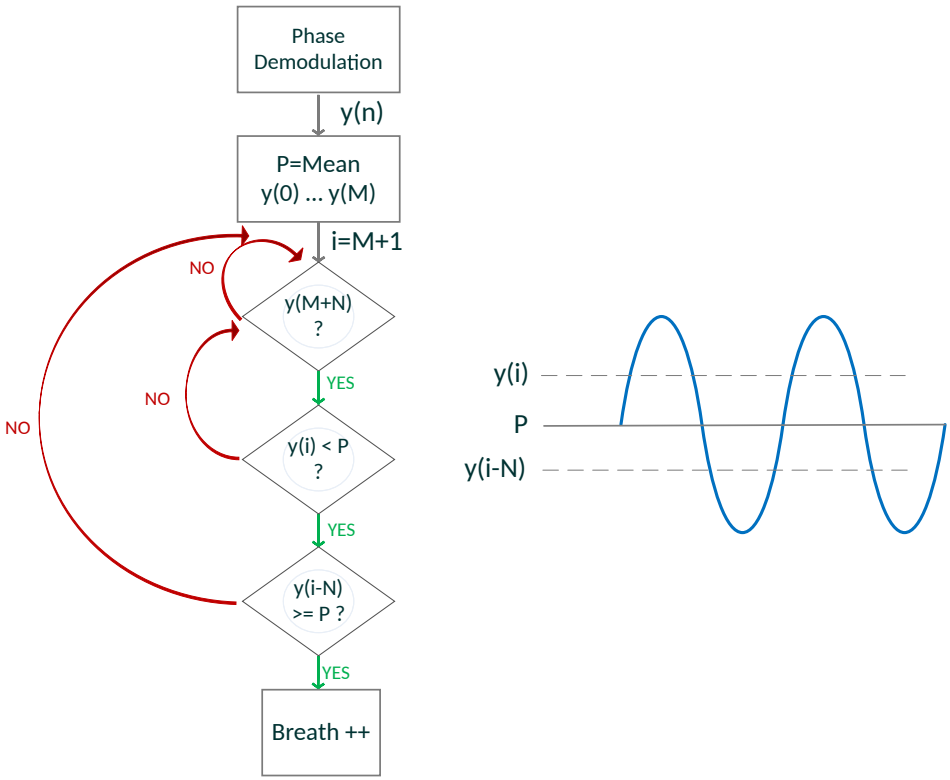

Figure 3.19: Crossing mean value flowchart.

(from now on called P) for comparison purposes. Having in mind that the breathing pattern is not always constant, i.e. the amplitude of each breath can be different, the measurement is made using two distant samples: one should be above P value and the other below, ensuring that the mean value belongs in this interval. Starting from $y(M+N)$, where $y(M)$ represents the last sample that was considered for the mean value computation and N represents the length of considered interval, a pair of samples ($y(i)$ and $y(i-N)$) is evaluated. If $y(i) > P$ and $y(i-N) \geq P$ one respiration is counted. This procedure is repeated for every sample multiple of N.

Then, considering at least 25 seconds, a estimation can be performed regarding the number of respirations counted in this time period and a direct relation of the number of breaths in one minute can be made.

However, this method is not robust, because in real-time monitoring system the mean value will change due to the random subject's motion and a periodic update could not be sufficient.

3.4.3 Autocorrelation Algorithm

This method finds repeating patterns in signals with a certain periodicity. For this purpose the cross-correlation of the signal with it own delayed version is computed. Autocorrelation presents an advantage, when random noise is present in signal due to moving body parts beside the subject's chest-wall, [25]. Regarding the recovered phase signal from the demodulation in time domain $y(t)$, the autocorrelation function estimates similarities in the time-varying

signal by computing the correlation with itself delayed, where the time lag is defined as τ. This function in time domain is defined as equation (3.37):

$$R_{xx}(\tau) = y(t) \otimes y(t+\tau) = \int_{-\infty}^{\infty} y^*(t)y(t+\tau)dt \tag{3.37}$$

Moreover, autocorrelation function in discrete time domain is defined as equation (3.38):

$$R_{xx}(\tau) = \frac{1}{N}\sum_{n=0}^{N-1} y^*(n)y(n+\tau) \tag{3.38}$$

In [4] a window is used to eliminate leakage from the less correlated data. The window application is expressed in equation (3.39):

$$R_{xx}(\tau) = \frac{1}{N}\sum_{n=0}^{N-1} y^*(n)w(n) * y(n+\tau)w(n+\tau) \tag{3.39}$$

where N is the data set length, and $w(n)$ is the window function. Figure 3.20 represents the simulation of the autocorrelation result of the extracted signal, where the highest peak represents the moment where the signal is totally correlated, or in other words, when equal signals are superposed in the same instant. Periodic signals maintain the same pattern over the

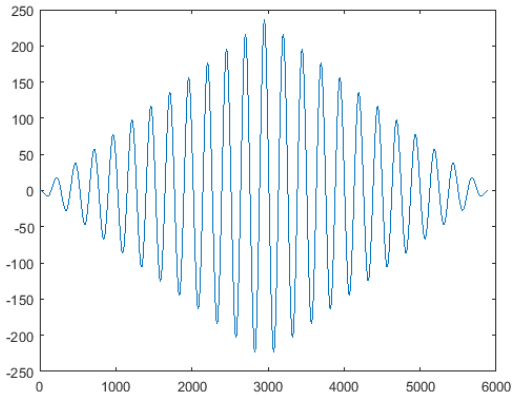

Figure 3.20: Plot of the extracted signal's autocorrelation result.

time, therefore the second highest peak appear when this repetition is recognized. Therefore, the passed time between the instant zero (highest peak) and when there is a pattern repetition (second highest peak) is measured. The time measurement is the equivalent number of passed samples in the discrete time domain. To pass from discrete time domain to time domain, the number of samples between two peaks is divided by the sampling rate. The rate in Hz can be obtained by the relation:

$$RespiratoryR[Hz] = \frac{60}{N_\tau} \tag{3.40}$$

where N_τ is the number of samples measured between two peaks and divided by the sample rate.

In [25] was concluded that the autocorrelation method is suitable for estimation in short period of measurement time and is accurate in the presence of random noise, because does not take it into account in the periodicity measure.

3.4.4 Power Spectral Density Estimation

The PSD is seen as the Fourier transform of the autocorrelation function $R_{xx}(\tau)$ from equation 3.37, [33], and it can be described by the equation (3.41).

$$S_x(f) = \int_{-\infty}^{\infty} R_{xx}(\tau) e^{-j2\pi f\tau} d\tau \tag{3.41}$$

This technique divides data in subsets by applying windows with appropriate length (each window should contain a significant number of periods of signal) and compute the Fast Fourier Transform (FFT) of each fragment. Finally an average of the resultant FFT window is made and the PSD of all data is achieved in order to obtain the bigger frequency component and therefore the desired rate result. Methods based on windowing are usually more accurate and contribute to a better SNR. However, they can not keep quick changes in signal because they are based on window averages. If during the windowing period there is a quick rate change that should be detected as an anomaly, it does not affect the final rate estimation, leading to bad diagnosis.

Different window-based methods for PSD estimation are now described.

Welch Method

This method divides the dataset in multiple and partially overlapped segments and computes the periodogram of each segment. The final spectral density of the input signal is the average of the total periodogram previously computed.

Considering that the input dataset is the respiratory signal in discrete time domain $y(n)$, extracted from phase demodulation using AT, the Welch method is represented by Figure 3.21. Its mathematical model stands as follows, [34]:

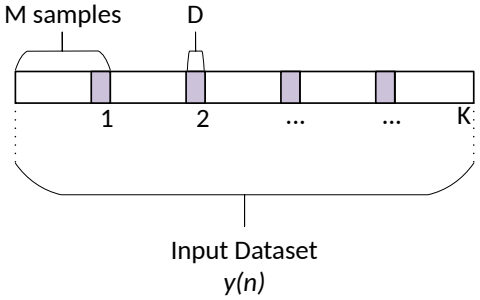

Figure 3.21: Dataset division for Welch method implementation.

The dataset is divided in K segments, with length of M samples. Therefore the segment i is defined as:

$$y_i(n) = y(n + iM) \tag{3.42}$$

where $i = (0, 1, 2, ..., K-1)$ and $n = (0, 1, 2, ..., M-1)$. The periodogram of each segment i is given by the equation (3.43)

$$P_{yy}^{(i)}(f) = \frac{1}{M} \left| \sum_{n=0}^{M-1} y_i(n) e^{-j2\pi fn} \right|^2 \tag{3.43}$$

As mentioned before, the segments are overlapped, so lets define that the i^{th} subset starts in sample iD, thus the dataset separation from (3.42) should be defined as (3.44):

$$y_i(n) = y(n + iD) \tag{3.44}$$

where D is defined as the overlap percentage. In other words, if $D = M$ there is no overlap whereas if $D = M/2$ there is an overlap of 50%. This overlap in the periodogram computation could cause information redundancy, which can be avoided if windows are used before the periodogram computation. Windows will discard samples that are not included in the window area, reducing also the spectral leakage caused by lateral multiplication. The sidelobe data attenuation depends on the window function choice. Regarding equation (3.43), periodogram of the windowed data subset is now defined as equation (3.45):

$$P_{yy}^{(i)}(f) = \frac{1}{MU}\left|\sum_{n=0}^{M-1} y_i(n)w(n)e^{-j2\pi fn}\right|^2 \tag{3.45}$$

where U is the normalization factor for the window power, expressed as equation (3.46):

$$U = \frac{1}{M}\sum_{n=0}^{M-1} w^2(n) \tag{3.46}$$

Finally, the desired power estimation is obtained by the averaging of the total computed periodograms $P_{yy}^{(i)}(f)$. This sum is represented by (3.47).

$$P_{yy}(f) = \frac{1}{K}\sum_{i=0}^{K-1} P_{yy}^{(i)}(f) \tag{3.47}$$

In MATLAB the function used to execute this method is:
pwelch(X, WINDOW, NOVERLAP, NFFT, Fs)

- ***X*** is the dataset input for spectral estimation;
- ***WINDOW*** is the window length specification i.e. each subset length specification. For default this function uses Hamming window;
- ***NOVERLAP*** is the number of overlapped samples. For default, 50% overlap is established.
- ***NFFT*** is the number of samples used for FFT computation. This number should be a 2 base exponential.
- ***Fs*** is the sampling frequency specification.

A good feature of this method is the approximately constant variance value, once the power estimation is performed using average values. Therefore, this method was selected to be implemented in the real-time bio-radar prototype. The dataset, as well as subset length, have to be large, in order to guarantee good resolution.

MUSIC Algorithm

This method computes the pseudo spectrum of the input signal, by its decomposition in eigenvectors from the correlation matrix of the signal. It is assumed that the input signal $y(n)$ compounds p complex exponentials with white Gaussian noise, [34].

Upon the eigenvectors of the correlation matrix computation, they are laid out in decreasing order. The p values with bigger eigenvalues form the eigenvector subspace with higher spectral component. The remaining eigenvectors correspond to the noise subspace.

The frequency estimation can be obtained from equation (3.48):

$$P_{MUSIC}(e^{j\omega}) = \frac{1}{\sum_{k=p+1}^{M} \left| s^H v_k \right|^2} \tag{3.48}$$

where v_k represents the eigenvectors from noise subspace and s^H the transposed complex conjugate of the complex sinusoid vector s from equation (3.49)

$$s = [1 \quad e^{j\omega} \quad e^{j2\omega} \quad ... \quad e^{j\omega(M-1)}] \tag{3.49}$$

The localization of the largest peaks p corresponds to the spectral estimation of the input signal $y(n)$. This estimation method does not require huge dataset, so it can be perform using few samples.

In MATLAB the function used to execute this method is:
pmusic(X,P,NFFT,Fs)

- ***X*** is the input signal for spectral estimation calculation;
- ***P*** is the number of complex sinusoids in the signal
- ***NFFT*** is the FFT length
- ***Fs*** is the sampling frequency used.

3.5 Final Algorithm Selection

So far we have described the basic mathematical model of the system, introducing sources of disturbance for the signal and simulated the DSP algorithm performance having in consideration the real scenario influence. It is now possible to conclude that interferences such as clutter and hardware issues can affect the received signal and phase demodulation significantly. Therefore, in this section a simulation will be performed taking into account the DC offset and IQ imbalance presence, with a view to perform the phase demodulation in this conditions and evaluate the performance of the DSP algorithm selected over the last sections. The algorithm is summarized in Figure 3.22.

Table 3.1 and 3.2 sum up the signal's parameters used for the following MATLAB simulation, regarding the received signal (3.30) and the baseband signal (3.34)

To do the phase demodulation the *Angle* computation is the selected option. Table 3.3, describes two different simulation scenarios of phase demodulation: when the distance d_o induce wraps and when it does not. Regarding the algorithm present in Figure 3.22, the procedure to recover the respiratory signal stands as follows:

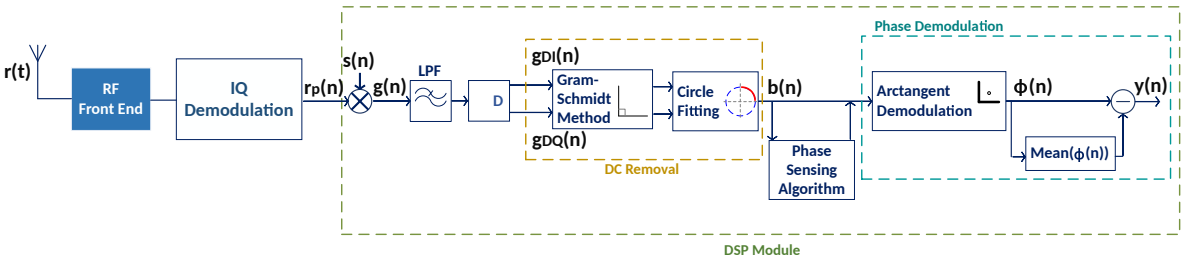

Figure 3.22: DSP algorithm block diagram.

Received Signal - $r(t)$				
F_s [Hz]	f_c [Hz]	λ [m]	A_0	Downsampling D
100	5.8G	0.0517	0.1	10

Table 3.1: Simulation signal's parameters - Received signal neglecting any kind of disturbances.

Varying phase - $\varphi(t)$			
f_1 [Hz]	a_r [m]	d_o [m]	Θ [rad]
0.3	0.0057	1.5	$\pi/12$

Table 3.2: Simulation signal's parameters - Respiratory signal definition.

Test number	Clutter's amplitude - A_1	Clutter's distance - d_1 [m]	Target's distance d_o [m]
Test 1 - Without wrap	0.3	1.7	1.5
Test 2 - With wrap	0.3	1.9	2

Table 3.3: Simulation signal's parameters - DC offset and IQ imbalance definition.

---

1. Downsampling the baseband signal. Since the sampling frequency selected for this simulation is $F_s = 100$ Hz, and the simulated respiratory signal has low frequency component (f_1=0.3 Hz), the new sampling frequency should also be low, therefore the decimation factor selected is $D = 10$ and the new sampling frequency is $F_s = 10Hz$;
2. IQ imbalance removing using Gram-Schimdt method;
3. DC offset removal with the circle fitting and centre tracking method;
4. Arc rotation case if it is necessary;
5. Phase demodulation - angle computation;
6. DC offset correction by subtracting its averaging value.

Baseband signals plots (signal $g(n)$) for both tests are shown in Figure 3.23.

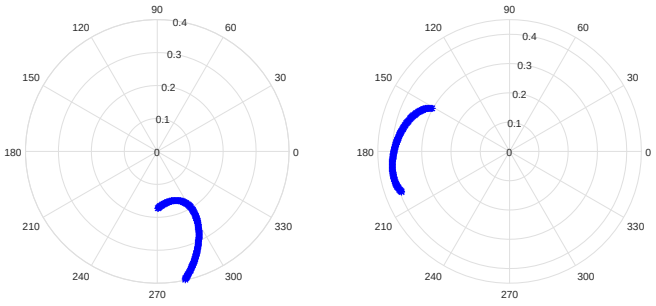

(a) (b)

Figure 3.23: Baseband $g(n)$ polar plot: (a) Test 1, (b) Test 2.

The **first simulation** was performed in favour of avoiding the signal wraps, with a view to test the performance of a simple AT with the presence of IQ imbalance and DC offsets.

By following the algorithm steps listed above, after downsampling the Gram-Schmidt method is applied, using the relation (3.29), in order to re-stablish the circle form to the arc that was corrupted by the IQ imbalance. Figure 3.24a shows how the formed arc fits an ellipse. Afterwards, a circle fitting is performed with the view to determinate where is the arc's centre and thus remove the DC offsets. The result of this procedure is shown in Figure 3.24b, where the arc fits a perfect circle. The AT can only be applied if the signal is centred in zero in the polar plot. The opposite effect is represented by Figure 3.25a where there is a distortion in the recovered signal.

On the other hand, Figure 3.25c shows the correct signal after phase demodulation and the DC offset correction (signal $y(n)$), proving the importance of the DC component removal. This plot is made according to the relation phase/wavelength, as reported by equation (3.20), which stablish the chest-wall motion in meters, according to phase in radians.

Other important aspect in the respiratory signal recover is the possibility of wraps to occur. If the target's position is such that the signal's phase reaches the π value, wraps will occur. The **second simulation** was performed in order to observe this effect. Figure 3.24c and Figure 3.24d show the ellipse fitting and circle fitting after imbalance compensation, respectively, for the second simulation. Figure 3.25b shows the recovered with wraps.

It it possible to recover the original form by rotating the complex signal the sufficient value of phase so the arc doesn't reach π, as it was seen in section 3.3.2 (see figure 3.26). The second simulation is also used to exemplify this procedure. The result after arc's rotation is shown in Figure 3.25c

Finally, after a successful phase demodulation, the respiratory rate is achieved. The spectral estimation result is shown in Figure 3.27.

This figure comprises the spectral estimation for both tests. It is possible to observe that the highest spectral component is approximately 0.3 Hz, as it was supposed to. Thus, is possible to recover the respiratory rate in scenarios where IQ imbalance and DC offset are present in the received signal. The conversion Hz to Breaths/min is made under the relation (3.50):

$$[BPM] = 60seg * [Hz] \tag{3.50}$$

Future work should comprise methods to recover the respiratory signal from stronger disturbance sources, such as the random and uncontrollable subject's movement while

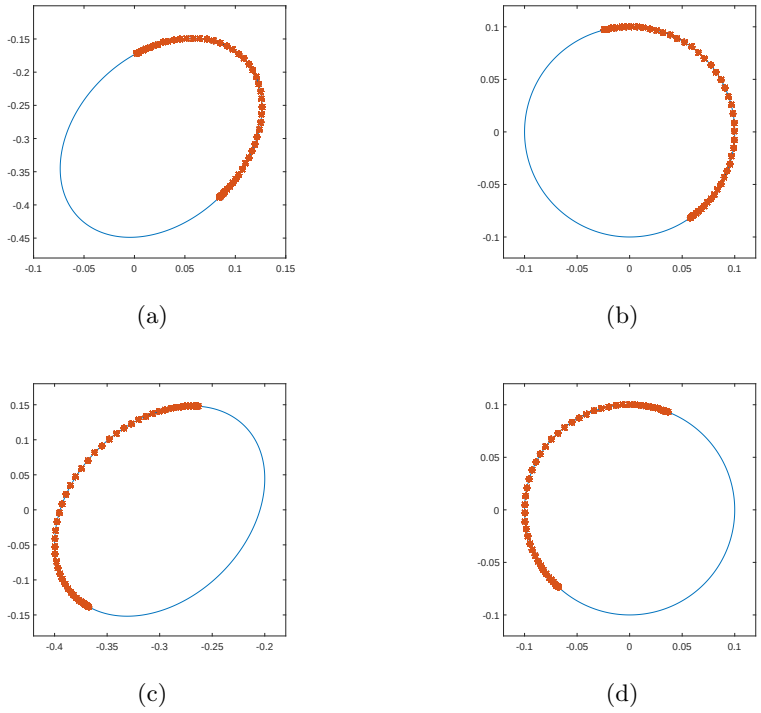

Figure 3.24: Arc fitting before and after the imbalance compensation and DC offset removal: (a), (b) For test 1, (c), (d) For test 2.

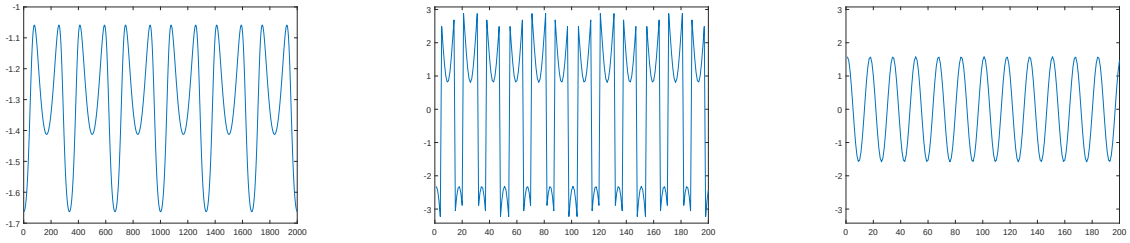

Figure 3.25: Respiratory signal after phase demodulation $y(n)$: (a) in case of DC offsets presence (Test 1), (b) Corrupted by phase wraps (Test 2), (c) Without DC offset and after rotation (Test 1 and 2).

---

the bio-signals are being monitored or the presence of a strong source of noise when the monitoring environment faces bad conditions, for instance, patients being monitored in moving ambulances, or a bio-radar embedded in a car for driver's bio-signals monitoring. In these cases it is difficult to recover an accurate respiratory rate, and more robust algorithm and techniques should be developed, as we will see in chapter 6.

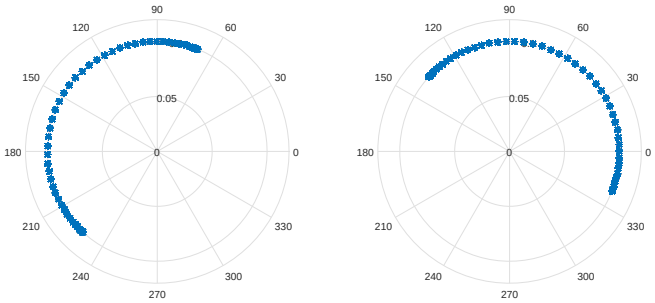

(a) (b)

Figure 3.26: Phase rotation in case of wraps: (a) Arc varying around π in the polar circle causing wraps, (b) Arc after phase rotation.

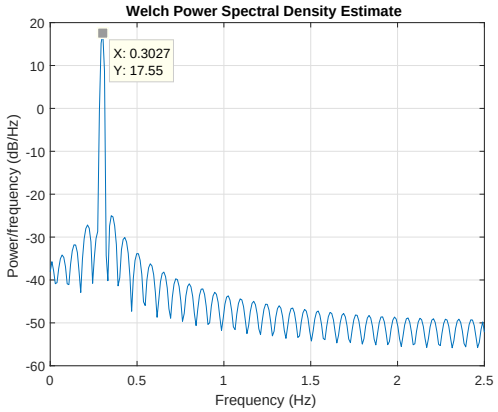

Figure 3.27: Respiratory signal's spectral estimation obtained with ***pwelch*** function from MATLAB.

3.6 Heartbeat and Respiration Signal Separation

A persistent problem in the bio-radar technology development is the heartbeat signal extraction from the respiratory one. This is a challenging task because the respiratory signal is 100 to 1000 times stronger than the heartbeat and due to their proximal spectral components they are superimposed in the received signal, [3]. In this section, some methods that were previously implemented are presented and also a new approach is introduced.

3.6.1 Filters and Alternative Methods

The most intuitive method for signal separation, assuming different frequency representations, is by filtering. In this scenario both breathing and heartbeat can be filtered with band-pass filters in MATLAB after sampling.

In order to select the best filter implementation to use, some characteristics should be taken into account such as the group delay, linear phase and the transition band slope. The size of the harmonics of the heartbeat signal requires a flat group delay over the harmonics, so the filter order should be a trade-off between the group delay and the slope of transition band. Group delay is the derivative of the phase change between the filter's input and output,

as a function of frequency. If the group delay is constant over the passband, no distortion is introduced to the signal. In FIR filters with greater order, the group delay is longer. Linear phase is also an important requirement in this case, because the information is present in the modulated signal, hence can be distributed by the harmonics in the baseband signal. The phase shift of FIR filters is linear within the passband, therefore it represents a good option in this matter. High FIR filter order implement steeper transitions to the passband/stopband. However, the amount of group delay is proportional to the filter order. Usually IIR filters have a non-linear phase but are efficient in terms of passband slope comparing with FIR filters, [3].

Some examples of the filter usage are the following: in [3] a Kaiser high-pass FIR filter was implemented, with a cutoff frequency of 0.675 Hz, followed by a Kaiser low-pass FIR filter with cutoff frequency equal to 20 Hz to eliminate the out-of-band noise that could interfere in the rate finding. In [18], [17], band-pass Flat-Top FIR filters are applied with a frequency range of 0.8-10 Hz. Also in [2] and [26] band-pass filters were applied, within a frequency range of 0.8 to 2 Hz, using a 1000th order FIR filter with Hanning window. Here signals were acquired during apnea periods.

If a band-pass filter is used to isolate the heartbeat signal, harmonics of the respiratory signal could still be present in the heart signal because its lower fundamental frequency. This effect is even more evident when small wavelengths are used. In [1] a mathematical description of the baseband signal for a small wavelength carrier is done, proving the occurrence of multiple harmonics. This effect reveals a disadvantage in the filter usage.

In addiction, [35] used FIR filter and also adaptive filters, which did not produce ideal results. In this paper the wavelet transform (WT) is proposed as a possible solution for bio-signals separation. The WT is a time-scale representation technique used to localize information on a signal by its decomposition in time or frequency domain, using a limited number of wavelet coefficients. In lower frequency band, wavelet transform has lower time resolution but higher frequency resolution and vice-versa, which makes easier the signal's separation task.

Other alternative method to the filter usage is mentioned in [8], where the same harmonic effect is pointed out. Therefore, the usage of Blind Source Separation (BSS) algorithms is proposed, which separates multiple mixed signals from the original source signal without requiring any information in advance. Thereunder the Independent Component Analysis (ICA) is pointed out, which consists on a computational method to separate a signal into a sum of subcomponents, assuming that they are statistically independent from each other.

3.6.2 Total Variation Denoising Method

The Total Variation Denoising (TVD) is a regularization method for noise reduction, which revealed being efficient due to its edge preservation ability, [36]. Image denoising consists in an image noise removal process, using for instance filtering, partial differential equations and wavelet. By applying the TVD method in 1D signals it is possible to remove noise and preserve sharp details at the same time. In this case, heartbeat signal is seen as noise in the respiratory signal. In this dissertation, this method was applied for one bio-radar experiment, where the extracted signal is obtained under specific conditions and it presented successful results. For this purpose a MATLAB function was used to implement a discrete TVD using a primal-dual interior-point solver.

The output of the used function is obtained by the minimization of a cost function (3.51)

over the variable x, [36]:

$$E = \frac{1}{2}\Big(\sum (y - x)^2\Big) + \kappa * \sum \Big(|D * x|\Big) \tag{3.51}$$

where D is is the first difference matrix and x is the denoised signal in the output. The κ is a regularization parameter that controls the degree of smoothing, [36]. The second term of the equation (3.51) measures the fluctuation of x and it has more weight for higher values of κ.

The results of the implementation of this method are presented in chapter 5.

Chapter 4

Real-Time Prototype of Bio-Radar

In the framework of this dissertation, a real-time measuring system was developed as a prototype, with the goal to prove the concept exposed and discussed in the course of this document. Regarding the discussion made in chapter 3, the choices led to a prototype and DSP algorithm (already presented at the end of chapter 3) and their implementation is reported in this chapter.

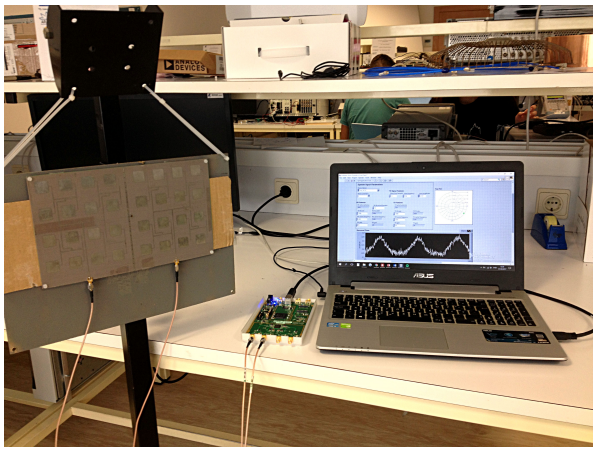

Figure 4.1: Prototype set up.

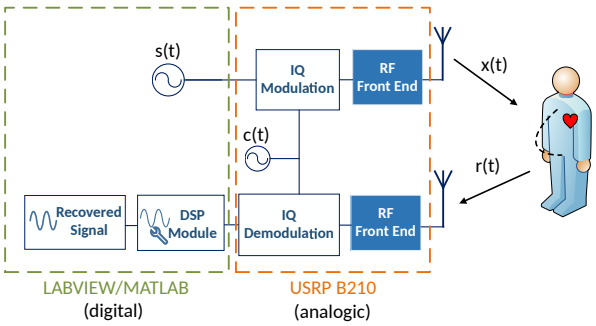

Figure 4.2: Simplified prototype block diagram.

The prototype consists in a real-time measuring system implemented in the LabVIEW

programming environment. The system uses two antennas, one for transmission and the other for signal reception. The front-end is based in a SDR implementation. Figure 4.1 shows a functional diagram of the prototype and in Figure 4.2 is detailed how and where each block is implemented.

During the development of this system, the LabVIEW software revealed some limitations, in particular regarding the use of available memory. Also the method of ellipse fitting used in MATLAB was too complex to implement in LabVIEW. Therefore, it was necessary to divide this prototype in two separate modules:

1. Real-time measurement system, which acquires and displays signals without any arc constrain compensation. Also the respiratory rate is estimated in real-time;

2. MATLAB script that apply the DSP algorithm described in chapter 3 for DC and IQ imbalance removal in the signals acquired with LabVIEW.

The aim of this chapter is to describe in detail all the prototype components, starting by the antennas characteristics, followed by the front-end description and finally the real-time DSP algorithm implementation in both LabVIEW and MATLAB platforms. Justifications for the software selection are also exposed.

Last section describes a simulator, the CWS, built for calibration and validation purposes. Note that in chapter 3 we had defined signal denomination for each stage of the DSP chain and the same nomenclature is maintained in this chapter.

4.1 Antennas

In this section characteristics of the used antennas are presented. For both Tx and Rx, two 4×4 patch array antenna were used and they are shown in Figure 4.3. Scattering parameters

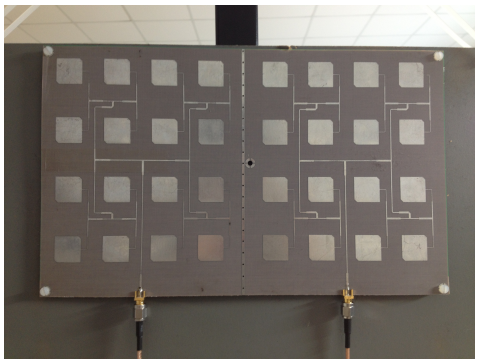

Figure 4.3: Patch antennas for Tx and Rx.

were measured, more specifically the reflection coefficient (S_{11}) and the reverse gain (S_{12}) in order to analyse the cross talk between Tx and Rx antennas (see Figure 4.4).

Both used antennas are highly directive, which means that their main lobe should be narrow but with significant high magnitude when comparing with its side lobes. Therefore, due to the directive nature of these antennas, the crosstalk between transmission and reception is expected to be low. In Figure 4.4b the magnitude of S_{12} parameter is around -60 dB, which is a relatively low value.

The S_{11} parameter shown in Figure 4.4a demonstrates that the used antennas have a high reflection coefficient for 5.8GHz, approximately -0.84 dB, revealing a non adaptation at the selected frequency, if comparing with other frequencies, such as 4.69 GHz which has a S_{11} of -14.41 dB or 5.25 GHz which has a S_{11} of -9 dB, approximately. Unfortunately, this misfit was only noticed in the end of this project. The S_{11} parameter represents the fraction of the injected power that is reflected back to the source, which in this case is the majority of the injected signal. However, despite this mistake, results presented in chapter 5 shows that even under these shallow conditions the prototype works properly.

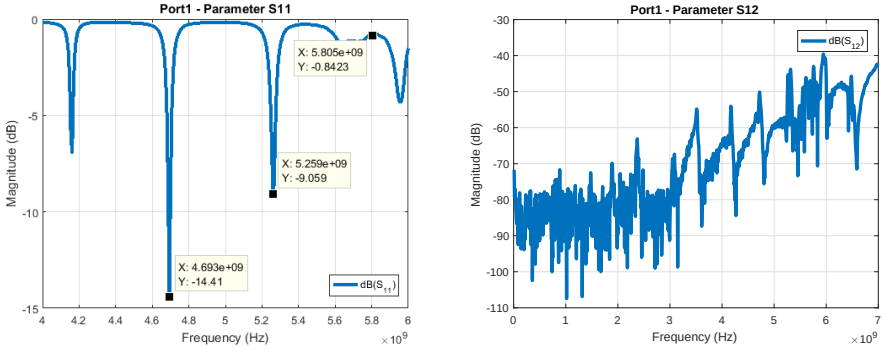

(a) (b)

Figure 4.4: Antenna's scattering parameters: (a) Reflection coefficient (S_{11}), (b) Reverse gain (S_{12}).

The acceptable performance achieved with the proposed set-up can be justified by its appropriated radiation pattern. Therefore, the radiation diagram of this antenna (from now on called antenna A) was compared with the radiation diagram of other antenna, which were adapted at the same frequency and with the same design (from now on called antenna B). The S_{11} parameter of the antenna B is plotted in Figure 4.5 and its adaptation at 5.8 GHz is verified, once it has a low reflection coefficient, that is approximately -11.76 dB. Figure 4.6 presents the radiation diagram of both A and B antennas for direct and cross

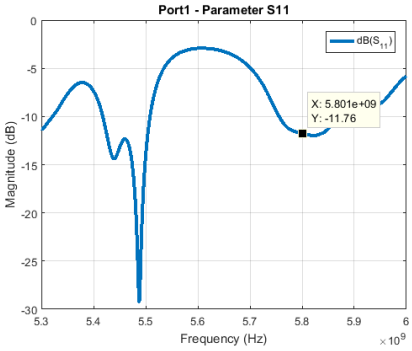

Figure 4.5: Reflection coefficient of the Antenna B (S_{11}).

polarization. The radiation pattern for antenna A presents high magnitude, always around -20 dB independently of its orientation. The same behaviour is observed for antenna B, although its magnitude value is higher than the ones from antenna A (approximately -15

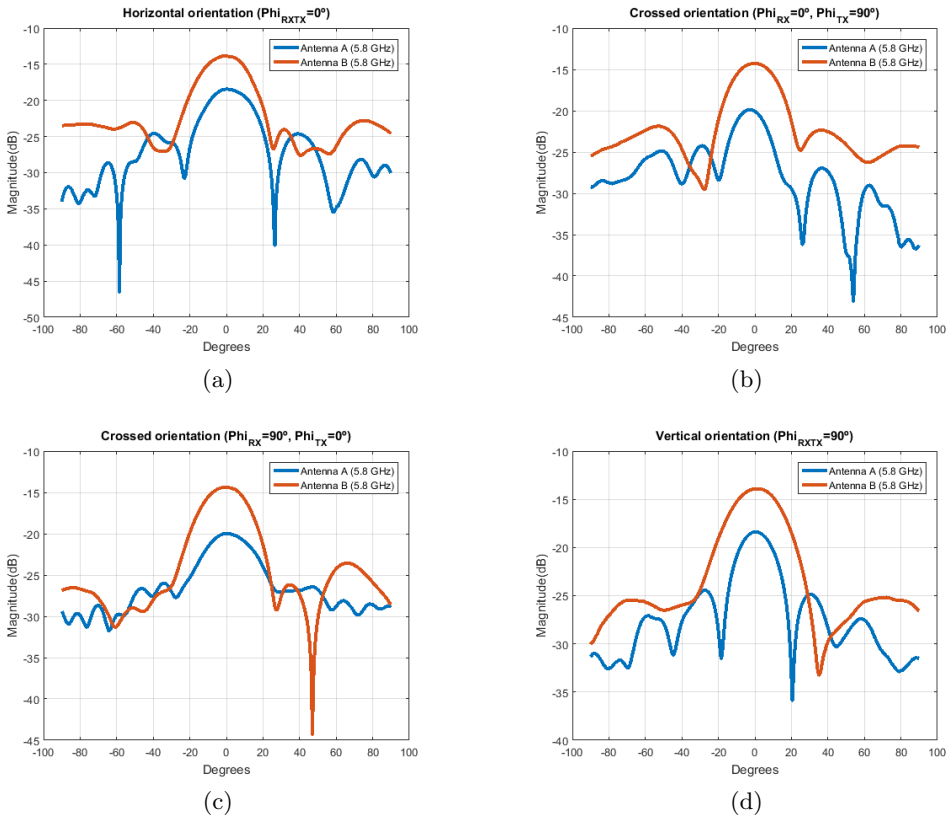

Figure 4.6: Radiation pattern of antenna A and antenna B: (a) Horizontal Polarization, (b) Horizontal-Vertical Polarization, (c) Vertical-Horizontal Polarization, (d) Vertical Polarization.

dB), which was expected since antenna B is more adapted at 5.8 GHz than antenna A. Other key characteristic that can be observed is the side lobes: the radiation pattern of antenna A has side lobes with significantly lower magnitude than the main lobe. Finally, the main lobe of antenna A is narrower than the one from antenna B, which reveals more directivity.

The radiation patterns presented in Figure 4.6 are similar for both antennas and they justify the good results presented in chapter 5. Considering the higher magnitude of the main lobe and low magnitude of sidelobes in the case of antenna B, it is possible to conclude that if antennas with a better S_{11} were used instead the currently used ones, the prototype radiation efficiency would increase.

4.2 USRP

As referred previously in chapter 2, SDR are reconfigurable platforms that allow a very flexible RF front-end hardware to be controlled via software. With this platform is possible to configure digitally its input and outputs (receiver and transmitter), regarding the required frequency and sampling rates, [26]. SDR performs the modulation and demodulation of the RF signals digitally, allowing to do any kind of DSP directly to the baseband signals.

In the context of the developed prototype, the front-end should be implemented in full

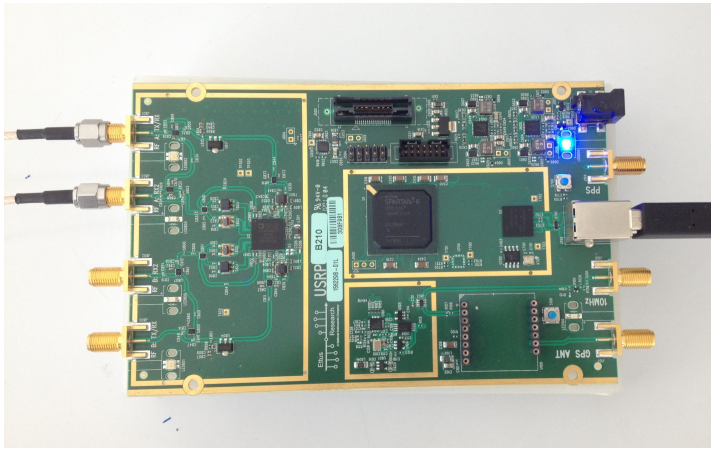

Figure 4.7: USRP B210.

duplex mode, in order to allow simultaneous Tx and Rx which is an indispensable feature for a correct CW radar operation. For this reason, an USRP B210 board was used (shown in Figure 4.7), developed by Ettus Research, with an Analog Devices chip that incorporates RF front-end components, such as Tx and Rx mixers and the LO implemented by a Phase Locked Loop (PLL) with VCO.

The overall USRP B210 board characteristics meets our prototype requirements, which are the following [37]:

- Continuous RF coverage from 70 MHz − 6 GHz;
- Two integrated channels - 2 Tx and 2 Rx;
- Full duplex operation mode with a bandwidth of 56MHz;
- Sampling rate up to 61.44 MS/s;
- Powered by USB 3.0;
- Analog Devices AD9361 chip with integrated direct-conversion transceiver;
- Full software support for UHD, ensuring the compatibility with several development platforms.

The general USRP architecture is presented in Figure 4.8. The LO composed by a VCO and PLL guarantees the continuous carrier frequency during modulation and demodulation processes. The signal created in this oscillator is used in both mixers for up-conversion and down-conversion and shares the same reference clock. Oscillators based on PLL use feedback to maintain a certain level of voltage in their outputs, using a VCO to produce voltage according to the phase detector in the beginning of the feedback loop. As we will see further, the time took by the PLL to converge is not deterministic, hence the generated signal phase value is a stochastic variable. Due to this, the acquired signal polar plot will present a different arc position everytime the system restarts and the PLL needs to converge again. This unkown arc position can also be caused by changing the nominal distance between the testing subject and the bio-radar.

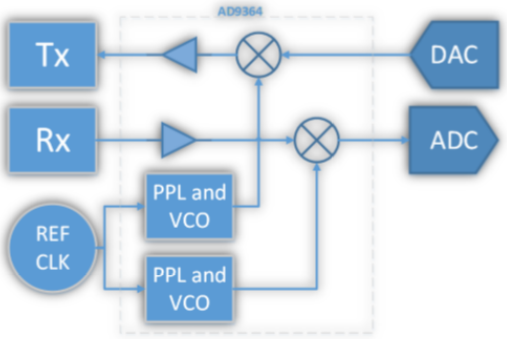

Figure 4.8: General USRP Architecture, [26].

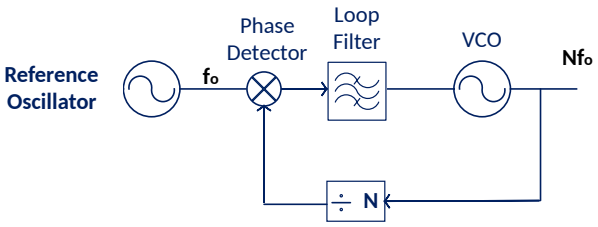

Figure 4.9: PLL oscillator architecture, [38].

Regarding Figure 4.2, the USRP operation stands as follows: the signal is generated digitally, converted to the analog domain through a DAC and transmitted after up-conversion, using the carrier frequency generated by the PLL. In the reception chain, the down-conversion is done directly from the RF signal to the baseband using the same LO signal, in other words it works as a homodyne receiver. After digitized by the ADC, the signal is presented in the digital output of the USRP in baseband for further DSP processing, that will be performed in LabVIEW or MATLAB.

4.3 Software Platform Selection for Real-Time Operation

In order to perform a real-time acquisition system, some options were studied regarding their processing features, compatibility with the UHD, available memory and directness in the implementation. The explored options are the following:

1. GNU Radio software;
2. Matlab as acquiring platform;
3. LabVIEW.

For every option, an Application Programming Interface (API) is required in order to establish the interface between the SDR and the selected software. UHD offers support in some development platforms including the ones mentioned previously.

4.3.1 GNU Radio

GNU Radio is an open source and free software which supports USRP platforms. Its development environment is based in a simplified block diagram, where each block has a source code in Python. Blocks are disposed in the developing space called canvas and connected to each other performing a visual code implementation. The first approach for the bio-radar prototype implementation was designed in this software. The block diagram is shown in Figure 4.10 and its application is detailed further.

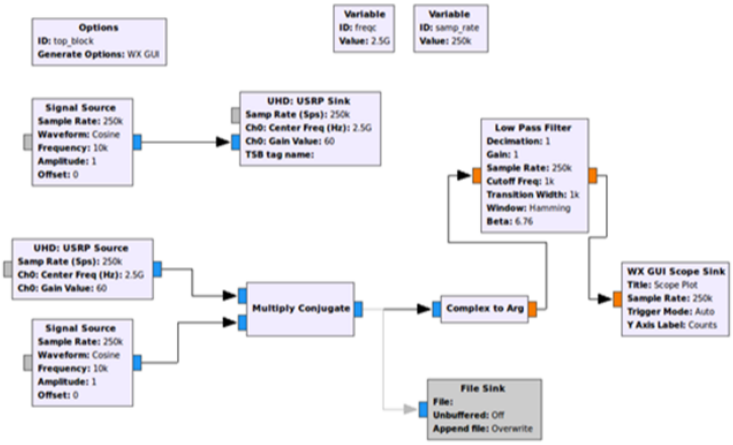

Figure 4.10: Block code implementation for Bio-Radar using GNU Radio software.

This interface is separated in two main chains, one for the signal's transmission and the other for its reception and process.

Transmission Chain

The transmission chain is composed by two blocks: the *Signal Source* block which generates a sinusoidal signal with the required specifications, such as the frequency offset of $f_o = 10$ kHz, sample rate of $F_s = 250$kHz (that should be the same in every block in canvas), the signal type that is in this case a cosine signal and its amplitude that is equal to 1. The *Signal Source* block is connected to the *UHD:USRP Sink* block. This establishes the interface between the user and the radar's front-end. Transmission features are defined: sampling rate, carrier frequency that is in this case $f_c = 2.5$ GHz and the transmission gain (set by the LNA gain).

Reception Chain

The reception chain is where the acquired signal is processed. First the RF signal is acquired by the *UHD:USRP Source*, that in this implementation uses the same configuration parameters used in the *UHD:USRP Sink* block from the transmission chain. The output of this block is a baseband complex signal, which is then mixed (using a *Multiply Conjugate* block) with an equally complex sinewave with frequency f_o, in order remove the frequency offset added to avoid the LO leakage. Later, the AT is implemented by the block *Complex to Arg* and the result is displayed after a low-pass filtration.

Despite its optimal compatibility with the UHD and its quick learning software features, GNU Radio has its limitations on displaying the signals in real-time. After phase extraction, only the last samples were displayed and a historic trace of the acquired samples was not

supported. A possible solution to overcome this problem was to modify the source code specifically in the display block called *WX GUI Scope Sink*, although deep knowledge of the source code was needed. However, for non-real time implementation GNU Radio can be a possible solution, by recording the acquired data into a binary file (using *File Sink* block) and read it in MATLAB afterwards.

4.3.2 MATLAB

In the framework of this thesis, MATLAB is used to implement the DSP algorithm, specially for more complex operations such as IQ imbalance compensation and ellipse fitting for DC removal, leading to a more accurate respiratory signal extraction and its frequency rate computation. Once the required DSP is implemented offline in MATLAB, a real-time solution where the data is processed in real-time, using the created signal processing algorithm, would be a suitable solution.

As seen before in this chapter, UHD can be used in several development environments including MATLAB. There are several program examples which use UHD in [39], that can be used in MATLAB to interact with USRP devices. For example, the application '*txrx_loopback_to_file.exe*' allow a RF signal Tx and it Rx in full duplex mode and saves the data in a binary file. This system command accepts as inputs Tx and Rx features, such as sampling frequency, gain, number of acquired samples (which also defines the duration of this procedure) and the transmitting signal characteristics.

Although, the goal of this prototype is to achieve and display the phase variations on the received signal in real-time, which was not possible to implement in this case, because the written binary file is only processed after the experiment is over. Even if the data is acquired in small subsets of data and treated immediately, is not possible to implement in real-time because the connection with USRP board needs several seconds to initiate and has to be restarted everytime a new subset is obtained, which leads to a massive lost in samples.

Other option would be the usage MATLAB's *Communication Toolbox*, which uses system objects to simulate dynamic systems where input are always changing inducing the same effect in the output. Thus, this toolbox have functions, blocks and system objects for this purpose.

4.3.3 LabVIEW

The LabVIEW software is a program development environment, developed by National Instruments that uses a graphical programming language, rather than text-based language like C, for instance. It has several libraries of functions that supports different tasks, such as data acquisition, instrument control, data analysis, data presentation and data storage, [40]. Up next we will see that LabVIEW programming is seen as a modular type because it can divide a complex operation in successive simpler operations.

The LabVIEW programs are called Virtual Instruments (VI), which are dataflow diagrams seen as source codes and can be disposed hierarchically. They are also seen as different modules that can be connected to each other. In this context, a VI inside other VI is called a subVI, [40]. Each subVI can be executed by itself turning debugging task much more easy when it is needed.

The source code of the VI is developed in the block diagram panel which is directly related to a user interface called front panel. In the front panel there will be the plotted graphs, input

controls, value indicators, etc.

The prototype's goal is to display the respiratory signal in real-time keeping a historic trace window. At the same time is required to compute the respiratory rate and display the result over the time. The LabVIEW software is compatible with UHD, as well as the other options mentioned previously, moreover is in an advantageous position regarding the problems pointed out on each option. It has a functions palette dedicated to NI-USRP, which contains devoted blocks to open/close sessions in order to write data in a Tx channel and fetch it from the Rx channel. As we will see further, this development environment allows full duplex operation mode and data processing in real-time. In the front panel, there is a *Waveform Chart* that can keep a historic data trace and therefore the respiratory signal can be drawn over the time.

In the next sections the algorithm implemented in LabVIEW is fully described and the obtained results will be discussed in the next chapter.

4.4 Real-Time DSP Implementation

In this section, the implementation in LabVIEW of the DSP algorithm defined in chapter 3 is explained. As referred previously the LabVIEW implementation is only for demonstration purposes, as well as a manner to record data that is processed further in MATLAB. Thus, the implemented algorithm is simpler as shown in Figure 4.11. Each stage of the algorithm is executed by different subVI, built for that only purpose. The system will operate with the subsequent main features:

- Transmitted signal $s(n)$:
  - Tone frequency $f_o = 10$kHz - also known as the offset in frequency;
  - Tone amplitude $A = 0.707$;
  - Number of sine samples $N = 1000$ - which is a necessary parameter for the sampling information to generate a signal.
- Tx/Rx features:
  - Sampling rate $F_s = 100$kHz - this value was selected having in mind the necessary resolution for the *To Baseband* block. This is explained later in section 4.4.2;
  - Gain $G = 20$dB - which corresponds to the gain from the Power Amplifier (PA) in the Tx chain and LNA amplifier in the Rx chain, in the USRP front-end;
  - Carrier frequency $f_c = 5.8$ GHz.

4.4.1 Full Duplex Implementation

In order to operate in full duplex mode, Tx and Rx must be conducted simultaneously. This is possible using the same block diagram for the set up of both Tx and Rx implementation. They pursue the same principle which is structured by the following steps (also shown in Figure 4.12):

1. **Open Session:** Tx/Rx session needs to be opened according to the specified device name. In this case the device is the USRP B210.

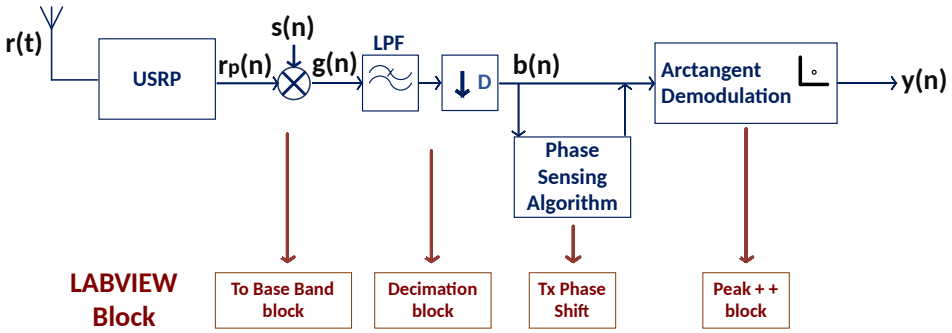

Figure 4.11: DSP implemented in LabVIEW.

---

2. **Channel Selection:** The USRP B210 board has two channels for Tx and other two for Rx. Therefore, the channels being used needs to be selected.

3. **Channel Parameters:** Tx/Rx operational parameters must be specified, such as: sampling rate of ADCs or DACs, carrier frequency and Tx/Rx Gain;

4. **Signal Generator:** In the Tx section, a complex waveform should be generated with the same sampling frequency specified in the previous step and the frequency offset f_o needed due to phase noise elimination.

5. **Rx Initiate:** In the Rx section, acquisition mode needs to be initiated after the Rx session opening. It should also be aborted before the session close.

6. **Fetch Rx Samples and Write Tx Channel:** In a while loop a certain number of samples (N_s) from the wave generated previously, are written in the Tx channel, or read from the Rx channel. In this case, each iteration reads $N_s = 1000$ samples.

7. **Close Session:** when the program is aborted by the user or due to any perturbation, both Tx and Rx sessions are closed.

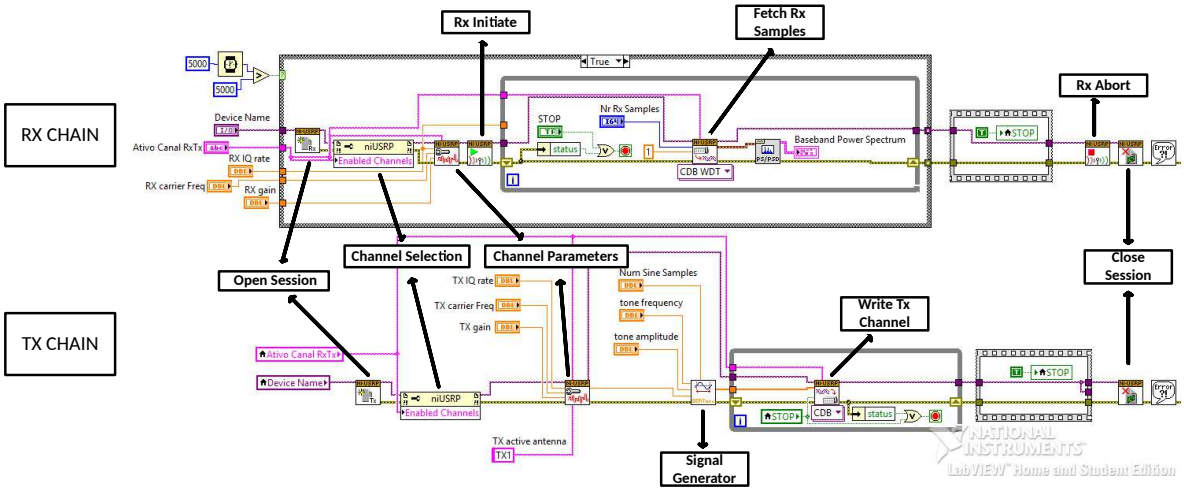

Figure 4.12: Full duplex implementation in LabVIEW.

This USRP board is configured to start reception process before the transmission, hence noise floor is received during the first seconds. Therefore, in the Rx section an *if condition* is done, where the argument is an elapsed time equal to 10 seconds. It means that the acquisition (reception) only starts after 10 elapsed seconds since the system initialization. This condition guarantees that initial noise from an empty reception (without the reception of the reflected signal) is not displayed in the rolled chart and also not recorded in the binary files.

The functions needed to perform this steps are in the Functions Palette more specifically in the tab of *Drivers I/O*.

4.4.2 Down-Conversion in Real Time

As referred previously, the signal coming from the USRP is already in baseband, it means that is IQ demodulated and the carrier is no longer present. Although, the offset to avoid the LO leakage should be removed ($f_o = 10$kHz) as well. Despite this frequency value being known, it is not possible to use that exact value to cancel this offset because the hardware that generates the transmitted signal is not perfect, so the received signal has a slightly different frequency from the one defined. Thus, a PSD of the Rx signal should be made with a view to detect its higher spectral component and use it to perform the accurate down-conversion.

To Base Band subVI was created for this purpose. It has as inputs:

- **Data**, which is the input signal (data type - complex waveform);
- Inputs for frequency axis generation:
  - **Sweep Points**, is the N_s of the input signal;
  - **Start Freq**, corresponds to $-F_s/2$;
  - **Stop Freq** , corresponds to $F_s/2$;
- Inputs for an ancillary complex signal generation:
  - **Num Sine Samples**, is the number of samples (previously defined as N) of the generated sinusoid;
  - **Tone amplitude**, is the amplitude of the generated sinusoid signal;
  - **Coerced IQ Rate**, is the sampling frequency of the system (F_s);

Inside this subVI the PSD is computed and the frequency from the input signal is acquired by a peak detector. The obtained peaks are related to an index axis set according to the number of input array elements, but it should be related to a frequency axis in order to get the predominant frequency component. Therefore, regarding the F_s used for data fetch, a frequency axis is generated by the subVI called *Samples to Freq*. Although, for its implementation parameters like the starting and stopping frequency of this axis, as well as the resolution (given by d_f) should be computed. For this reason another subVI called *Freq Index Axis* is created, (Figure 4.13). It receives at its input the current F_s and the Ns acquired in each iteration of the acquisition *while loop*.

$$d_f = \frac{F_{stop} - F_{start}}{Ns} \tag{4.1}$$

In order to cancel the offset added previously before the signal's transmission, *To Baseband* block execute the following steps, that are also illustrated in Figure 4.14:

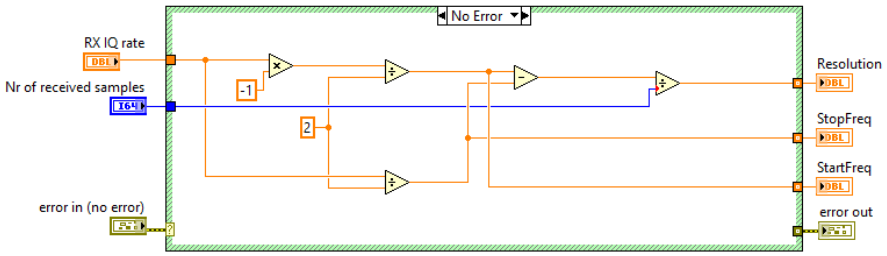

Figure 4.13: *Freq Index Axis* block in LabVIEW.

---

1. The PSD from the input signal is computed. The output of the *PSD.vi* is a cluster that encompasses a vector with the magnitudes of the spectral components from the input data, beyond other parameters;

2. The maximum value of the magnitude vector is extracted, as well as its index. The frequency axis of the PSD graphic starts in $-Fs/2$ and stops in $Fs/2$. As mentioned previously the *Array Max & Min.vi* returns an axis that does not correspond to the real frequency values required. By knowing the d_f, it is possible to create an array with frequency values that are correspondent to the magnitudes vector, which lead us to the next step;

3. Frequency axis is created using the *Sample to Freq* block. The output of this block is an array with the frequencies separated according to the resolution d_f. The best d_f is the smallest value possible regarding F_s, N_s and the processing memory of LabVIEW. Resolution is a key factor, because higher d_f values could lead to an inaccurate frequency detection. The best resolution achieved in this application was 100 Hz, for a $Fs =$ 100kHz and $Ns = 1000$. The output axis starts with F_{start} frequency value, finishes with F_{stop} (from the *Freq Index Axis* block) value and is filled with a *for loop* and a *shift register* where each array value is the result of a cumulative sum of the resolution value with the previous array element value. The final array length is 1000 and comprehends a bandwidth equal to 100kHz;

4. Once the frequency axis is created, it is possible to obtain the frequency value which has the highest spectral power density. Thus, in this step a complex signal is generated with this frequency value;

5. Finally, the data signal is mixed with the complex sinusoid created in the previous step and the result is a signal without the offset f_o.

4.4.3 Decimation Block

In the same system/algorithm is possible to work with the same signal at different sampling rates. Previously in chapter 3, we saw that the extracted bio-signals are close to DC and have a low bandwidth compared to the sampling frequency. Therefore, decimation is needed.

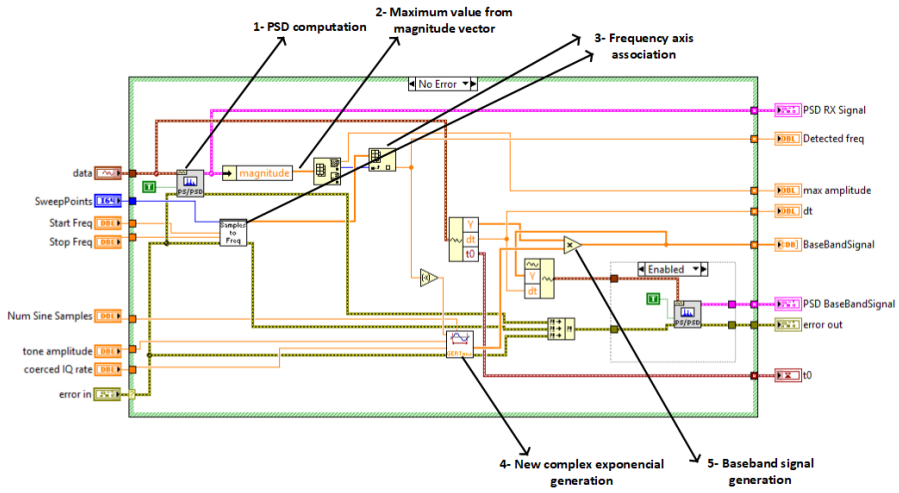

(a)

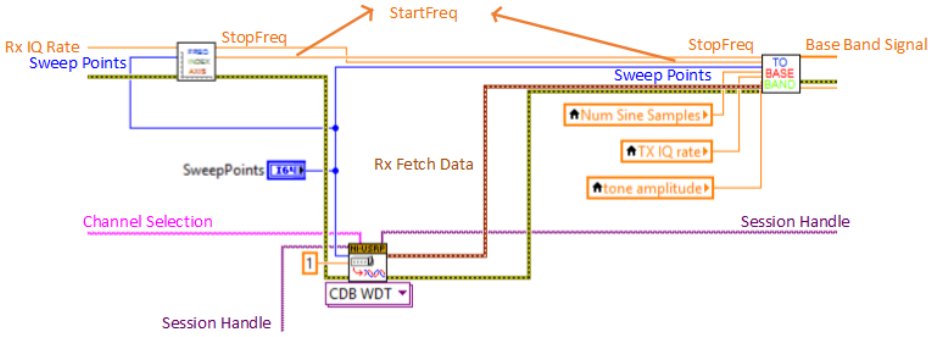

(b)

Figure 4.14: Down-conversion procedure in LabVIEW: (a) *To Base Band* block implementation, (b) ancillary blocks needed for the *To Base Band* block operation.

The Rx data is fetched using a *while loop* to acquire signal samples and each iteration acquires 1000 samples. This means that after the *To Base Band* block, signal is represented by 1D array of 1000 complex samples. In this case, downsample means reduce this array length in a certain factor, that is in this case $M = 100$ resulting in the new $Fs = 1000$Hz.

The input of the *Decimation* block is the baseband signal $g(n)$. Regarding Figure 4.11, the decimated signal is called $b(n)$ and mathematically is represented by:

$$b(n) = g(Mn) \tag{4.2}$$

where M is the decimation factor and thus the new sampling frequency is:

$$Fs = \frac{Fs}{M} \tag{4.3}$$

Decimation block comprises an anti-aliasing filter and a *for loop* that builds a new array with some input samples as we will explain further. It has as inputs:

- **Signal In** - input signal desired to be downsampled;

- **IQ Rate** - sampling rate of the input signal;
- **New Rate** - new sampling rate that we want to achieve;
- **Signal dt** - decimated time interval between data points.

First the input signal is low-pass filtered in order to avoid the aliasing effect, or in other words, to avoid the superposition of other spectral components that do not represent the original signal and will only add noise. In this application, a low-pass 100^{th} order FIR filter is used with Hamming window, where the cut-off frequency is the new sampling frequency ('New Rate' input) required after decimation. Hamming window was selected because is attenuates side lobes uniformly in -60 dB, reducing the undesirable leakage. The down-conversion procedure is shown in Figure 4.15. This block uses a *for loop* (after anti-aliasing filter)

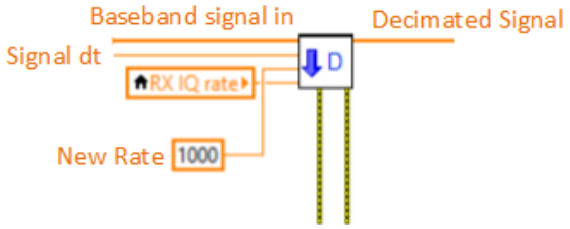

(a)

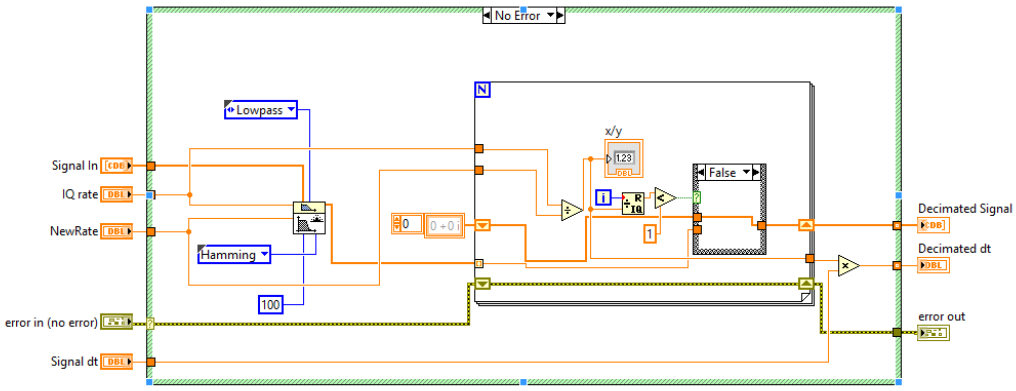

(b)

Figure 4.15: Down-sampling procedure in LabVIEW: (a) *Decimation* block, (b) Block diagram of the *Decimation* implementation

to fill in a new array. If we want to decimate with a factor M, it means that the array will have one in M samples of the old array.

By using the input parameters 'New Rate' and 'IQ Rate', the factor M is computed in order to define a condition to fill the array.

$$M = \frac{NewRate}{IQRate} \tag{4.4}$$

If the *for loop* iteration is multiple of M, the correspondent sample is inserted in the new

array otherwise the array is the same as it was in the previous iteration. In this case, a sample is picked each 10^{th} sample, conferring a new sampling rate of 1000 Hz.

4.4.4 Phase Wrap Avoidance

As already mentioned, PLL confers a random initial phase in the polar plot everytime the system initiates. This issue allied to the target's position relative to the radar can lead the signal to cross π, and hence wraps occur. Once the unwrap algorithm can not be performed, because in this stage data vector length is equal to 10 samples, an alternative is implemented.

The LO in USRP that generates the carrier frequency is the same in the Tx and Rx chain. Therefore the measured phase is the difference between both Tx and Rx signals, for instance, if the phase is zero it means that Tx and Rx are in phase. The transmitted signal has a defined initial phase equal to zero, thus in order to change the initial phase in the polar plot, the phase from the transmitted signal should be adjusted. In practice this is possible to do inside the *while loop* used to write data in the Tx channel. A boolean button is integrated in the display chart and serves as input in the *Phase Shift* sub VI block. Thus, if the user sees that the signal is close to the π value, presses the button and a phase shifted occurs according to the amount specified by the user through a control input.

Inside the *Phase Shift* subVI block, the new Tx phase value is computed regarding the following procedure: if the boolean button is pressed, a mean value of the current phase is computed and summed with the phase amount set by the user. This procedure is done in degrees, because it is more intuitive for the user to have a visual perception of how much the signal's phase should be adjusted. Afterwards, the generated signal is mixed with an exponential, which its phase is the result from the previous sum in radians, leading to the required shift rotation. If the amount of phase shift is not sufficient and the arc still achieves π, this procedure can be repeated and the new value of phase is the result of the sum with the previous result and the value present in the control. On the other hand, if the button is not pressed, the original complex signal is not changed. Figure 4.16 shows the *Phase Shift* block and its subVI implementation.

4.4.5 Respiratory Rate Measurement

In this subsection we will see two different approaches for the respiration rate measurement performed during the development of this prototype. The first approach is called "Cross Mean Value Algorithm" and was previously described in chapter 3. Despite its lack of robustness, its implementation in LabVIEW is also described. Furthermore, the current implemented technique based in the PSD computation is also fully described.

Cross Mean Value Algorithm

After the system initiates and the phase value is stable, during 10 iterations a buffer is filled with data samples, and the mean value of this buffer (which corresponds to the reference value P) is computed.

Then, a new buffer (B1) is filled in with the mean value of the extracted phase. Values from the position 0 and position 40 of the B1 are extracted and a second new buffer (B2) is filled. Buffer B2 serves as threshold and is refilled at each iteration multiple of 40, in order to compare within this interval. The conditional algorithm presented in section 3.4.2 is now

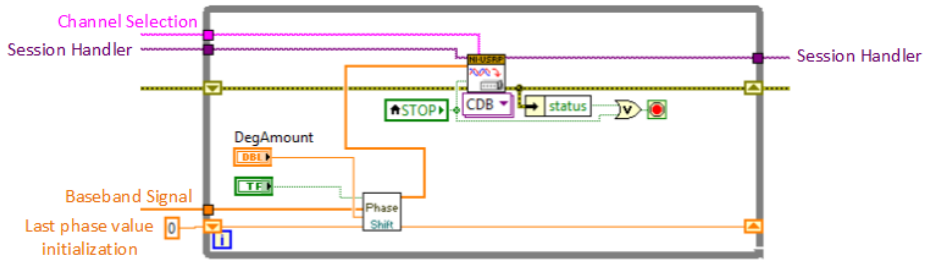

(a)

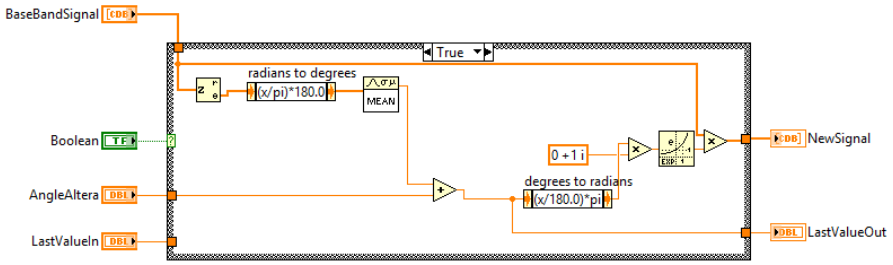

(b)

Figure 4.16: Phase shift procedure in case of wraps occur: (a) This procedure is done in the *while loop* used to write the data in the Tx channel, (b) *Phase Shift* block description.

---

applied. For each respiration detected an audible beep will sound and the total number of inspirations is updated.

PSD Algorithm

The chosen method for breathing rate computation is based on PSD using FFT computation with a sliding window. The implementation of this block is separated by three main steps:

1. Data division in subsets;
2. PSD computation;
3. Interpolation for a proper peak detection.

Figures 4.18 and 4.19 show the block diagram implemented in LabVIEW, where the first figure shows the first step implementation and the latter shows the last two steps.

1 - Data division in subsets

The overall system and algorithm is implemented in real-time using the datasets acquired iteratively at a sampling frequency of $F_s = 100$kHz. In each iteration, the acquired dataset has length equal to 1000 samples. Therefore, one second takes 100 iterations and 100 000 samples. After decimation, where the new $F_s = 1000$ Hz, the dataset length is reduced to 10 samples.

In order to have a considerable amount of data to perform proper PSD, 10 samples are not sufficient, so in this step a buffer is filled iteratively, by concatenating the 10 samples per iteration until it has a total length of 5000 samples. The filling process is shown in Figure 4.17. In LabVIEW it is only possible to fill in an already existent array, so it is initialized

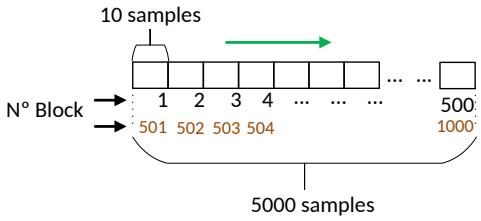

Figure 4.17: Buffer filling.

outside the main Rx *while loop* with '1'. Once in each iteration, 10 new samples are added to the buffer, the PSD computation starts only after iteration number $i = 500$ (in iteration 500 we have the buffer totally filled), in order to avoid the initialization values ('1') in the PSD computation. After the 500^{th} iteration, new data values replace the older ones, so at each iteration multiple of 500 we have 5000 new values.

The buffer length selection assured a balance between resolution and real-time rate computation, i.e. decrease the delay of the rate result, that is updated over time. Large buffer lengths create a higher resolution frequency estimation, although it takes too much time to fill in the first buffer and to update it with new values. For example, if we used a buffer with length equal to 10000 samples it would only be filled with new values at each 1000^{th} iteration and according to the sampling frequency it would take 10 seconds. In addiction, it would take too long to display rate changes that can eventually occur or even miss them. In contrast, small buffer lengths decrease the resolution.

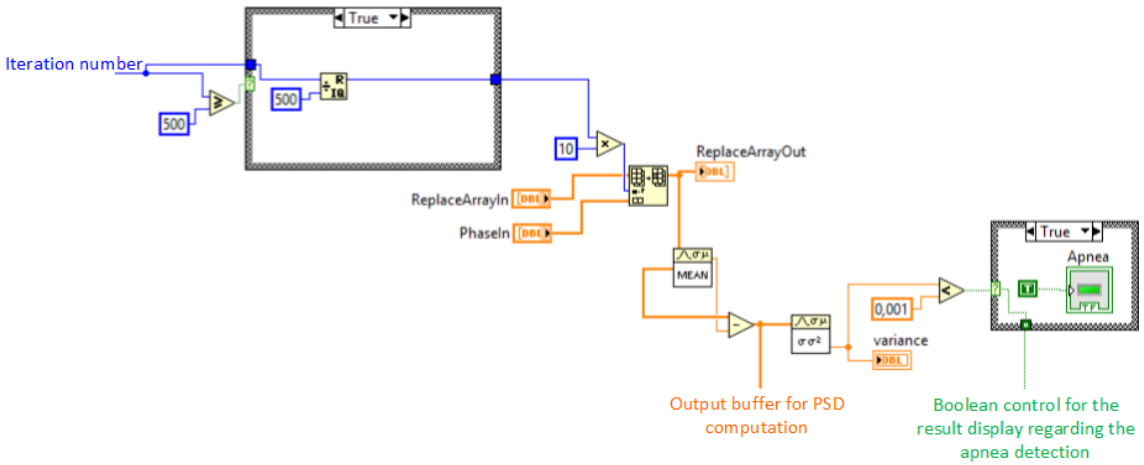

Figure 4.18: Buffer fill and apnea detection (that is going to be explained later).

2 - PSD computation

After the 500^{th} iteration, the PSD can be computed. As mentioned previously, the

prototype in LabVIEW is only for demonstration purposes, so due to the complexity application of the presented algorithm for DC extraction in this software and once the DC offsets are small, signals can be displayed with DC presence and hence the data enters in this block with DC. Thus, before the PSD computation the mean value should be removed, because if otherwise the spectral component present in DC is bigger than the respiratory component, as result the detected peak would be 0 Hz.

For the PSD computation the *FFT Power Spectrum and PSD* VI from LabVIEW is used, with Hanning windowing by default. The array of magnitudes is extracted, which has peaks of the highest spectral components. The peak index is linked to the sampling frequency used at this point, so it goes until $F_s/2 = 500$ Hz. However the spectral component that we want to achieve is really close to DC, so an interpolation will help to increase frequency resolution for a proper spectral detection.

3 - Interpolation for peak detection

In this application an spline interpolation is done using a factor of 5. It could not be bigger due to LabVIEW processing memory problems.

First, an interpolated frequency axis was generated using the *Ramp Pattern* VI, starting in zero frequency until $F_s/2$. Afterwards, the magnitude array is resampled in order to be equally distributed according to the new frequency axis previously created, by using a block available in [41]. Soon after the interpolation, the highest peak is detected and its index is assigned according to the interpolated frequency axis.

Result is displayed in Hz and also in Breaths/min, by multiplying the Hz value by 60 seconds. The spectral peaks are also displayed using a *XY Graph*, where x-axis and y-axis are the interpolated frequency and magnitude arrays previously obtained, respectively.

This method presents some flaws regarding frequency resolution. The minimum detectable frequency is 0.2 Hz (12 bpm) because even using a buffer length equal to 5000 the resolution is not enough. If the person stops breathing the noise increases because there are too disperse samples and no phase modulation, hence the rate changes randomly. This latter issue can be solved by an apnea detecting system, that is discussed in the next section.

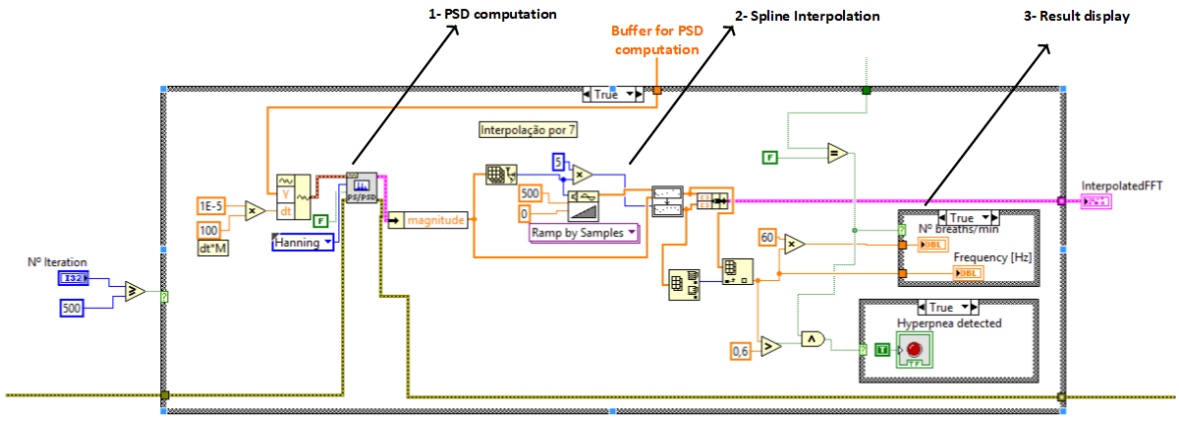

Figure 4.19: PSD computation and hyperpnea detection (described in the next section).

4.4.6 Apnea and Hyperpnea Detecting System

Normal breathing is an automatic and effortless action, with a constant rate and inspiratory volume, [42]. A healthy adult breaths with a respiratory rate of 12/20 Breaths/min, [43]. Although, abnormalities may occur in rate, rhythm, and in the effort of breathing [42]. In clinical context, apnea term defines the absence of breathing and hyperpnea consists in an increase respiration depth and frequency.

The rate estimation algorithm encompasses also apnea and hyperpnea detector. In this section, its implementation is described.

Apnea detecting system

If the subject stops breathing, only noise artefacts will be received. The phase value does not change over time and its variance is very low and tends to a constant value. By evaluating the variance of the buffer, a threshold is defined. If the variance is lower than 0.001, apnea is detected and a squared green led is lighten up. At this point, if only noise is acquired it will be perceived in several frequency components due to the dispersed data and different peaks would be detected. So a condition must be defined: if the apnea is detected, hyperpnea is not and the rate result is not displayed.

The implementation of the apnea detector is shown in Figure 4.18.

Hyperpnea detecting system

The breathing rate of a normal person is between 12 and 20 Breaths/min as mentioned previously. Giving offsets margins to these values, an *if condition* is set inside the *Peak ++* subVI. If the respiratory rate passes 36 Breaths/min, a hyperpnea case is detected and a red led is lighted in the front panel.

The implementation of the hyperpnea detector is shown in Figure 4.19.

4.5 Chest-Wall Simulator

During the prototype implementation in LabVIEW, several tests were needed to validate its proper operation and accuracy, specially during the implementation of the respiratory rate computation, as well as the implementation of DSP techniques for DC offset cancellation and rate computation in MATLAB. In this context a CWS was built to help in this task.

The CWS replaces the human chest-wall in the diagram of Figure 4.2. This simulator is a mechanical platform that is pushed and pulled horizontally with a known motion rate which is, in this case, 0.4 Hz. To build this simulator was used a stepper motor, controlled by the Easydriver version 4.4 which controls the steps necessary to rotate the motor. The rotation direction is irrelevant for this application, so it was established as counterclockwise. The number of steps and the time between them is settled by a Arduino Pro Micro microcontroller. Figure 4.20 illustrates the main mechanical operations.

The CWS constitutes a model that can be used for the respiratory motion of the human chest-wall. To prove this point, a subject was asked to synchronize his breathing with metronome beats, in order to get a breathing rate of 24 Breaths/min. Figure 4.22 shows the simulator's motion extracted signal after the DSP algorithm, superimposed with a sample of an extracted respiratory signal forced to be with 0.4 Hz. Note that Figure 4.22a still has DC

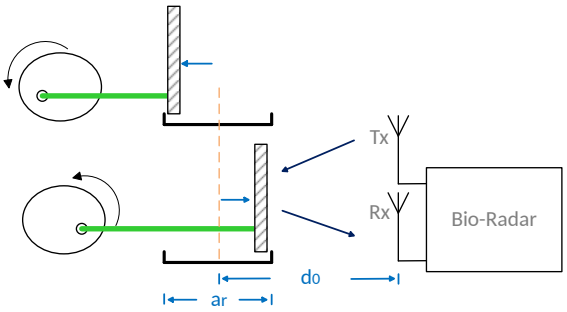

Figure 4.20: Mechanical schematic for the CWS motion.

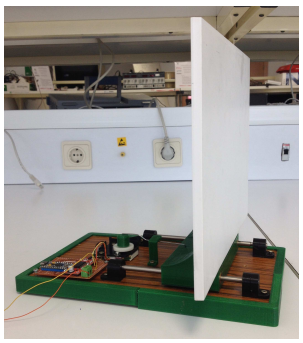

Figure 4.21: Chest-Wall Simulator.

offset in both signals. Both waveforms are similar and could be equally extracted with the same rate of $f1 = 0.3906Hz$. This figure proves that the acquired signal with the CWS is approximately equal to the respiratory one, so this model can be used.

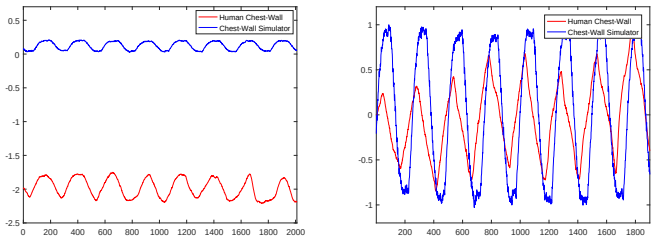

(a) (b)

Figure 4.22: Arctangent result: (a) after downsampling, (b) after DC offsets removal and IQ compensation.

In chapter 5 this simulator serves as model validator. By using the bio-radar prototype developed in this section, signals were acquired regarding the simulator's motion. The DSP algorithm is implemented and the resultant extracted signals reveal that is possible to recover the desired signal with a proper compensation.

4.6 MATLAB DSP Implementation

In the beginning of this chapter, it was defined that regarding the real-time processing requirements, it was not possible to compensate signal non-linearities, hence the recovered signal and its rate's computation can not be accurate enough in LabVIEW. Although it is possible to get an accurate rate extraction apart from the real-time implemented algorithm, once is possible to record data in binary files in LabVIEW and process it further offline using MATLAB.

Figure 4.23a shows the algorithm implemented in MATLAB for signal process, and Figure 4.23b shows the LabVIEW blocks used for signal's recording. Regarding Figure 4.23a, the recorded signal is already in baseband and without the 10kHz offset, so it corresponds to

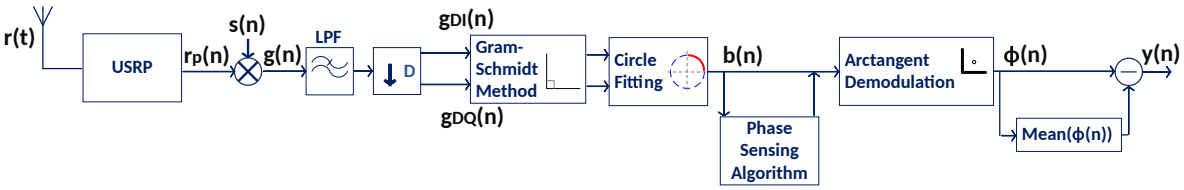

(a)

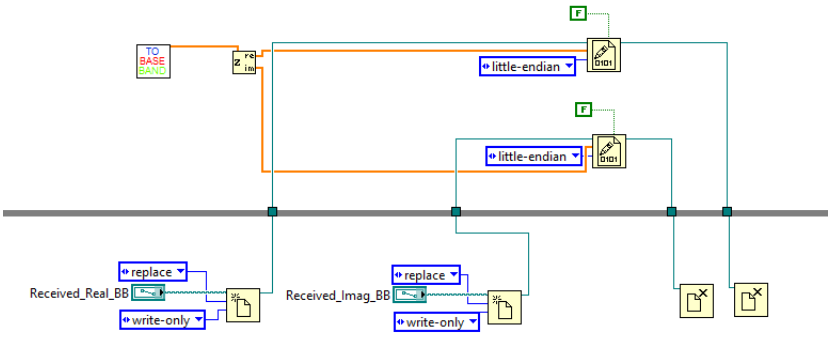

(b)

Figure 4.23: (a) DSP algorithm implemented in MATLAB, (b) LabVIEW blocks for signal recording.

---

signal $g(n)$. The output of '*To Baseband*' block is an array of double complex data, so the recorded signal is separated in two files, one for the real component and the other for the imaginary component.

In MATLAB, the acquired signals are read and the complex signal is formed for further processing. After decimation (using factor M=1000), the Gram-Schmidt method is applied for IQ imbalance compensation and circle fitting is performed in order to cancel the DC offsets.

In order to perform the Gram-Schmidt method the imbalance parameters, A_E and ψ_E must be measured. Quadrature signals are balanced if the quadrature components present the same amplitude and if they are exactly 90° out of phase. This information can be estimated by the superimposed plot of the both quadrature components. A_E is the ratio between the amplitudes from I and Q signals and ψ_E is the difference between the phases of the two quadrature signals minus 90. The imbalanced measured for this case was $A_E = 1.0788$ and $\psi_E = \pi/10$. Finally the signal's rate is computed using the ***pwelch*** function followed by a spline interpolation with the ***interp1*** function, by a factor $L = 10$.

The extracted signals and their discussion are presented in chapter 5.

Chapter 5

Results Discussion

This chapter will focus in the obtained signals using the prototype described in chapter 4 and processed by the DSP algorithm also mentioned. Results are presented according to the following order: first the CWS is used for algorithm validation and also for the system performance evaluation regarding the antennas design and the selected frequency operation. Then real signals are acquired and processed using the developed bio-radar prototype. Then an alternative approach to separate heartbeat and respiratory signal is presented with one successful case. Finally, a comparison is made using these acquired signals and a simultaneously measuring vital signals using the BioPac equipment.

5.1 Bio-radar Model Validation using CWS

In chapter 3 we have proposed a mathematical model for the bio-radar's system and simulated it with artificial signals, also to evaluate the performance of the selected DSP algorithm. In this section, results of the proposed algorithm using a CWS are presented in order to verify the algorithm performance. The CWS has a constant motion rate with a fixed amplitude. Due to that it can be used as comparison basis for this algorithm implementation with real respiratory signals acquired with the same prototype.

Experimental Procedure

For model validation purposes, a few tests were performed with two varying parameters and a total duration of 1 minute. Table 5.1 describes three testing scenarios, where the a_r represents the amplitude of the chest-wall displacement, $d(t)$ and d_0 is the distance between the radar and the target. This distance variation will also change the position of the formed arc in the complex plot. Tests are described as follows:

Test 1 − the CWS was used to analyse the impact of high amplitude variation, centred at d_0 with motion rate of 0.4 Hz;

Test 2 − the CWS was used to analyse the impact of low amplitude variation, centred at d_0 with motion rate of 0.4 Hz;

Test 3 − a subject was asked to synchronize his breathing with metronome clicks. The breathing rate was 24 Breaths/min. This third test is used to compare the signal obtained with the CWS with a real signal.

	a_r [cm]	d_0 [cm]	
Test 1	0.7	56	*Estimated values
Test 2	0.3	66	
Test 3	≈ 0.4*	≈ 70*	

Table 5.1: Parameters for each test. Tests 1 and 2 where performed with the CWS and the test 3 with a human.

Result Discussion

Polar plots before and after IQ imbalance compensation and DC offsets removal, of the performed tests are shown in Figure 5.1. In the three testing scenarios, it was possible to do

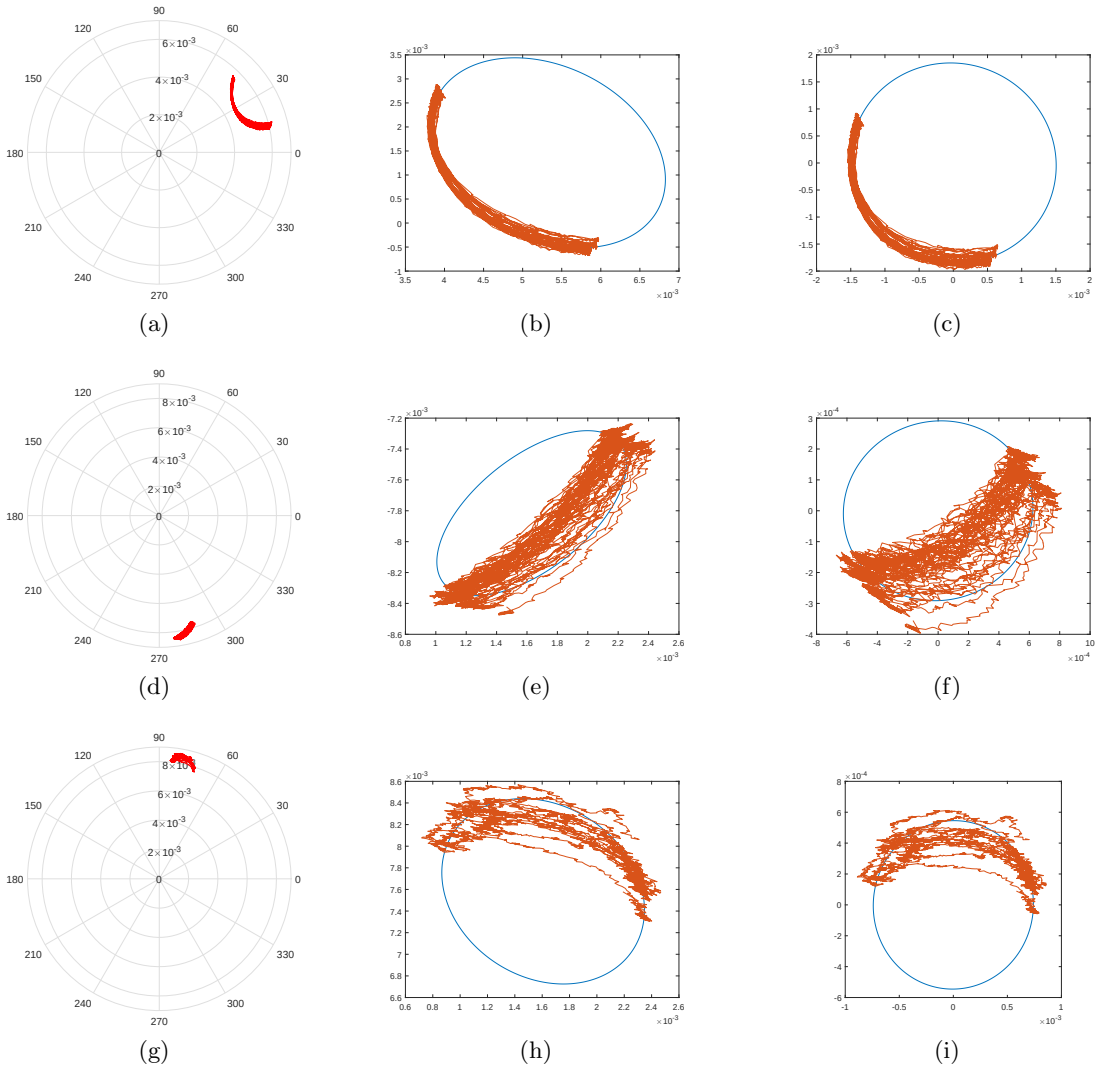

Figure 5.1: Baseband polar plot for test 1, 2 and 3: (a) (d) (g) after downsampling, (b) (e) (h) ellipse fitting for IQ imbalance compensation, (c) (f) (i) circle fitting after DC offsets removal and IQ compensation.

IQ imbalance compensation and DC offset removal successfully. It is possible to verify that for a larger target motion, the ellipse fitting is more precise and the imbalance compensation is more accurate, hence there are better results for the parameter $a_r = 7$mm. It is also possible to conclude that the parameter d_0 does not have any influence in the performance of the implemented algorithm. Analysing the simulator, the major source of noise is the presence of friction while the mechanical platform moves forward and backward. The friction effect is more significant for lower displacement (in test 2 when a_r is 3mm).

Focusing now in test 3, when breathing it is impossible to keep the same breathing rhythm and it is difficult to stay completely stable during the acquisition. Comparing figures 5.1b and 5.1c with figures 5.1h and 5.1i, it can be observed the following effect: the arc drawing is more disperse over the ellipse, in the case of the breathing signal than in the case of the simulator's first test.

As explain previously in chapter 3, section 3.2.3, DC offsets are removed by the subtraction of the arc's centre coordinates. Table 5.2 shows for each test the coordinates values before $(X0, Y0)$ and after $(X1, Y1)$ the DC cancellation.

	$X0$	$Y0$	$X1$	$Y1$
Test 1	0.0053	0.0015	-5.3993e-17	-6.3695e-17
Test 2	0.0016	-0.0078	1.7352e-17	-1.9293e-17
Test 3	0.0016	0.0076	3.4091e-19	-3.9854e-18

Table 5.2: Arc's centre coordinates before and after DC offset cancellation.

Finally, the extracted signal for each test is shown in Figure 5.2, proving that is possible to recover the respiratory signal with the proposed algorithm.

In order to clarify the proximity of the CWS extracted signal to a real breathing signal, was asked a subject to force his respiratory rate, as mentioned previously. Fig.5.2c shows the signals acquired as described in test 1 and test 3, after downsampling and after DC offsets removal. All waveforms are similar and could be equally extracted with the same rate of f1 = 0.3906 Hz.

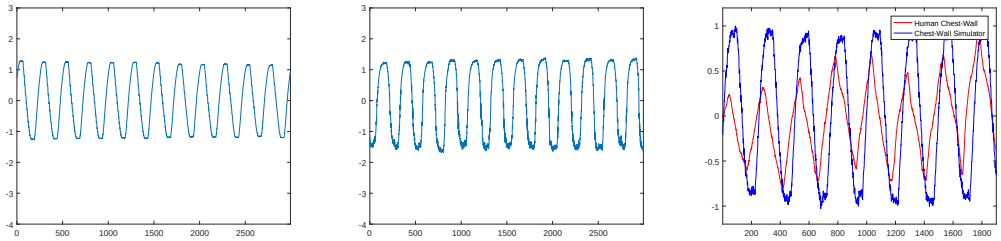

(a) (b) (c)

Figure 5.2: Recovered signal: (a) Test1, (b) Test 2, (c) Test 3.

5.2 Alternative Approach to Separate Heartbeat and Respiratory Signal

In this subsection, the implementation of a method based on TVD method, in MATLAB using recorded signals, is presented. In order to acquire the heartbeat, the gain of both the PA and LNA stages were increased to the value of 30dB. The signal was recorded with the same procedure previously performed to acquire the respiratory signal and was processed in MATLAB using the same functions mentioned in section 4.6.

This experiment aims to extract the heartbeat signal from the respiratory signal without apnea periods, so in this case the respiratory signal is neglected in the rate computation. Before the TVD application and with no DC offset cancellation PSD was computed in order to detect if the heartbeat component is present, as shown in Figure 5.3.

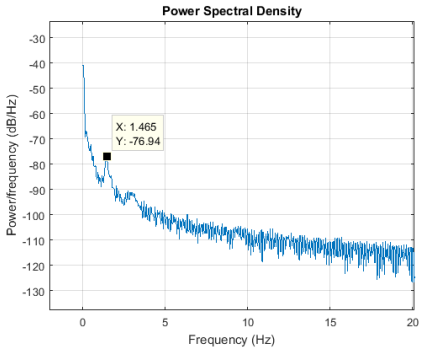

Figure 5.3: PSD of the respiratory signal before the TVD application and DC offset presence.

There are two spectral components that stand out in Figure 5.3: one in DC that comprises the DC offsets and the respiratory spectral component, which was neglected in this experiment, and there is also a peak at 1.465 Hz that corresponds to the heartbeat spectral component. Applying the relation 3.50 from chapter 3, 1.465 Hz corresponds to 87.9 BPM.

Then, the TVD algorithm is applied, where two complementary functions are used: the ***tvdiplmax*** and the ***tvdip*** that returns the denoised output.

The function ***tvdiplmax*** has as input the signal to denoise, $y(n)$ and returns the greater κ value which confines the TVD solution equal to the mean of the input signal. The TVD is applied for several coefficients given by the vector ***lration***. Each coefficient is a fraction of the maximum value given by ***tvdiplmax*** function and produce a different denoised output.

The ***tvdip*** performs discrete TVD using a primal-dual interior-point solver, [44]. This function aims to minimize the function (3.51) over the variable x. In the end of this procedure, the denoised signal x is subtracted by the original signal $y(n)$, resulting in the noise present in $y(n)$. The κ equal to 0.001 was the one that produced the most suitable output. In this case, the noise is the heartbeat signal that is desired to obtain. Figure 5.4 shows the original signal and the heartbeat signal extracted from it. It is possible to observe that the highest peaks of the respiratory signal are still present in the heartbeat extraction (marked by the green points). This occurs because the noise is not uniformly distributed over the respiratory signal, and this method can maintain sharp details. Although, since the heartbeat rate is computed regarding all signal and not over the time continuously, these peaks do not affect the final result of the calculated rate.

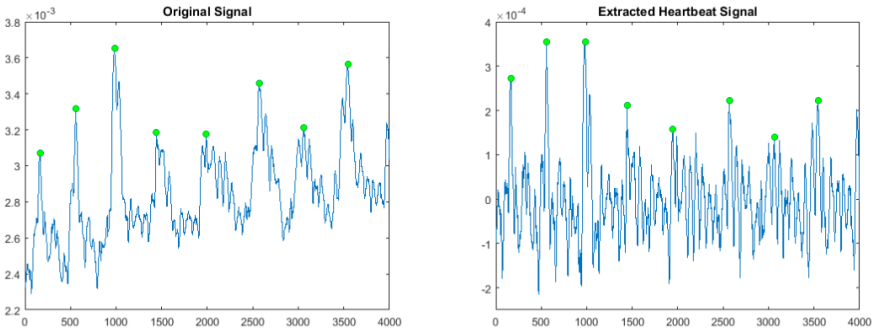

(a) (b)

Figure 5.4: TVDip final result: (a) Original signal before denoising, (b) Heartbeat signal extracted from the original signal.

Finally, the heartbeat rate was computed using ***pwelch*** function (see Figure 5.5) and the highest spectral component was extracted using a spline interpolation with $L = 10$. The detected spectral component was equal to 1.4623 Hz, it means 87.74 BPM. This result reveals a case of success in heartbeat extraction using this method.

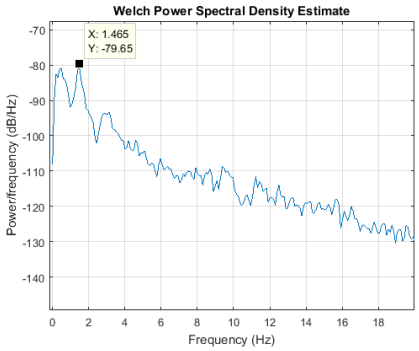

Figure 5.5: PSD of the heartbeat extracted signal after the TVDip application.

Unfortunately, due to the lack of time the validation of this method and algorithm improvements could not be done. Therefore, this technique shows great potential as future work. An algorithm can be developed, in order to compute automatically the best κ and better conditions of the system operation must be defined, such as the amplifier's gain and the best carrier to detect the heartbeat signal with enough resolution, avoiding the respiratory signal's inaccuracy during its recover.

5.3 Impact of Antennas Design

The frequency selection is an important subject as it affects the system performance and influences physical characteristics in the transmitting environment such as antenna size, possible range for target's detection and the resolution (i.e. the amount of phase shift). Also the antenna design is crucial for a good system performance. In this section, a comparison

between two antennas is made, using directive 5.8 GHz antennas (from now on called antenna 1 and these are the ones used in this dissertation) and non-directive 2.5 GHz (from now on called antenna 2).

In chapter 2 advantages in the usage of high carriers frequencies are presented, such as the increasing SNR, the possibility to use more compact and portable radar modules, the full beam radiating properties which can be maintained for longer distances and increase radar cross-section of the vital signals area.

Directive antennas will have a beam more focused in the target, as result the presence of clutter in the received signal is reduced. On the other hand, if non-directive antennas are used the main lobe is wider and the clutter effect will be clearly evident. A vectorial diagram of the received signal for both antenna cases is shown in Figure 5.6.

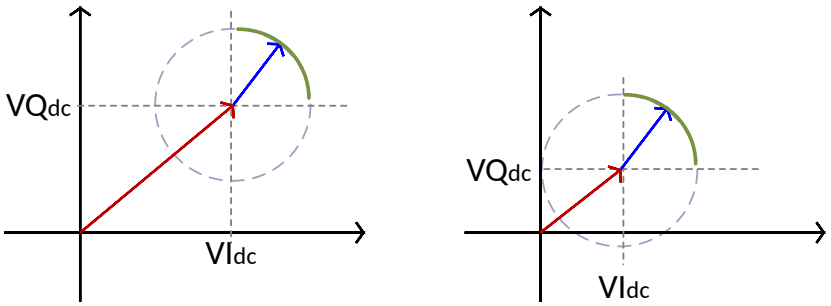

Figure 5.6: Vectorial diagram representing the DC component, where the red arrow represents the DC component and the the blue one represents the signal: (a) In case of non-directive antennas the DC component is higher than in (b) where a directive antenna is being used and there is less clutter influence.

Experimental Procedure

The purpose of this experiment is to compare the system performance with two different antenna types: antenna 1 is 4×4 antenna patch array tunned in an higher frequency, more specifically 5.8 GHz and antenna 2 is a single patch with frequency of operation equal to 2.5 GHz. The antenna radiation pattern shown in Figure 5.7 were simulated in MATLAB regarding their characteristics.

The conducted experiment states as follows: the CWS was used to simulate the chest-wall motion, which is at a frequency of 0.4Hz. For each antenna the CWS's motion was measured twice, at two different nominal distances, for d_0=50 cm and for d_0=70 cm.

For each experiment, the DC component was measured by computing the absolute value of the signal's mean.

Result Discussion

Regarding the radiation patterns in Figure 5.7, antenna 1 focus in a specified area reducing the clutter reception. On the other hand, antenna 2 has a single main lobe with low directionality and therefore more parasitic reflections will be received.

As mentioned previously the clutter is perceived as DC offsets present in both real and imaginary part of the signal. This effect is confirmed by the results of the conducted experiments, presented in table 5.3. The obtained results show that independently of the

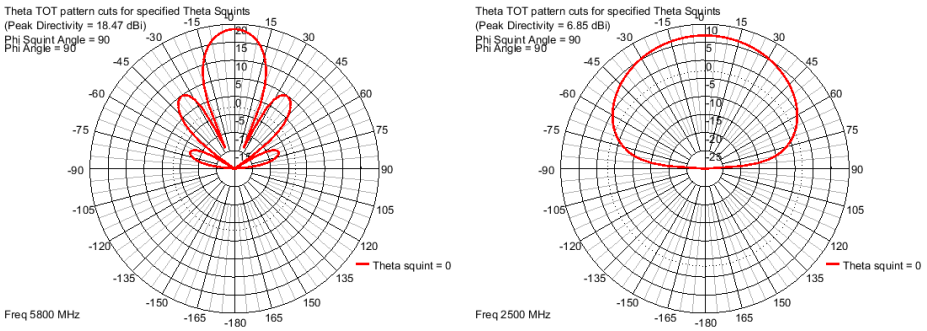

(a) (b)

Figure 5.7: Antenna's radiation pattern for Phi = 0°: (a) antenna 1 presents a gain of 18.47 dBi , (b) antenna 2 presents a gain of 6.85 dBi.

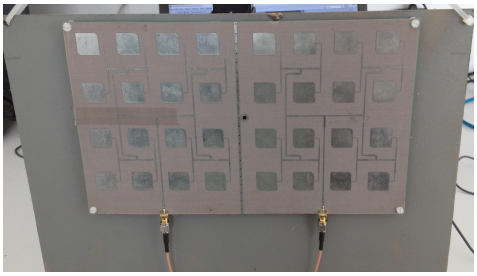

Figure 5.8: Antenna 1.

Figure 5.9: Antenna 2.

	$d_0 = 50$ cm	$d_0 = 70$ cm
antenna 1 - 5.8 GHz	0.0115	0.0044
antenna 2 - 2.5 GHz	0.2330	0.2521

Table 5.3: DC values experimental tests.

target's distance (far or near the antennas) antenna 1 presents lower DC component. In contrast, antenna 2 presents higher DC component at both testing distances.

By implementing the DSP algorithm, the target motion can be extracted in each performed test, as shown in Figure 5.11. The extracted signal for antenna 2 has high presence of noise. On the contrary, antenna 1 signal presents significantly less noise presence showing a more clear arc in the polar plot. Note that the first two periods of extracted signal in Figure 5.11b are due to wraps occurrence, see Figure 5.10. Also the motion's rate was correctly obtained for both cases (Figure 5.12 presents the major spectral component at $f1 = 0.3906$ Hz), regarding

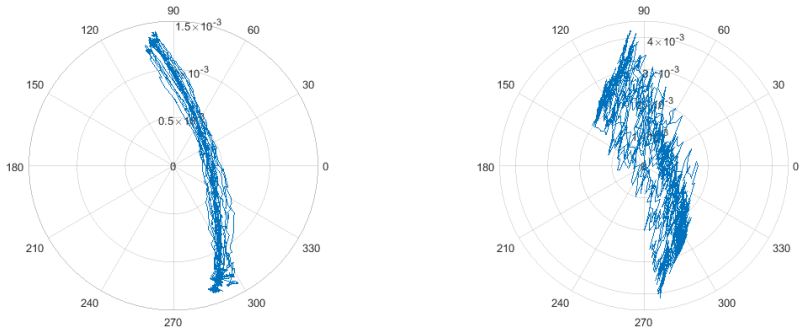

(a) (b)

Figure 5.10: Polar Plot of the extracted signal: (a) for antenna 1 at 5.8 GHz. (b) for antenna 2 at 2.5 GHz.

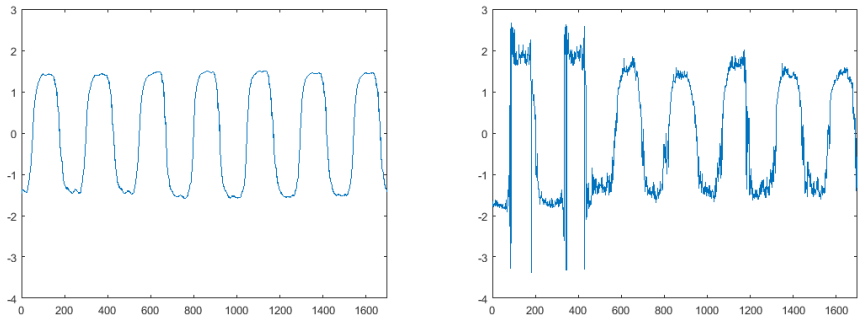

(a) (b)

Figure 5.11: Target's motion extraction at a distance of $d_0 = 50$ cm: (a) for antenna 1. (b) for antenna 2.

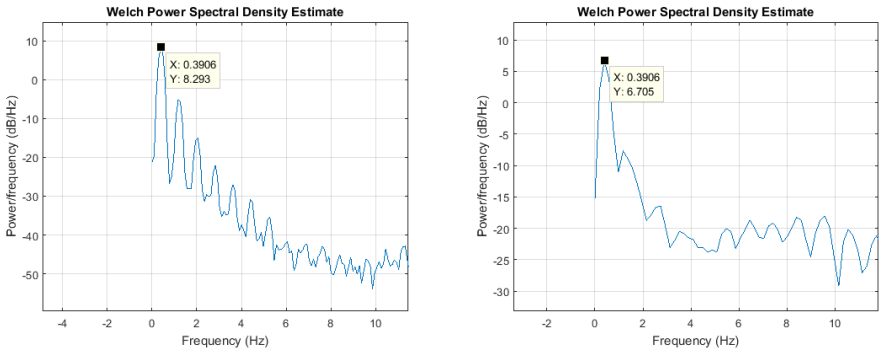

(a) (b)

Figure 5.12: Power spectral density: (a) for antenna 1. (b) for antenna 2.

---

the motion frequency of the CWS, previously mentioned as 0.4Hz.

5.4 Bio-radar Performance Evaluation using BioPac

With the prototype concluded, a validation of its performance was needed. For this purpose a certified measuring equipment (used in the aim of research) called Biopac MP100 was used to monitor vital signals simultaneously with bio-radar.

The Biopac MP100 system is connected to an acquisition board which have several modules for different types of signal acquisition such as ECG, breathing and blood pressure. Once more, the respiratory signal will be used to evaluate the bio-radar performance. The module RSP100C is focused in the processing of data acquired from a respiration transducer chest band, TSD201, placed around the chest cavity of the subject in test. This transducer measures the respiratory effort by analysing the instantaneous thoracic circumference, [2]. The resultant signal is given in Volts. The obtained signal has a mean value, which is dependent on the chest cavity structure of each patient. Thus the obtained value is a variance around this value. The system's set up is shown in Figure 5.13

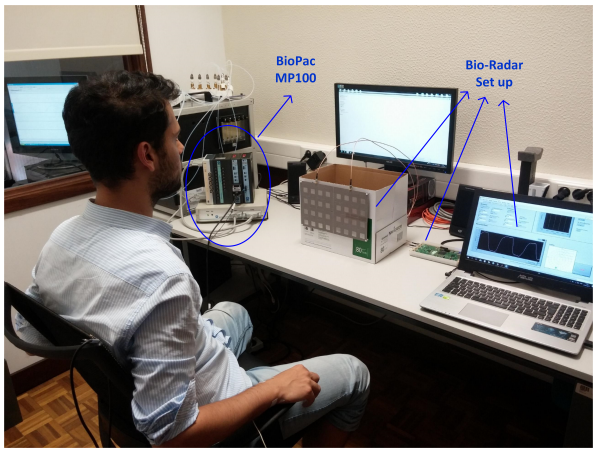

(a)

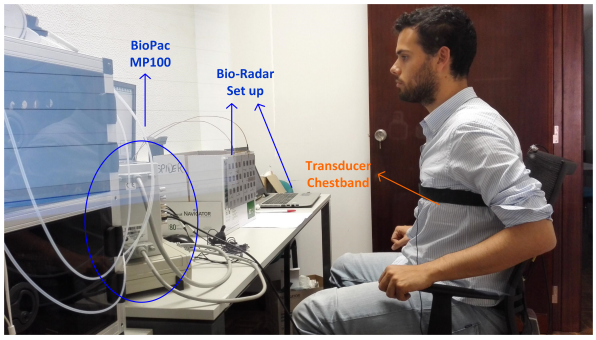

(b)

Figure 5.13: Set up for the conducted tests using BioPac MP100 and bio-radar.

In total, three tests were conducted following the same procedure. The chest band was placed in the subject's chest, which was seated in front of the bio-radar's antennas. The subject was asked to stay still during all the process. The testing procedure starts with an Initial Breathing Pattern (IBP) from the patient, that is composed by three heavy breaths and followed by an apnea period. This pattern is used as trigger to establish the beginning of

the measurement in order to sync signals acquired by BioPac and by bio-radar. Figure 5.14 shows an example of the resultant signal with the IBP and the rest of the measurement. In MATLAB, the acquired samples considered for processing are the ones collected during that measuring time (after the IBP), denominated as 'Normal Breathing' in Figure 5.14.

The results are presented below, where a comparison is made between the extracted signal acquired by the bio-radar and the Biopac measurement (see Figure 5.15) by superimpose acquired signals, and the respiratory rate is computed for each case. Results are summarized in table 5.4. Also the values of the arc's centre coordinates after DC compensation are presented.

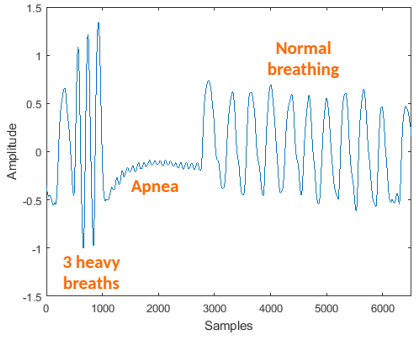

Figure 5.14: Biopac Signal 1 - Respiratory pattern used for the conducted experiment.

In order to achieve a good comparison, the following procedure is done for the different systems:

Biopac: Signals are acquired with $F_s = 2000$Hz, so a decimation with $M = 20$ is made in order to both (biopac and bio-radar) have the same sampling rate $F_{s2} = 100Hz$. Then samples correspondent to the IBP are removed and the obtained signal's mean value is removed. Finally the PSD is computed using the ***pwelch*** function followed by spline interpolation with an interpolation factor $L = 10$.

Bio-Radar: As mentioned previously, signals in bio-radar are acquired with $F_s = 100$kHz, so a decimation with $M = 1000$ is made. Then the rest of the algorithm developed in this dissertation is applied and the PSD is computed using the ***pwelch*** function followed by spline interpolation.

	Rate BioPac [Breaths/min]	Rate Bio-Radar [Breaths/min]	X_{DC}	Y_{DC}
Test 1	17.55	17.55	-4.1021e-18	3.6176e-18
Test 2	18.13	18.13	-2.4369e-17	3.0512e-17
Test 3	14.34	14.93	-1.9019e-18	-6.5228e-18

Table 5.4: Respiratory rate for each test using both BioPac and Bio-Radar, and arc's centre coordinates before and after DC offset cancellation for the bio-radar case.

Comparing now the obtained plotted signals from Figure 5.15, the bio-radar and Biopac signals match almost totally during the proper respiration measurement (after IBP).

BioPac signal presents a periodic signal with a constant trend, although the acquired signal from bio-radar suffers from some distortion effects due its operation principle. For

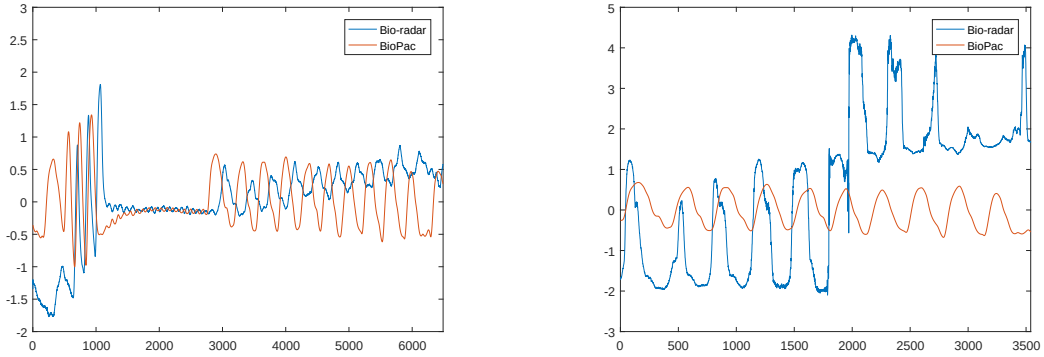

(a)

(b)

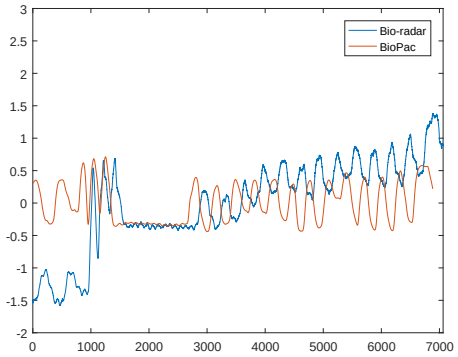

(c)

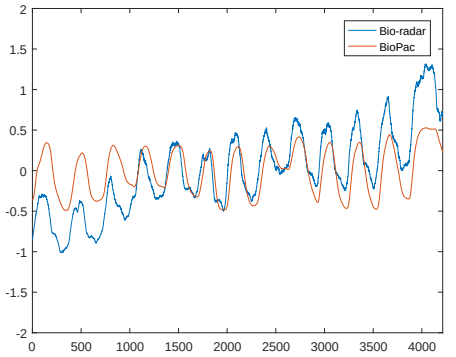

(d)

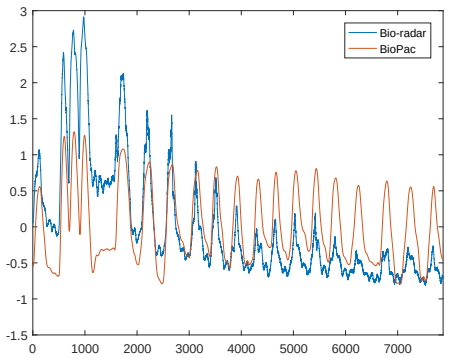

(e)

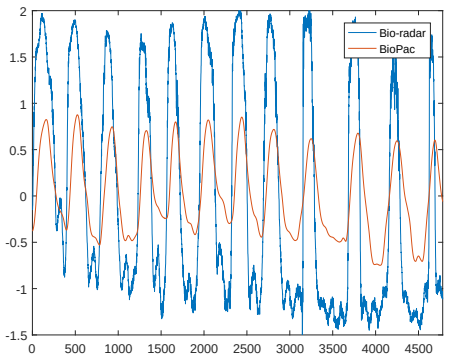

(f)

Figure 5.15: Extracted signal for Test 1, Test 2 and Test 3: (a), (c), (e) Full test, (b), (d), (f) Extracted respiratory signal.

---

example, in Figure 5.15b a wrap occurs near the sample number 2000. This effect happened because after the DC offsets removal, the formed arc crosses always the π value at least one time, regardless the arc's rotation. In this case the ***unwrap*** function from MATLAB was used. Other noticeable effect, can be observed in Figure 5.15d. In this figure, the bio-radar

signal have a slightly varying mean value. This effect appears is normal because the patient do not maintain the same breathing rate and amplitude.

Figures 5.15a, 5.15c and 5.15e represent the obtained signals of the full test, including the IBP. While Figure 5.15c and 5.15e are approximately matched, in Figure 5.15a signals are slightly shifted. This effect occurred because the measurement did not start at the exact same time with both systems. The usage of the IBP allows to solve this problem, by providing a visible trigger and thus, after the apnea period is possible to shift the respiratory signal, so it can start at the same instance as the BioPac one. In this latter figures is also possible to verify the changed trend in the bio-radar signal.

Despite the small effects present in bio-radar signal is possible to verify that its extracted signal match with the Biopac.

Chapter 6

Conclusion and Future Work

6.1 Conclusion

In section 1.2 the objectives that constitute the main goal of this dissertation were presented, regarding the proposed motivation, and they were successfully achieved. The final result of this work is a functional prototype of a bio-radar, capable to acquire and display the respiratory signal in real-time, to compute its rate and display the result continuously during the monitoring time. A basic system of apnea and hyperpnea detection was also implemented regarding the computed rate.

In order to understand the nature of the acquired signals and how they interact with the hardware used for their acquisition and also the surrounding environment influence, a mathematical model was proposed, studied and simulated. Afterwards, having in mind the sources of disturbance present and the state of the art of the applied methods for their compensation, a DSP algorithm for signal recover was proposed and simulated as well.

Due to some limitations faced with LabVIEW, a portion of the DSP algorithm had to be implemented in a non real-time environment, using the bio-radar only to record the bio-signals and MATLAB for signal processing, namely the module that compensate the IQ imbalance and remove DC offsets.

A chest-wall simulator was built for calibration purposes, specially during the implementation of the algorithm for respiratory rate computation in LabVIEW. Due to its uniform and periodic motion, the CWS was also used to validate the DSP algorithm implemented in MATLAB, as previously shown in chapter 5.

A characterization of the developed set-up was done, in order to prove that the selected RF front-end characteristics were the most suitable for bio-radar requirements. Signals were acquired using a different antenna, which was non directive and using a carrier frequency of 2.5 GHz. To compare both signals acquired in different conditions, an experiment was conducted. It was possible to conclude that an antenna with lower directivity acquires more parasitic reflections, increasing the DC offsets and hence more noise. From the used antennas in the final prototype, despite the high value of S_{11} parameter obtained for 5.8 GHz, the radiation pattern was acceptable, once it presents a directive main lobe with an admissible magnitude. With a view to validate the radiation pattern of the used antennas, which were non adapted, a comparison was made with a radiation pattern of the ones adapted at the same carrier frequency. The obtained radiation pattern presented a similar shape as the first one, but with slightly higher magnitude. The parameter S_{11} measures the portion of energy

that is actually radiated toward the target. The system presented acceptable results even with relative low transmitted energy, with non-adapted antennas. If adapted antennas were used instead of the current ones, the transmitted power would be higher and hence stronger captured signals. However, the lack of radiated power does not have influence in the proper function of the system, once the respiratory signal is perceived and the directive main lobe conceives low DC offsets, as expected.

Finally, the bio-radar performance in real-time and its signal acquisition were validated using the Biopac MP100 measuring system. The Biopac kit acquires the respiratory signal using a transducer chest band located around the thorax cavity of the patient. In chapter 5 a presentation of the extracted signals using both acquisition methods is made, as well as a comparison of their computed average rate. By its analysis it is possible to conclude that no significant differences were detected confirming that a good performance of the prototype was achieved.

6.2 Future Work

For the recent decades bio-signals monitoring using non-contact methods have been a field deeply studied. Despite of the technology advance that we are facing nowadays, some challenges remain unsolved. Thus, this section aims to point out some future work that should be improved on these systems and perhaps contribute for its cost effective commercialization.

From all the future work presented in this section is possible to stand out two main challenges:

- For the heartbeat signal's extraction from the respiratory signal;
- The reduction or total elimination of the influence that random motion from the subject can produce in the recovered signal.

Starting by the signal's separation, it would be interesting to perform in real-time, including their rate computation and a detection system of cardiac failures, as the one implemented in this dissertation with the respiratory signal. Also machine learning techniques could be applied in this field, in order to contribute for robust diagnosis of the patient's health condition.

In previous work, signal's separation was accomplished but only if the signals were recorded and then processed separately, using tools like MATLAB or LabVIEW. Some of the proposed solutions implemented filters in MATLAB with different band pass frequencies. In this dissertation, a different method was proposed with acceptable results. By assuming that the heartbeat signal is noise in the respiratory signal, they can be separated using denoising techniques, namely the TVD, which aims to remove unwanted signal components and preserve the important details, simultaneously. Due to the lack of time this solution could not be more developed, and so is presented here as future work.

Focusing now on patient's posture during the measuring procedure, as previously seen, random motions of the subject or even the non uniform respiration pattern can affect the extracted signal and hence the rate computation. A possible solution is the development of a detection system capable to distinguish between bio-signals and random motion of the patient. If abrupt motions are detected, the system suspend its measurement until the patient is immobile again. Usually this type of motions are bigger than the wavelength's carrier, hence

the acquired signals during this period could be used to calibrate the system, more exactly for the imbalance compensation, because a full ellipse can be acquired instead of just an arc.

Further work could be developed in order to improve already existent systems. Reducing the system size could be advantageous. For that, higher frequency is required to reduce the antenna's size, but having in attention that a balance must be made, once higher carrier enables higher resolution, which contributes for the quality of the heartbeat signal, but decreases the efficiency of the breathing signal acquirement.

Still related to higher carriers frequency, is also important to note that it contributes for directivity and hence less clutter presence, but this increases the difficulty of finding an optimal point of detection in the chest and the random motion will have more influence in the acquired signal. A possible solution to overcome this impairment is a beam-forming system that could track the chest-wall, using a directive lobe and thus the random motions would not represent a problem. For the chest-wall tracking, mapping algorithms are required in order to find a reference point in the chest-wall centre.

Other solution for clutter reduction is the usage of one antenna for both Tx and Rx instead for two. Thus we only have one directive lobe, and the same beam transmits and receives data from the same RCS. With two beams, the cross section is different for the Tx and Rx and so the received reflections.

Appendices

Appendix A

Article for 23^{rd} Conference of Pattern Recognition

Bio-Radar Model Validation using Chest-Wall Simulator

Carolina Gouveia [1]
Daniel Malafaia [1]
José Vieira [2]
Pedro Pinho [1]
Ana Tomé [2]
Pedro Magalhães [3]

[1] Instituto de Telecomunicações - 3810-193 Aveiro
[2] IEETA - Campus Universitário de Santiago 3810-193 Aveiro
[3] UA - Departamento de Eletrónica, Telecomunicações e Informática - Campus Universitário de Santiago 3810-193 Aveiro

Abstract

The cardiopulmonary signal monitoring, without the usage of contact electrodes or any type of sensors, has several applications such as elderly's health monitoring, sleeping monitoring or even in search and rescue scenarios. The bio-radar system can measure vital signals accurately by using the Doppler effect principle, that relates the received signal properties with the distance variability between the radar antennas and the person's chest-wall. In this work, a mathematical model of bio-radar is presented. Furthermore it is proposed a fully controllable Chest-Wall Simulator (from now on called CWS) to validate the bio-radar system, as well as the proposed breathing extraction algorithm. Later results comprising simulated and real signals are discussed.

1 Introduction

The bio-radar's system is composed by a continuous wave Doppler radar which continuously transmits a sinusoidal carrier, generated digitally, and receives the echo from the reflecting target. Due to the Doppler effect, there is a phase change as the subject's chest-wall moves towards or away from the radar and hence a phase modulation in the received signal is created [1]. The overall system is represented by the block diagram in Fig.1, where the parasitic reflection $r_1(t)$ from nearby standing objects is also considered. Bio-signals have low amplitude and its bandwidth

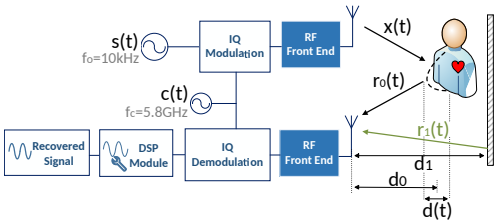

Figure 1: Bio-radar system block diagram.

occupies very low frequency ranges close to DC, hence they are highly sensitive to several sources of noise, such as clutter from the scenario reflections. Therefore, in the next sections the mathematical model that synthesises the bio-radar system behaviour is presented. Also the CWS is described and used to evaluate the bio-radar's system and the real-time DSP algorithm developed for the bio-signals information extraction.

2 Modelling the Bio-Radar system

2.1 Signal model for the Bio-Radar channel response

Regarding the block diagram presented in Fig.1, a RF signal $s(t) = e^{j\omega_0 t}$ is generated digitally, modulated with an in-phase and quadrature (IQ) modulation, with the carrier signal $c(t)$ and transmitted toward the target.

$$x(t) = \cos(\omega_0 + \omega_c)t \tag{1}$$

The received signal is expressed as:

$$\begin{aligned} r(t) &= r_0(t) + r_1(t) = \\ &= A_0\cos((\omega_0+\omega_c)t + \varphi(t)) + A_1\cos((\omega_0+\omega_c)t + \theta_1) \end{aligned} \tag{2}$$

where A_0 and A_1 are the amplitudes of the received signal from the subject and clutter, respectively. The signal $r_1(t)$ represents the sum of the total sources of clutter and its equation in the baseband is $r_1(t) = A_1 e^{j\theta_1} = A_1 e^{(j4\pi d_1/\lambda)}$. The phase change function which contains the respiratory information is represented by $\varphi(t)$. The chest-wall motion changes the wave's travelled distance and hence modulates the reflected signal. Thus, the phase change function can be described by the equation 3:

$$\varphi(t) = \theta_0 + \frac{4\pi d(t)}{\lambda} \tag{3}$$

where $\theta_0 = (4\pi d_o/\lambda) + \phi$ is the total path travelled by the wave, considering the nominal distance between the radar and the target, d_o, and the phase shift at the target's surface, ϕ. In the remain of this work we consider the chest movement described as $d(t) = a_r\cos(2\pi f_1 t)$. For simulation purposes the chosen respiratory rate used was $f_1 = 0.3$Hz.

2.2 Breathing signal's extraction algorithm

The received signal is sampled by the RF front-end and IQ demodulated. This signal is then processed by a DSP algorithm represented by the diagram in Fig.2. The baseband complex signal $g(t)$ is downsampled once it

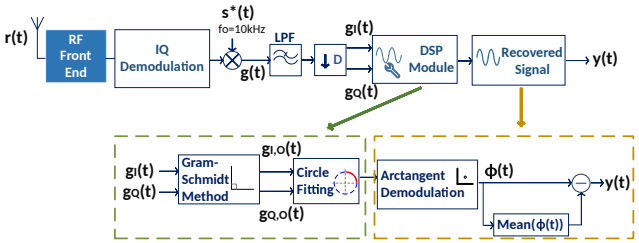

Figure 2: Receiver channel with DSP algorithm implementation.

is a narrowband low-pass signal.
The phase variation due to the target's motion, is represented in the polar plot by an arc (Fig.3(a)), where its length corresponds to the amplitude of the respiratory signal, a_r, and its radius is the received signal's amplitude A_0. In an ideal scenario the arc fits to a perfect circle centred in zero.

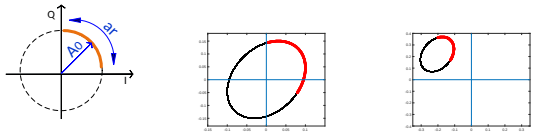

(a) (b) (c)

Figure 3: Complex plot of the baseband signal, $g(t)$, due to target's motion: (a) in an ideal scenario, (b) with IQ imbalance effect, (c) with DC offset and IQ imbalance effect.

However, in real-world scenarios there is IQ imbalance effect, which occurs when both real and imaginary parts do not have the same amplitude and the phase relationship is not exactly 90°. Hence, the formed arc fits to an ellipse instead a circle. There are also DC offsets present in both real and imaginary parts of the baseband signal, caused by the clutter, which leads to an offset in the arc's centre. Fig.3(c) shows the arc formed with the IQ imbalance effect and DC offset presence. These effects should be digitally removed before the phase demodulation in order to guarantee an accurate arctangent result.
The IQ imbalance can be removed by using the Gram-Schmidt method, by applying relation (4), [2], [1], which restores the orthogonality of the baseband signal in quadrature. The parameters ψ_E and A_e are phase and amplitude imbalance measured, respectively.

$$\begin{bmatrix} g_{I,O}(t) \\ g_{Q,O}(t) \end{bmatrix} = \begin{bmatrix} 1 & 0 \\ -\tan(\psi_E) & \frac{1}{A_e\cos(\psi_E)} \end{bmatrix} \begin{bmatrix} g_I(t) \\ g_Q(t) \end{bmatrix} \tag{4}$$

After the imbalance compensation, the DC offsets are estimated and removed using circle fitting method [3], which tracks the circle centre coordinates and subtract them from the complex signal, forcing the arc to be centred in zero. Finally, the arctangent is evaluated in order to extract the respiratory signal [1],[3], obtaining the signal $y(t)$, and its rate is computed using the power spectral density. In the simulation of this mathematical model using simulated signals was possible to recover the respiratory signal with rate of $f_1 = 0.3027$ Hz as expected.

3 Chest-Wall Simulator

The CWS replaces the human chest-wall in the diagram of Fig.1 and was developed in order to validate the mathematical model described previously and to test the DSP algorithm efficiency. This simulator is a mechanical platform that is pushed and pulled horizontally with a known motion rate which is, in this simulation, 0.4 Hz. To build this simulator was used a stepper motor, controlled by the Easydriver version 4.4 which controls the steps necessary to rotate the motor. The number of steps and the time between them is settled by a Arduino Pro Micro microcontroller. Fig.4 illustrates the main mechanical operations.

For model validation purposes, a few tests were preformed with two varying parameters and a total duration of 1 minute. Table 1 describes three testing scenarios, where the a_r represents the amplitude of the chest-wall displacement $d(t)$, and d_0 is the distance between the radar and target that causes different position of the formed arc in the complex plot. The amount of chest-wall displacement in millimetres depends on the subject's body structure and should be between 4 and 12 mm, [2]. Tests are described as follows:

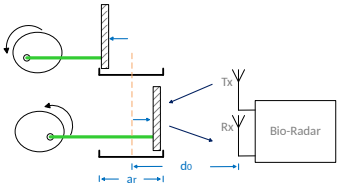

Figure 4: Mechanical schematic for the CWS motion.

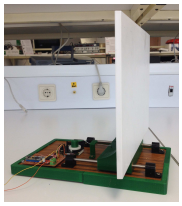

Figure 5: Chest-wall simulator.

Test 1 – the CWS was used to analyse the impact of high amplitude variation, at a certain d_0 and a motion rate of 0.4 Hz;

Test 2 – the CWS was used to analyse the impact of low amplitude variation, at a certain d_0 and a motion rate of 0.4 Hz;

Test 3 – a subject was asked to synchronize his breathing with metronome clicks. The breathing rate was 24 breaths/ minute.

	a_r [cm]	d_0 [cm]
Test 1	0.7	56
Test 2	0.3	66
Test 3	≈ 0.4*	≈ 70*

*Estimated values

Table 1: Parameters for each test. Tests 1 and 2 where performed with the CWS and the test 3 with a human.

4 Experimental Results

In this section, results of the three tests described previously will be shown and discussed. Polar plots before and after IQ imbalance compensation and DC offsets removal, of the performed tests are shown in Fig.6. In all the three testing scenarios, it was possible to do IQ imbalance compensation and DC offset removal successfully. It is possible to verify that for a larger target motion, it is easier to do an ellipse fitting and the imbalance compensation is more accurate, hence there are better results for the parameter $a_r = 7$mm. It is also possible to conclude that the parameter d_0 does not have any influence in the performance of the implemented algorithm. With the simulator, the major source of noise is the presence of friction while the mechanical platform moves forward and backward. The friction effect is more significant for lower displacement (when a_r is 3mm).

Focusing now in test 3, when breathing it is impossible to keep the same breathing rhythm and it is difficult to stay completely stable during the acquisition. Comparing figures 6(b) and 6(c) with figures 6(h) and 6(i), it can be observed the following effect: the arc drawing is more disperse over the ellipse, in the case of the breathing signal than in the case of the simulator's first test.

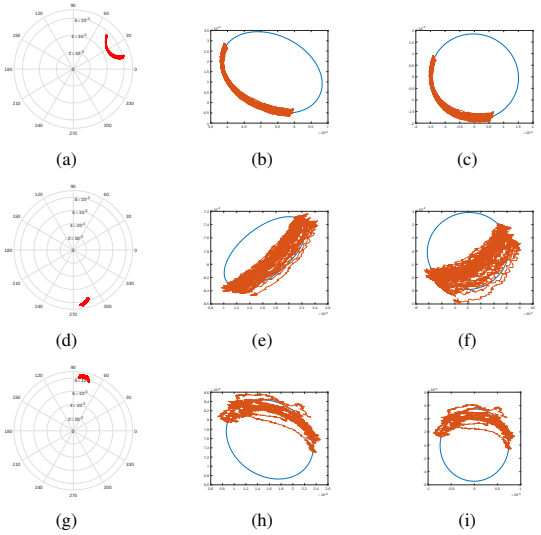

Figure 6: Baseband polar plot for test 1, 2 and 3: (a) (d) (g) after downsampling, (b) (e) (h) ellipse fitting for IQ imbalance compensation, (c) (f) (i) circle fitting after DC offsets removal and IQ compensation.

In order to clarify the proximity of the CWS extracted signal to a real breathing signal, was asked a subject to force his respiratory rate, as mentioned previously. Fig.7 shows the signals acquired as described in test 1 and test 3, after downsampling and after DC offsets removal. Note that figure 7(a) still has DC offset in both signals. Both waveforms are similar and could be equally extracted with the same rate of f1 = 0.3906 Hz.

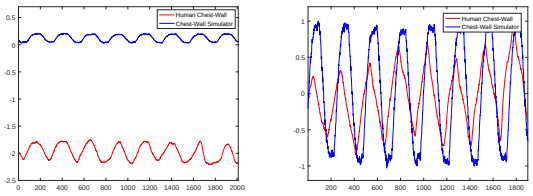

Figure 7: Arctangent result: (a) after downsampling, (b) after DC offsets removal and IQ compensation.

5 Conclusion

In this work a mathematical model of the bio-radar system was introduced. A DSP algorithm for phase demodulation was presented and evaluated using a chest-wall simulator built for this purpose. This simulator was projected to move at a constant rate of 0.4 Hz, in order to validate the results of the extracted respiratory signal. By applying the signals captured with the simulator in the algorithm, it was possible to verify that the algorithm works regardless of the position of the target or its chest-wall motion. The same algorithm was tested using a real acquired respiratory signal and the same conclusions were achieved.

References

[1] Olga Boric-Lubecke, Victor M Lubecke, Amy D Droitcour, Byung-Kwon Park, and Aditya Singh. *Doppler Radar Physiological Sensing*. John Wiley & Sons, 2015.

[2] Amy Diane Droitcour et al. *Non-contact measurement of heart and respiration rates with a single-chip microwave doppler radar*. PhD thesis, Stanford University, 2006.

[3] Byung-Kwon Park, Victor Lubecke, Olga Boric-Lubecke, and Anders Host-Madsen. Center tracking quadrature demodulation for a doppler radar motion detector. In *Microwave Symposium, 2007. IEEE/MTT-S International*, pages 1323–1326. IEEE, 2007.

Appendix B

Poster for 23^{rd} Conference of Pattern Recognition

RECPAD 2017

Bio-Radar Model Validation using Chest-Wall Simulator

Carolina Teixeira de Sousa Gouveia
Daniel Malafaia; José Vieira; Pedro Pinho; Ana Tomé; Pedro Magalhães

Abstract

The cardiopulmonary signal monitoring, without the usage of electrodes or any type of contact sensors, has several applications such as elderly's health monitoring, sleeping monitoring or even in search and rescue scenarios. The bio-radar system can measure vital signals accurately by using the Doppler effect principle, that relates the received signal properties with the distance variability between the radar antennas and the person's chest-wall. In this work, a mathematical model of bio-radar is presented. Furthermore it is proposed a fully controllable Chest-Wall Simulator (from now on called CWS) to validate the bio-radar system, as well as the proposed breathing extraction algorithm. Later results comprising simulated and real signals are discussed.

Radar Principles

The bio-radar's system is composed by a continuous wave Doppler radar which continuously transmits a sinusoidal carrier, generated digitally, and receives the echo from the reflecting target. Due to the Doppler effect, there is a phase change as the subject's chest-wall moves towards or away from the radar and hence a phase modulation in the received signal is created [1]. Bio-signals have low amplitude and its bandwidth occupies very low frequency ranges close to DC, hence they are highly sensitive to several sources of noise, such as clutter from the scenario reflections.

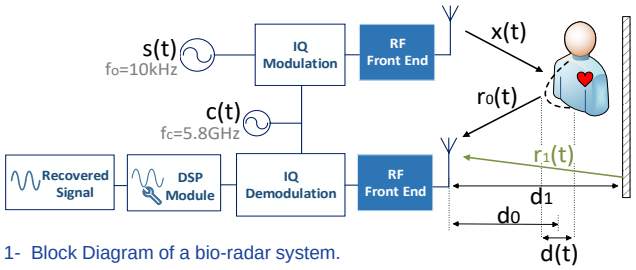

Fig 1- Block Diagram of a bio-radar system.

Regarding the block diagram of the system shown in Fig. 1, a RF signal, $s(t) = e^{jw_o t}$, generated digitally, modulated with an in-phase and quadrature (IQ) modulation, with the carrier signal $c(t)$ and transmitted toward the target.

$$x(t) = \cos((w_o + w_c)t)$$

The received signal is expressed as:

$$r(t) = r_o(t) + r_1(t) =$$
$$= A_o\cos\big((w_o + w_c)t + \varphi(t)\big) + A_1\cos\big((w_o + w_c)t + \theta_1\big)$$

where A_o and A_1 are the amplitudes of the received signal from the subject and clutter, respectively. The signal $r_1(t)$ represents the sum of the total sources of clutter. The phase change function which contains the respiratory information is represented by $\varphi(t)$, and can be described by:

$$\varphi(t) = \theta_0 + \frac{4\pi d(t)}{\lambda}$$

where $\theta_0 = (4\pi\, d_0/\lambda) + \emptyset$ is the total path travelled by the wave, considering the nominal distance between the radar and the target, d_0, and the phase shift at the target's surface, $\emptyset$. The chest movement is described as $d(t)=a_r\cos(2\pi\, f_1 t)$.

Breathing signal's extraction algorithm

The received signal is sampled by the RF front-end and IQ demodulated. This signal is then processed by a DSP algorithm represented by the diagram in Fig.2.

Chest-Wall Simulator

The CWS replaces the human chest-wall in the diagram of Fig.1 and was developed in order to validate the mathematical model described previously and to test the DSP algorithm efficiency. In order to clarify the proximity of the CWS extracted signal to a real breathing signal, was asked a subject to force his respiratory rate, as mentioned previously. Fig. 4 shows the successful operation of the DSP algorithm to compensate the DC offset and the IQ imbalance.

In Fig. 5 we can see the signals acquired with the CWS and person's respiratory signal. Both waveforms are similar and could be equally extracted with the same rate of f1 = 0.3906 Hz.

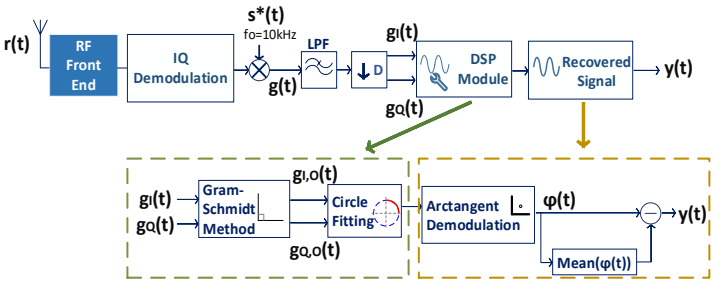

Fig 2 - Block Diagram of the DSP algorithm.

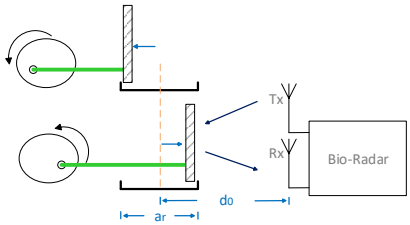

Fig 3 - Mechanical schematic for the CWS motion.

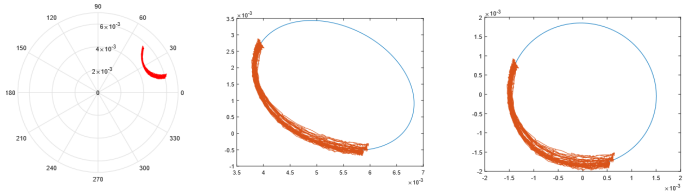

Fig 4 - Baseband polar plot: after downsampling, ellipse fitting for IQ imbalance compensation and circle fitting after DC offsets removal and IQ compensation.

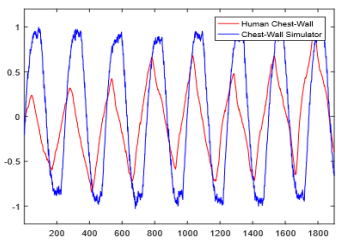

Fig 5 - Two extracted respiration signals, in red from a real person and in blue captured with the CWS.

Conclusion

This CWS was designed to oscillate at a constant rate of 0.4 Hz, in order to validate the results of the extracted respiratory signal. By applying the signals captured with the CWS in the algorithm, it was possible to verify that it successfully extracts the respiration signal, regardless the position of the target or its chest-wall motion. The same algorithm was tested using a real acquired respiratory signal and the same conclusions were achieved.

References

[1] Olga Boric-Lubecke, Victor M Lubecke, Amy D Droitcour, Byung-Kwon Park, and Aditya Singh. Doppler Radar Physiological Sensing. John Wiley & Sons, 2015

instituto de telecomunicações
ieeta instituto de engenharia electrónica e telemática de aveiro
universidade de aveiro theoria poiesis praxis

Appendix C

Poster for 11^{th} Congress of the Portuguese Committee of URSI "New technologies for mobility"

Bio-Radar Performance Evaluation for Different Antenna Design

Carolina Gouveia[1], Daniel Mafalaia [1], José N. Vieira [1,2], and Pedro Pinho [1,3]
[1] IT - Instituto de Telecomunicações, Campus Universitário de Santiago, Aveiro, Portugal
[2] IEETA - Instituto de Engenharia Electrónica e Telemática de Aveiro, Campus Universitário de Santiago, Aveiro, Portugal
[3] ISEL - Instituto Superior de Engenharia de Lisboa, R. Conselheiro Emídio Navarro 1, Lisboa, Portugal
(carolina.gouveia@ua.pt, danielmalafaia@ua.pt, jnvieira@ua.pt, ppinho@deetc.isel.pt)

***Abstract* - The cardiopulmonary monitoring without any physical contact with the human body such as Radar, has several applications such as elderly's health monitoring, sleeping monitoring or even for rescuing people from collapsed buildings. The bio-radar system can measure vital signals accurately by using the Doppler effect principle that relates the received signal properties with the distance change between the radar antennas and the person's chest-wall. In this paper, a mathematical model of the bio-radar is presented, the used algorithm for breath rate extraction is explained and an analysis of the antenna radiation pattern influence on the quality of the received signal is done. Moreover, we show that the antenna with a narrow beam leads to a better signal to noise ratio. The conducted experiment will use a Chest-Wall Simulator (CWS), developed to simulate the human chest-wall motion with a stable frequency, which is in this case 0.4Hz.**

***Key Words* - Radar, SDR, Bio-Signals, Doppler Effect, Antenna radiation patterns**

I. Introduction

The bio-radar's system is composed by a continuous wave Doppler radar which continuously transmits a sinusoidal carrier, generated digitally, and receives the echo from the reflecting target. Due to the Doppler effect, there is a phase change as the subject's chest-wall moves towards or away from the radar and hence a phase modulation in the received signal is created [1]. The overall system is represented by the block diagram in Fig. 1, where the parasitic reflection $r_1(t)$ from nearby standing objects is also considered. Bio-signals

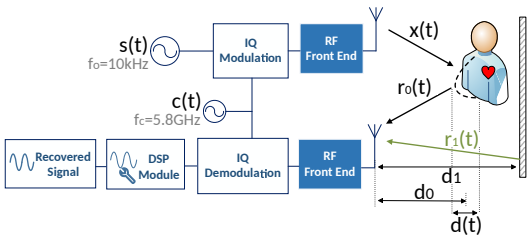

Fig. 1. Bio-radar system block diagram.

have low amplitude and the modulation that they create on the radar transmitted signal will be, in baseband, very close to DC. Hence they are highly sensitive to several sources of noise, such as clutter from the scenario reflections. In this paper a mathematical model that synthesises the bio-radar system behaviour is presented. Once the system is sensitive to parasitic signals that causes noise in the measurement, this effect is greater if the target has small dimensions. Therefore the antenna design should guarantee maximum directivity and narrow beam width, to focus exclusively in the human chest-wall, to avoid the reception of undesired clutter reflections.

In this work, experiments were conducted using two antennas with different designs and different carriers. To prove the impact of their features, the DC component present in the signal was computed for each experiment. Clearly, directive antennas with higher carrier presented best results, as we will see further.

This paper is organised as follow, In the next section we will start by present a mathematical model for the bio-radar system, then on the subsection 2B we have a description of the breathing signal extraction. Then on section 3 we present the implementation of the system and some real measurements obtained SDR based test bed and finally the main conclusions are presented.

II. Modelling the Bio-Radar System

A. Signal model for the Bio-Radar channel response

Regarding the block diagram presented in Fig.1, a base band signal $s(t) = e^{j\omega_0 t}$ is generated digitally, modulated with an in-phase and quadrature (IQ) modulation, with the carrier signal $c(t)$, leading to the signal

$$x(t) = \cos(\omega_0 + \omega_c)t \tag{1}$$

that is transmitted towards the target. The received signal is expressed as:

$$\begin{aligned} r(t) &= r_0(t) + r_1(t) = \\ &= A_0 \cos((\omega_0 + \omega_c)t + \varphi(t)) + A_1 \cos((\omega_0 + \omega_c)t + \theta_1) \end{aligned} \tag{2}$$

where A_0 and A_1 are the amplitudes of the received signal from the subject and clutter, respectively. The signal $r_1(t)$ represents the sum of the total sources of clutter and its equation in the baseband is $r_1(t) = A_1 e^{j\theta_1} = A_1 e^{(j4\pi d_1/\lambda)}$. The phase change function which contains the respiratory information is represented by $\varphi(t)$. The chest-wall motion changes the wave's travelled distance and hence modulates the reflected signal. Thus, the phase change function can be described by the equation 3:

$$\varphi(t) = \theta_0 + \frac{4\pi d(t)}{\lambda} \tag{3}$$

where $\theta_0 = (4\pi d_o/\lambda) + \phi$ is the total path travelled by the wave, considering the nominal distance between the radar and

the target, d_o, and the phase shift at the target's surface, ϕ. In the remain of this work we consider the chest movement described as $d(t) = a_r \cos(2\pi f_1 t)$, where a_r is the amplitude of the chest movement and f_1 is the breathing rate.

B. Breathing signal's extraction algorithm

The received signal is sampled by the RF front-end and IQ demodulated. This signal is then processed by a DSP algorithm represented by the diagram in Fig. 2. The baseband complex

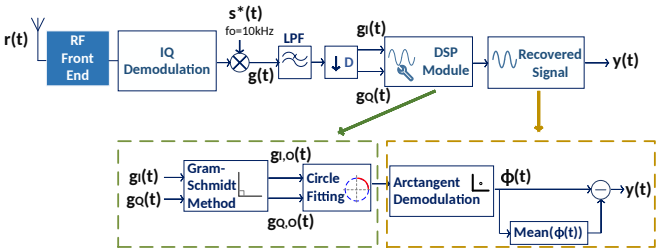

Fig. 2. Receiver channel with DSP algorithm implementation.

signal $g(t)$ is downsampled once it is a narrowband low-pass signal.

The phase variation due to the target's motion, is represented in the polar plot by an arc (Fig. 3(a)), where its length corresponds to the amplitude of the respiratory signal a_r, and its radius is the received signal's amplitude A_0. In an

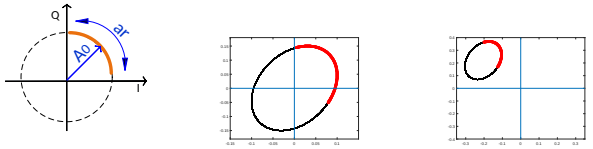

(a) (b) (c)

Fig. 3. Complex plot of the baseband signal, $g(t)$, due to target's motion: (a) in an ideal scenario, (b) with IQ imbalance effect, (c) with DC offset and IQ imbalance effect.

ideal scenario the arc fits to a perfect circle centred in zero. However, in real-world scenarios there is IQ imbalance effect, which occurs when both real and imaginary parts do not have the same amplitude and the phase relationship is not exactly 90°. Hence, the formed arc fits to an ellipse instead a circle. There are also DC offsets present in both real and imaginary parts of the baseband signal, caused by the clutter, which leads to an offset in the arc's centre. Fig. 3(c) shows the arc formed with the IQ imbalance effect and the DC offset. These effects should be digitally removed before the phase demodulation in order to guarantee an accurate arctangent result.

The IQ imbalance can be removed by using the Gram-Schmidt method, by applying relation (4), [2], [1], which restores the orthogonality of the baseband signal in quadrature. The parameters ψ_E and A_e are phase and amplitude imbalance measured, respectively.

$$\begin{bmatrix} g_{I,O}(t) \\ g_{Q,O}(t) \end{bmatrix} = \begin{bmatrix} 1 & 0 \\ -\tan(\psi_E) & \frac{1}{A_e \cos(\psi_E)} \end{bmatrix} \begin{bmatrix} g_I(t) \\ g_Q(t) \end{bmatrix} \quad (4)$$

After the imbalance compensation, the DC offsets are estimated and removed using circle fitting method [3], which tracks the circle centre coordinates and subtract them from the complex signal, forcing the arc to be centred in zero. Finally, the arctangent is evaluated in order to extract the respiratory signal [1],[3], obtaining the signal $y(t)$, and its rate is computed using the power spectral density.

C. Carrier wavelength impact

The impact of the wavelength was simulated in MATLAB and is shown in Fig. 4. Different carrier values were used revealing differences in the arc length. In [4], they conclude

(a) (b) (c)

Fig. 4. Influence of the carrier's wavelength, considering motion's amplitude $a_r = 0.00325$: (a) $f_c = 5.8$ GHz, (b) $f_c = 2.5$ GHz, (c) $f_c = 10$ GHz

that due to the amount of phase modulation, defined in radians as equation 5, the signal-to-noise ratio (SNR) is dependent on the wavelength carrier and hence lower carriers lead to low SNR and vice-versa.

$$\Delta\phi = \frac{4\pi\varphi(t)}{\lambda} \quad (5)$$

Beside the increasing SNR, other advantages in the usage of high frequencies are identified, for instance the possibility to use more compact and portable radar modules, because smaller size antennas can produce same gain and directivity using higher frequencies. High frequencies also maintain full beam radiating properties for longer distances and increase radar cross-section of the vital signals area [5].

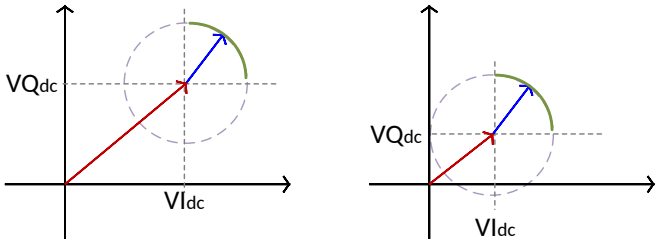

Fig. 5. Vectorial diagram representing the DC component, where the red arrow represents the DC component and the the blue one represents the signal: (a) In case of non-directive antennas the DC component is bigger than in (b) where a directive antenna is being used and there is less clutter influence.

III. Implementation

In this work a bio-radar prototype was developed which consists in a real-time measure system implemented in the LabVIEW software. Signals are acquired using two antennas one for transmission and the other for reception and the front-end based in software defined radio system (SDR) that is a reconfigurable platform which establish the connection of the front-end hardware and the DSP software. With this platform is possible to configure digitally its input and output (receiver

and transmitter), regarding their frequency and sampling rates coverage, [6]. In the framework of this application, the SDR used is an USRP B210. It does the modulation and demodulation of the RF signals digitally, giving more flexibility on the DSP side. The purpose of this work is to compare the system

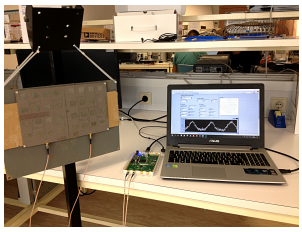

Fig. 6. Bio-radar prototype using 5.8 GHz antennas

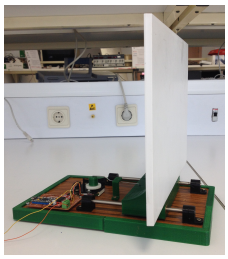

Fig. 7. Chest-Wall Simulator

performance with two different types of antennas: antenna 1 is 4×4 antenna patch array tunned in an higher frequency, more specifically 5.8 GHz and antenna 2 is single patch with frequency of operation equal to 2.5 GHz, see Fig. 6 and Fig. 7 .The antenna radiation pattern are shown in Fig. 8.

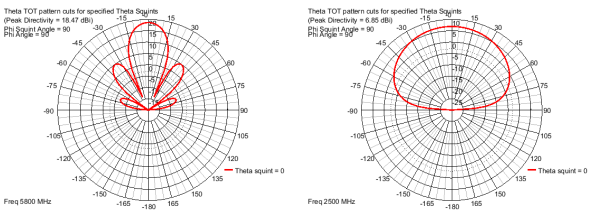

(a) (b)

Fig. 8. Antenna's radiation pattern for Phi = 0°: (a) antenna 1 presents a gain of 18.47 dBi , (b) antenna 2 presents a gain of 6.85 dBi

The conducted experiment states as follows: the CWS (Fig. 7) was used to simulate the chest wall motion, which is at a frequency of 0.4Hz. For each antenna the CWS's motion was measured twice, at two different nominal distances, for d_0=50 cm and for d_0=70 cm.

For each experiment, the DC component was measured by computing the absolute value of the signal's mean. The obtained values are discussed in the next section.

IV. Results Discussion

Regarding the radiation patterns in Fig. 8, antenna 1 focus in a specified area reducing the clutter reception. On the other hand, antenna 2 has a single main lobe with low directionality and therefore more parasitic reflections will be received.

As mentioned previously the clutter is perceived as DC offsets present in both real and imaginary part of the signal. This effect is confirmed by the results of the conducted experiments, presented in table I. The obtained results show that independently of the target's distance (far or near the antennas) antenna 1 presents lower DC component. In contrast, antenna 2 presents higher DC component at both testing distances.

TABLE I
DC values experimental tests

	$d_0 = 50$ cm	$d_0 = 70$ cm
antenna 1 - 5.8 GHz	0.0115	0.0044
antenna 2 - 2.5 GHz	0.2330	0.2521

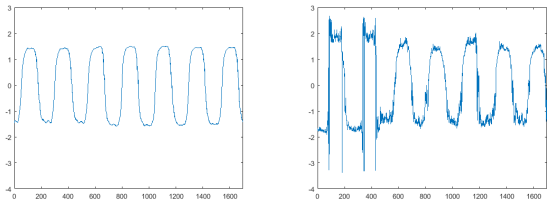

(a) (b)

Fig. 9. Target's motion extraction at a distance of $d_0 = 50$ cm: (a) for antenna 1. (b) for antenna 2.

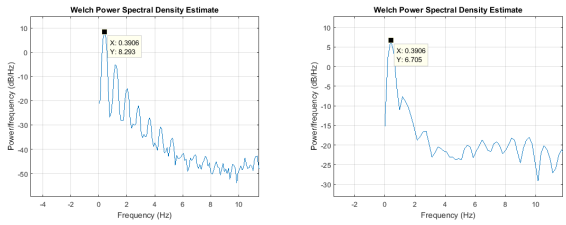

(a) (b)

Fig. 10. Power spectral density: (a) for antenna 1. (b) for antenna 2.

By implementing the DSP algorithm present in section II-B, the target motion can be extracted in each performed test, as shown in Fig. 9. The extracted signal for antenna 2 has high presence of noise. On the contrary, antenna 1 signal presents significantly less noise presence. Also the motion's rate was correctly obtained for both cases (Figure 10 presents the major spectral component at $f1 = 0.3906$ Hz), regarding the motion frequency of the CWS, previously mentioned as 0.4Hz.

V. Conclusion

In this work a mathematical model of the bio-radar system was introduced, as well as the DSP algorithm needed for phase demodulation and respiratory signal extraction. The impact of antennas design and its carrier frequency are also studied. Experimental tests using a Chest-Wall simulator show that directive antennas acquire better signals with small DC components and therefore less noise in the signal. However,

the narrow beam of the the antenna 2 imply a better alignment between the antenna and the patient. As a future work we intend to design a beamforming antenna with a tracking algorithm to maintain the alignment.

REFERENCES

[1] Boric-Lubecke, Olga, et al. Doppler Radar Physiological Sensing. John Wiley & Sons, 2015.

[2] Droitcour, Amy Diane. Non-contact measurement of heart and respiration rates with a single-chip microwave doppler radar. Diss. Stanford University, 2006.

[3] Park, Byung-Kwon, et al. "Center tracking quadrature demodulation for a Doppler radar motion detector." Microwave Symposium, 2007. IEEE/MTT-S International. IEEE, 2007.

[4] Zakrzewski, Mari, Harri Raittinen, and Jukka Vanhala. "Comparison of center estimation algorithms for heart and respiration monitoring with microwave Doppler radar." IEEE Sensors Journal 12.3 (2012): 627-634.

[5] Li, Changzhi, et al. "A review on recent advances in Doppler radar sensors for noncontact healthcare monitoring." IEEE Transactions on microwave theory and techniques 61.5 (2013): 2046-2060.

[6] Malafaia, Daniel, José Vieira, and Ana Tomé. "Improving Performance of Bio-radars for Remote Heartbeat and Breathing Detection by using Cyclostationary Features." Proceedings of the International Joint Conference on Biomedical Engineering Systems and Technologies-Volume 4. SCITEPRESS-Science and Technology Publications, Lda, 2015.

Bibliography

[1] C. Li, V. M. Lubecke, O. Boric-Lubecke, and J. Lin, "A review on recent advances in doppler radar sensors for noncontact healthcare monitoring", *Ieee transactions on microwave theory and techniques*, vol. 61, no. 5, pp. 2046–2060, 2013.

[2] D. Malafaia, B. Oliveira, P. Ferreira, T. Varum, J. Vieira, and A. Tomé, "Cognitive bio-radar: The natural evolution of bio-signals measurement", *Journal of medical systems*, vol. 40, no. 10, p. 219, 2016.

[3] A. D. Droitcour *et al.*, "Non-contact measurement of heart and respiration rates with a single-chip microwave doppler radar", PhD thesis, Stanford University, 2006.

[4] O. Boric-Lubecke, V. M. Lubecke, A. D. Droitcour, B.-K. Park, and A. Singh, *Doppler Radar Physiological Sensing*. John Wiley & Sons, 2015.

[5] Ø. Aardal, "Radar monitoring of heartbeats and respiration", PhD thesis, 2013.

[6] I. S. Merrill *et al.*, *Introduction to radar systems*. Mc Grow-Hill, 2001.

[7] A. Kumar, "Experimental study of through-wall human being detection using ultra-wideband radar", 2011.

[8] W. J. S. Silva, "Software Defined Radar for Medical Imaging", 2016.

[9] `https://www.medbullets.com/step1-respiratory/17007/muscles-of-respiration`, Accessed: 2017.

[10] A. Aubert, L Welkenhuysen, J Montald, L De Wolf, H Geivers, J Minten, H. Kesteloot, and H Geest, "Laser method for recording displacement of the heart and chest wall", *Journal of biomedical engineering*, vol. 6, no. 2, pp. 134–140, 1984.

[11] A. D. Droitcour, O. Boric-Lubecke, V. M. Lubecke, J. Lin, and G. T. Kovacs, "Range correlation and I/Q performance benefits in single-chip silicon Doppler radars for noncontact cardiopulmonary monitoring", *Ieee transactions on microwave theory and techniques*, vol. 52, no. 3, pp. 838–848, 2004.

[12] M. Zakrzewski, H. Raittinen, and J. Vanhala, "Comparison of center estimation algorithms for heart and respiration monitoring with microwave doppler radar", *Ieee sensors journal*, vol. 12, no. 3, pp. 627–634, 2012.

[13] B.-K. Park, O. Boric-Lubecke, and V. M. Lubecke, "Arctangent demodulation with dc offset compensation in quadrature doppler radar receiver systems", *Ieee transactions on microwave theory and techniques*, vol. 55, no. 5, pp. 1073–1079, 2007.

[14] J. C. Lin, "Noninvasive microwave measurement of respiration", *Proceedings of the ieee*, vol. 63, no. 10, pp. 1530–1530, 1975.

[15] J. C. Lin, E. Dawe, and J. Majcherek, "A noninvasive microwave apnea detector", in *Proceedings of the san diego biomedical symposium*, San Diego Biomedical Symposium., vol. 16, 1977, p. 441.

[16] J. C. Lin, J. Kiernicki, M. Kiernicki, and P. B. Wollschlaeger, "Microwave apexcardiography", *Ieee transactions on microwave theory and techniques*, vol. 27, no. 6, pp. 618–620, 1979.

[17] B.-K. Park, V. Lubecke, O. Boric-Lubecke, and A. Host-Madsen, "Center tracking quadrature demodulation for a doppler radar motion detector", in *Microwave symposium, 2007. ieee/mtt-s international*, IEEE, 2007, pp. 1323–1326.

[18] B.-K. Park, A. Vergara, O. Boric-Lubecke, V. M. Lubecke, and A. Høst-Madsen, "Quadrature demodulation with dc cancellation for a doppler radar motion detector", *Ieee mtt transactions*, 2007.

[19] X. Gao, A. Singh, E. Yavari, V. Lubecke, and O. Boric-Lubecke, "Non-contact displacement estimation using doppler radar", in *Engineering in medicine and biology society (embc), 2012 annual international conference of the ieee*, IEEE, 2012, pp. 1602–1605.

[20] A. D. Droitcour, O. Boric-Lubecke, V. M. Lubecke, and J. Lin, "0.25-um CMOS and BiCMOS single-chip direct-conversion Doppler radars for remote sensing of vital signs", in *Solid-state circuits conference, 2002. digest of technical papers. isscc. 2002 ieee international*, IEEE, vol. 1, 2002, pp. 348–349.

[21] A. Droitcour, V. Lubecke, J. Lin, and O. Boric-Lubecke, "A microwave radio for Doppler radar sensing of vital signs", in *Microwave symposium digest, 2001 ieee mtt-s international*, IEEE, vol. 1, 2001, pp. 175–178.

[22] C. Li, Y. Xiao, and J. Lin, "A 5GHz Double-Sideband Radar Sensor Chip in 0.18-um CMOS for Non-Contact Vital Sign Detection", *Ieee microwave and wireless components letters*, vol. 18, no. 7, pp. 494–496, 2008.

[23] C. Li, X. Yu, C.-M. Lee, D. Li, L. Ran, and J. Lin, "High-Sensitivity Software-Configurable 5.8-GHz Radar Sensor Receiver Chip in 0.13-um CMOS for Noncontact Vital Sign Detection", *Ieee transactions on microwave theory and techniques*, vol. 58, no. 5, pp. 1410–1419, 2010.

[24] J.-S. Kim, M. S. Rahman, B.-J. Jang, K.-D. Kim, and B.-Y. Kim, "DSP embeded hardware for non-contact bio-radar heart and respiration rate monitoring system", in *Biomedical information engineering, 2009. fbie 2009. international conference on future*, IEEE, 2009, pp. 560–563.

[25] G. Sun and T. Matsui, "Rapid and stable measurement of respiratory rate from doppler radar signals using time domain autocorrelation model", in *Engineering in medicine and biology society (embc), 2015 37th annual international conference of the ieee*, IEEE, 2015, pp. 5985–5988.

[26] D. Malafaia, J. Vieira, and A. Tomé, "Improving Performance of Bio-radars for Remote Heartbeat and Breathing Detection by using Cyclostationary Features", in *Proceedings of the international joint conference on biomedical engineering systems and technologies-volume 4*, SCITEPRESS-Science and Technology Publications, Lda, 2015, pp. 344–349.

[27] H. Phan, S.-L. Tan, I. Mcloughlin, and L. Vu, "A Unified Framework for GPS Code and Carrier-Phase Multipath Mitigation Using Support Vector Regression", vol. 2013, Mar. 2013.

[28] S. Guan, J. A. Rice, C. Li, and C. Gu, "Automated DC offset calibration strategy for structural health monitoring based on portable CW radar sensor", *Ieee transactions on instrumentation and measurement*, vol. 63, no. 12, pp. 3111–3118, 2014.

[29] X. Gao, J. Xu, A. Rahman, V. Lubecke, and O. Boric-Lubecke, "Arc Shifting Method for Small Displacement Measurement with Quadrature CW Doppler Radar", 2017.

[30] X. Gao and O. Boric-Lubecke, "Radius Correction Technique for Doppler Radar Noncontact Periodic Displacement Measurement", *Ieee transactions on microwave theory and techniques*, vol. 65, no. 2, pp. 621–631, 2017, ISSN: 0018-9480. DOI: 10.1109/TMTT.2016.2625796.

[31] O. Gal, *Ellipse Fit using Least Squares criterion*, `http://it.mathworks.com/matlabcentral/fileexchange/3215-fit-ellipse`, Accessed: 2017.

[32] M. Gdeisat and F. Lilley, "One-dimensional phase unwrapping problem", *Signal*, vol. 4, p. 6, 2012.

[33] S. Haykin, *Communication systems*. John Wiley & Sons, 2001.

[34] J. G. Proakis and D. G. Manolakis, *Digital signal processing 3 rd edition*, 1996.

[35] W. Jianqi, Z. Chongxun, L. Guohua, and J. Xijing, "A new method for identifying the life parameters via radar", *Eurasip journal on applied signal processing*, vol. 2007, no. 1, pp. 16–16, 2007.

[36] I. Selesnick, "Total variation denoising (an MM algorithm)", *Connexions*, 2012.

[37] A. N.I. C. Ettus Research, *USRP B210 (Board Only)*, `https://www.ettus.com/product/details/UB210-KIT`, Accessed: 2017.

[38] T. Yagi, H. Shiomi, and Y. Okamura, "Phase control experiment of the pll oscillator for a phased array antenna", in *Microwave workshop series on innovative wireless power transmission: Technologies, systems, and applications (imws), 2012 ieee mtt-s international*, IEEE, 2012, pp. 167–170.

[39] A. N.I. C. Ettus Research, *UHD application note*, `https://www.ettus.com/content/files/kb/application_note_uhd_examples.pdf`, Accessed: 2017.

[40] N. Instruments, *LabVIEW: User manual*, `http://www.ni.com/pdf/manuals/320999b.pdf`, Accessed: 2017.

[41] `https://forums.ni.com/t5/LabVIEW/How-to-resample-unequally-spaced-data-in-Array-form/td-p/306365`, Accessed: 2017.

[42] V. L. Clark and J. A. Kruse, "Clinical methods: The history, physical, and laboratory examinations", *Jama*, vol. 264, no. 21, pp. 2808–2809, 1990.

[43] G. Yuan, N. A. Drost, and R. A. McIvor, "Respiratory rate and breathing pattern", *Mcmaster university medical journal*, vol. 10, no. 1, pp. 23–25, 2013.

[44] J. N. S. Little M.A., `http://www.maxlittle.net/software/`.